ACS OMEGA

Article

Cite This: ACS Omega 2019, 4, 9512−9521

http://pubs.acs.org/journal/acsodf

Thermodynamic Insights into the Characteristics of Unary and Mixture Permeances in Microporous Membranes

Rajamani Krishna*

Van't Hoff Institute for Molecular Sciences, University of Amsterdam, Science Park 904, 1098 XH Amsterdam, The Netherlands

Supporting Information

ABSTRACT: The primary objective of this article is to gain fundamental insights into the dependences of component permeances Π_i in microporous membranes on the operating conditions (upstream partial pressures, temperature, and feed composition). It is argued that the permeances Π_i for unary systems and mixtures need to be compared on the basis of the adsorption potential $\pi A/RT$, a convenient and practical proxy for the spreading pressure π that is calculable using the ideal adsorbed solution theory for mixture adsorption equilibrium. The use of $\pi A/RT$ as a yardstick serves to elucidate and rationalize a wide variety of published experimental Π_i data on unary and mixture permeances in microporous membranes. For cage-type host structures such as SAPO-34, DDR, and ZIF-8, the Π_i values are uniquely dictated by the magnitude of $\pi A/RT$, irrespective of the partner species in the mixture. For MFI membranes, the tardier species slows down the more mobile partners due to correlated molecular motion within the channels; the degree of correlation is also a function of $\pi A/RT$.

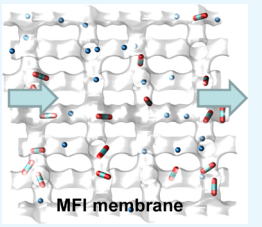

1. INTRODUCTION

Membrane technologies find applications in a variety of separation applications such as gas separations and water/alcohol pervaporation.[1,2] The permselective membrane layers often consist of microporous materials such as zeolites (aluminosilicates), metal−organic frameworks (MOFs), zeolitic imidazolate frameworks (ZIFs), or carbon molecular sieves.[3−16] Experimental data on membrane permeation are most commonly presented in terms of the component permeances defined by

$$\Pi_i = \frac{N_i}{p_{i0} - p_{i\delta}} \tag{1}$$

where N_i is the permeation flux and $p_{i0} - p_{i\delta}$ is the difference in the partial pressures at the upstream (subscript 0) and downstream (subscript δ) faces of the membrane layer of thickness δ. The permeance of any guest species is influenced by a variety of factors such as the connectivity and pore topology of the microporous host material, operating conditions (temperature, pressure, and feed mixture composition), and the choice of the partner species in the mixture. The pore landscapes of four important host materials CHA, DDR, ZIF-8, and MFI that have membrane applications are shown in Figure 1. CHA zeolite consists of cages of 316 Å^3 volume, separated by 8-ring windows of 3.8 Å × 4.2 Å size. DDR zeolite has cages of 278 Å^3 volume, separated by 8-ring windows of 3.65 Å × 4.37 Å size. ZIF-8 has an SOD (sodalite) topology, consisting of cages of 1168 Å^3 volume, separated by 3.3 Å windows; the windows are flexible. MFI zeolite consists of a set of intersecting straight channels and zigzag (or sinusoidal) channels of 5.5 Å size.

Figure 2a,b presents experimental data for permeances of CO_2 and H_2 determined for unary and mixture permeation across the SAPO-34 membrane. SAPO-34 has the same structural topology as CHA zeolite. Compared at the same partial pressures, the H_2 permeance is significantly reduced due to the presence of partner species CO_2, CH_4, and N_2; the reduction is significantly higher with CO_2 as a partner. In sharp contrast, CO_2 permeance is only marginally influenced by the presence and choice of the partner species in the mixtures: CH_4, N_2, and H_2.

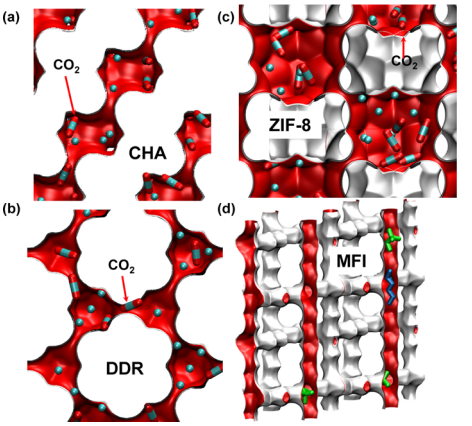

Figure 1. Pore landscapes of (a) CHA, (b) DDR, (c) ZIF-8, and (d) MFI zeolite, along with computational snapshots of guest molecules.

Figure 3a compares the experimental data on permeances of CO_2 and H_2 determined for unary and binary mixture permeation across an MFI membrane. The CO_2 and H_2 mixture permeances are both lower than the corresponding values for unary systems when compared at the same partial pressures in the upstream compartment. For H_2, the more mobile guest, the

Received: April 1, 2019
Accepted: May 20, 2019
Published: May 30, 2019

DOI: 10.1021/acsomega.9b00907
ACS Omega 2019, 4, 9512−9521

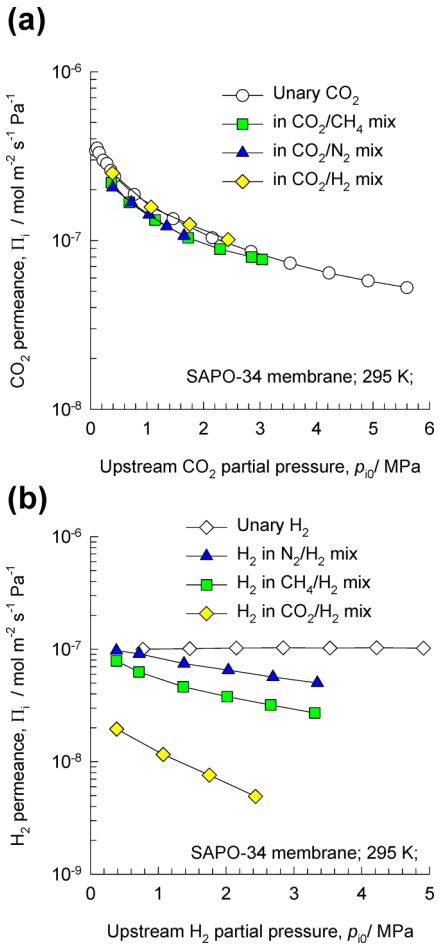

Figure 2. (a,b) Experimental data of Li et al.[41−43] for permeances of (a) CO_2 and (b) H_2 determined for unary and equimolar binary mixture permeation across the SAPO-34 membrane at 295 K. The x axis represents the partial pressures in the feed mixture in the upstream membrane compartment.

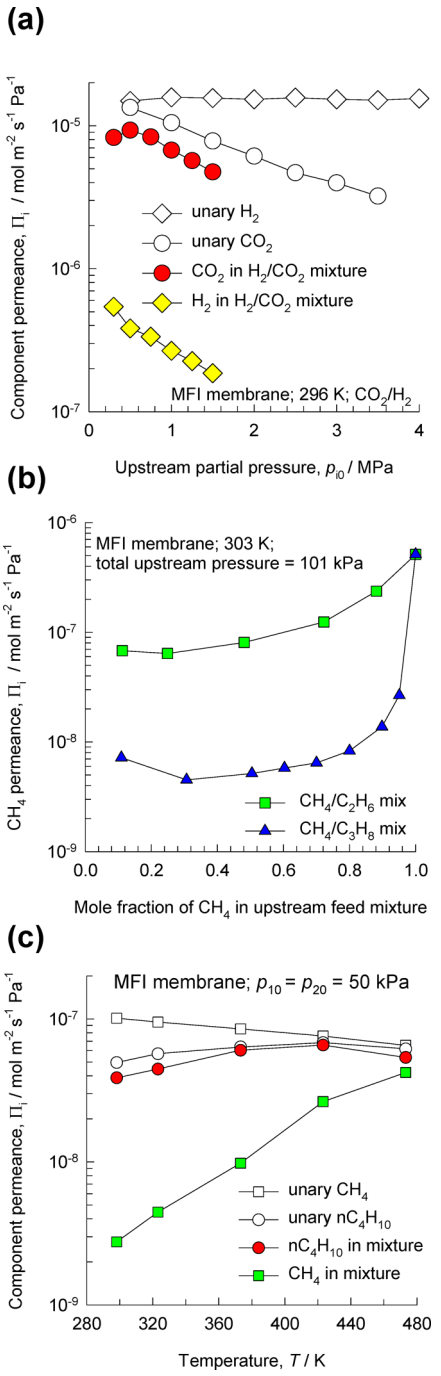

Figure 3. (a) Experimental data of Sandström et al.[44] for the component permeances for unary species and 50:50 CO_2/H_2 feed mixtures across the MFI membrane at 296 K. (b) Experimental data of van de Graaf et al.[45] for component permeances of CH_4/C_2H_6 and CH_4/C_3H_8 mixtures in the MFI membrane at 303 K. (c) Experimental data of Vroon et al.[46] for unary and 50:50 CH_4/n-C_4H_{10} mixture permeation across the MFI membrane at a total pressure of 100 kPa and varying temperatures.

lowering is by about 1 order of magnitude, while the permeance of the tardier CO_2 is lowered by a factor of about 2. The data based on unary permeation anticipates H_2-selective separation whereas the data for mixture permeation displays CO_2-selective separations.

Consider the experimental data for permeation of CH_4/C_2H_6 and CH_4/C_3H_8 mixtures across an MFI membrane at 303 K presented in Figure 3b. The two sets of experimental permeance data are plotted as functions of the mole fraction of the more mobile guest, CH_4, in the feed gas mixture in the upstream compartment. Increasing the proportion of the tardier component C_2H_6 in the CH_4/C_2H_6 feed mixture has the effect of progressively reducing the permeance of the more mobile CH_4 by up to an order of magnitude. The reduction of CH_4 permeance is significantly higher, by up to 2 orders of magnitude, for CH_4/C_3H_8 mixture permeation.

For 50:50 CH_4/n-C_4H_{10} mixture permeation across an MFI membrane, the experimental data show that the reduction of CH_4 permeance due to the presence of the tardier partner n-C_4H_{10} is considerably more significant at lower temperatures (see Figure 3c). As the temperature is increased, the component permeances become closer in values.

The experimental data for permeation of mixtures of n-hexane (nC6) and 2,2-dimethylbutane (22DMB) across an MFI membrane are remarkable in that the permeance of the tardier 22DMB is further reduced by more than 2 orders of magnitude by the presence of the more mobile nC6 partner (see Figure 4).

The wide variety of characteristics of membrane permeances witnessed in Figures 2−4 is a reflection of a combination of mixture adsorption equilibrium and mixture diffusion. The mixture adsorption equilibrium dictates the component loadings

DOI: 10.1021/acsomega.9b00907
ACS Omega 2019, 4, 9512−9521

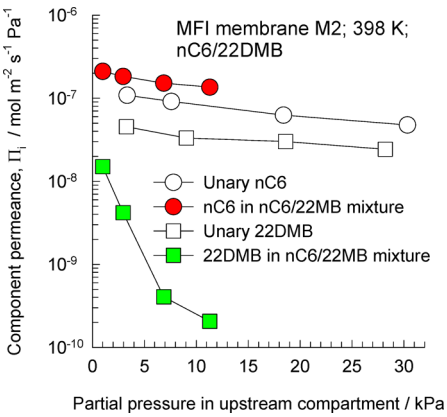

Figure 4. Experimental data of Gump et al.[47] for unary and 50:50 *n*C6/22DMB mixture permeances across the MFI membrane M2 at 398 K.

within the membrane layer; the component loadings, in turn, affect the guest mobilities, and slowing-down, or correlation, effects that often influence mixture permeation.[17−20] The primary objective of this article is to gain fundamental insights into the characteristics of unary and mixture permeances. Specifically, we aim to show that the fundamentally appropriate choice of the x axes in Figures 2−4 is the spreading pressure π calculated by use of the ideal adsorbed solution theory (IAST) of Myers and Prausnitz[21] for mixture adsorption. We shall demonstrate that the spreading pressure not only is a reflection of mixture adsorption equilibrium but also dictates the loading dependence of the guest diffusivities and correlation effects.[20]

2. METHODOLOGY FOR MODELING OF MIXTURE ADSORPTION AND DIFFUSION

2.1. IAST for Mixture Adsorption Equilibrium. Within microporous crystalline host materials, the guest constituent molecules exist entirely in the adsorbed phase. The Gibbs adsorption equation in differential form is[22−24]

$$A\ \mathrm{d}\pi = \sum_{i=1}^{n} q_i\ d\mu_i \tag{2}$$

In eq 2, A represents the surface area per kilogram of the framework, q_i is the molar loading, μ_i is the molar chemical potential, and π is the spreading pressure. At phase equilibrium, equating the component chemical potentials μ_i in the adsorbed phase and in the bulk gas phase mixture in the upstream membrane compartment, we write

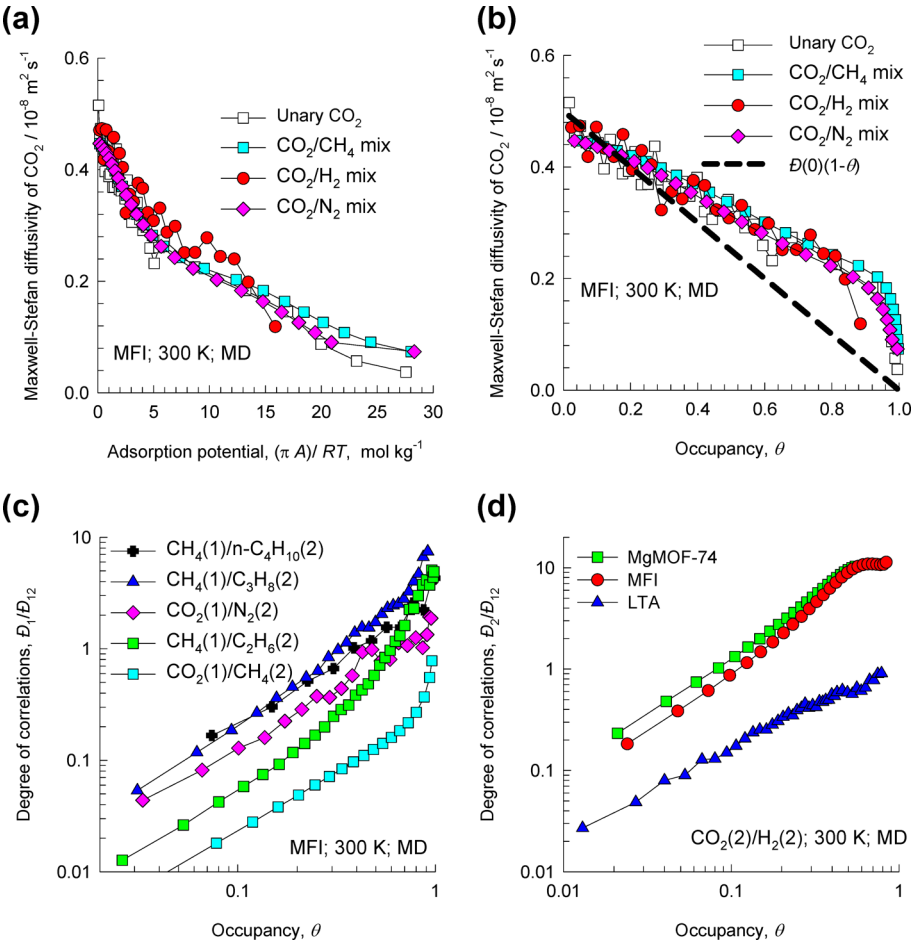

Figure 5. (a,b) Maxwell−Stefan diffusivity $Đ_i$ of CO_2 determined for MD simulation data[20] for diffusion of a variety of equimolar ($q_1 = q_2$) CO_2/H_2, CO_2/CH_4, and CO_2/N_2 mixtures in MFI zeolite at 300 K plotted as a function of the (a) adsorption potential $\pi A/RT$ and (b) the occupancy θ. Also shown in open symbols are the MD simulations of $Đ_i$ for unary CO_2 diffusion. (c) MD simulation data[20] for degree of correlations $Đ_1/Đ_{12}$ for equimolar ($q_1 = q_2$) CO_2/H_2, CO_2/CH_4, CO_2/N_2, CH_4/C_2H_6, CH_4/C_3H_8, and $CH_4/n\text{-}C_4H_{10}$ mixtures in MFI zeolite at 300 K. (d) MD simulation data[20] for degree of correlations $Đ_2/Đ_{12}$ for equimolar ($q_1 = q_2$) CO_2/H_2 mixtures in MFI, MgMOF-74, and LTA at 300 K.

DOI: 10.1021/acsomega.9b00907
ACS Omega 2019, 4, 9512−9521

$$d\mu_i = RT\ d\ln p_i \tag{3}$$

Briefly, the basic equation of the IAST theory is the analogue of Raoult's law for vapor−liquid equilibrium, that is

$$p_i = P_i^0 x_i; \quad i = 1, 2, ..., n \tag{4}$$

where x_i is the mole fraction in the adsorbed phase defined by

$$x_i = q_i/q_t; \quad q_t = q_1 + q_2 + ... + q_n; \quad i = 1, 2, ..., n \tag{5}$$

and P_i^0 is the pressure for sorption of every component i, which yields the same spreading pressure, π, for each of the pure components, as that for the mixture:

$$\frac{\pi A}{RT} = \int_0^{P_1^0} \frac{q_1^0(f)}{f} df = \int_0^{P_2^0} \frac{q_2^0(f)}{f} df = \int_0^{P_3^0} \frac{q_3^0(f)}{f} df = ... \tag{6}$$

In eq 6, $q_i^0(f)$ is the pure component adsorption isotherm. Since the surface area A is not directly accessible from experimental data, the adsorption potential $\pi A/RT$, with a unit of mole per kilogram, serves as a convenient and practical proxy for the spreading pressure π. For the simple case of a binary mixture in which each isotherm is described by the single-site Langmuir model with equal saturation capacities for each constituent

$$q_i^0(f) = q_{sat}\frac{b_i f}{1 + b_i f}; \quad i = 1, 2 \tag{7}$$

the following explicit expression can be derived

$$\frac{\pi A}{RT} = q_{sat}\ln(1 + b_1 p_1 + b_2 p_2) \tag{8}$$

For the more general case in which the saturation capacities of the constituents are unequal, the entire set of equations must be solved numerically. The unary isotherm data for all guest/host combinations analyzed in this article, along with the numerical details for determination of $\pi A/RT$, are provided in the Supporting Information.

2.2. Maxwell−Stefan Description of Mixture Diffusion.

The Maxwell−Stefan (M−S) approach is the most convenient and practical formulation that relates the molar permeation fluxes to the gradients of the molar chemical potential of the guest constituents.[20,25−27] For binary mixtures, the M−S equations are

$$-\rho\frac{q_1}{RT}\frac{d\mu_1}{dz} = \frac{x_2 N_1 - x_1 N_2}{Đ_{12}} + \frac{N_1}{Đ_1}$$
$$-\rho\frac{q_2}{RT}\frac{d\mu_2}{dz} = \frac{x_1 N_2 - x_2 N_1}{Đ_{12}} + \frac{N_2}{Đ_2} \tag{9}$$

where ρ represents the framework density of the microporous crystalline material. The $Đ_1$ and $Đ_2$ characterize the guest−wall interactions. The exchange coefficient $Đ_{12}$ reflects how the facility for transport of species i correlates with that of species j. The ratios $Đ_1/Đ_{12}$ and $Đ_2/Đ_{12}$ quantify the degrees of correlation. The magnitude of $Đ_1$, relative to that of $Đ_{12}$, determines the extent to which the flux of species 1 is influenced by the chemical potential gradient of species 2. The larger is the degree of correlation, $Đ_1/Đ_{12}$, the stronger is the influence of diffusional "coupling".

The persuasive advantage of using the M−S formulation is that the M−S diffusivities $Đ_i$ can be identified with the corresponding diffusivities for unary systems provided that the values are determined at the same adsorption potential $\pi A/RT$; this has been established in earlier work[20] with the aid of molecular dynamics (MD) simulations for a vast number of mixture diffusion in several zeolites and MOFs. As illustrated, Figure 5a compares the M−S diffusivity $Đ_i$ of CO_2 determined for MD simulation data for diffusion of equimolar ($q_1 = q_2$) CO_2/H_2, CO_2/CH_4, and CO_2/N_2 mixtures in MFI zeolite with the corresponding unary diffusivity. Compared at the same value of $\pi A/RT$, the M−S diffusivities $Đ_i$ have practically the same value, confirming that the adsorption potential is the correct yardstick to compare diffusivities. To rationalize the lowering of the M−S diffusivity with increasing values of $\pi A/RT$, we plot in Figure 5b the diffusivity data as a function of the fractional occupancy θ determined from

$$\theta = 1 - \exp(-\pi A/q_{sat}RT) \tag{10}$$

For a binary mixture, the saturation capacity q_{sat} is defined as follows[20]

$$\frac{1}{q_{sat}} = \frac{x_1}{q_{1,sat}} + \frac{x_2}{q_{2,sat}} \tag{11}$$

Increasing the fractional occupancy lowers the values of $Đ_i$ because the channels of MFI become increasingly crowded; indeed, $Đ_i \to 0$ as $\theta \to 1$ for all guest species. For binary mixtures in which the unary isotherms are described by eq 7, eqs 10 and 11 are simplified to yield

$$\theta = \frac{q_t}{q_{sat}} = \frac{b_1 p_1 + b_2 p_2}{1 + b_1 p_1 + b_2 p_2} \tag{12}$$

The simplest model to describe the occupancy dependence is indicated by the dashed line in Figure 5b

$$Đ_i = Đ_i(0)(1 - \theta) \tag{13}$$

where $Đ_i(0)$ is the M−S diffusivity at "zero loading". Equation 13 is essentially based on a simple hopping model in which a molecule can jump from one adsorption site to an adjacent one, provided that it is not already occupied.[28,29] Using a simple two-dimensional square lattice model, the M−S diffusivity in the limit of vanishingly small occupancies is $Đ_i(0) = \frac{1}{\zeta}\nu_i(0)\lambda^2$, where $\zeta = 4$ is the coordination number of the 2D array of lattice sites, λ is the jump distance on the square lattice, and $\nu_i(0)$ is the jump frequency at a vanishingly small occupancy.[29] More generally, molecule−molecule interactions serve to influence the jump frequencies by a factor that depends on the energy of interaction w. For repulsive interactions, $w > 0$, whereas for attractive interactions, $w < 0$. The quasichemical approach of Reed and Ehrlich[30] can be used to quantify such interactions.[29,31,32]

The implication of the plots in Figure 5a,b is that $\pi A/RT$ and θ are the appropriate thermodynamic measures of the loadings within the pores of microporous materials.

MD simulation data[20] for several mixture/host combinations also show that the degree of correlation increases with pore occupancy, practically linearly, as illustrated in Figure 5c for binary mixtures in MFI zeolite. For CO_2/H_2 mixtures, the

DOI: 10.1021/acsomega.9b00907
ACS Omega 2019, 4, 9512−9521

degrees of correlation for MFI, MgMOF-74, and LTA are compared in Figure 5d. For LTA with narrow windows separating adjacent cages, the degree of correlation is significantly lower than those for MFI and MgMOF-74.

From the IAST and M−S theories, it emerges that the adsorption potential $\pi A/RT$ not only encapsulates mixture adsorption equilibrium but also serves as the proper measure of the loading dependence of the M−S diffusivities $Đ_1$ and $Đ_2$ and the degree of correlation $Đ_1/Đ_{12}$. We should therefore expect $\pi A/RT$ to be the correct yardstick to compare component permeances for unary and mixture permeation in Figures 2−4.

3. RESULTS AND DISCUSSION

3.1. Permeation across SAPO-34, DDR, and ZIF-8 Membranes. Figure 6 presents plots of the component permeances for CO_2 and H_2 determined for unary and equimolar binary mixture permeation across the SAPO-34 membrane at 295 K, plotted as a function of $\pi A/RT$ calculated at the upstream face of the membrane, in equilibrium with the feed mixture in the upstream compartment. The CO_2 and H_2 permeances appear to be uniquely dependent on the adsorption potential and are independent of the partner species. The reasons for this simple and convenient finding are threefold: (i) the mixture adsorption equilibrium between the feed mixture and the upstream face of the membrane is properly quantified by the choice of $\pi A/RT$ as x axes, (ii) the loading dependence of the diffusivities is also described by $\pi A/RT$, and (iii) the correlation effects are of negligible importance in SAPO-34 because the guest molecules jump one at a time across the narrow windows, resulting in $Đ_1/Đ_{12} \to 0$ as evidenced by MD data.[17−20]

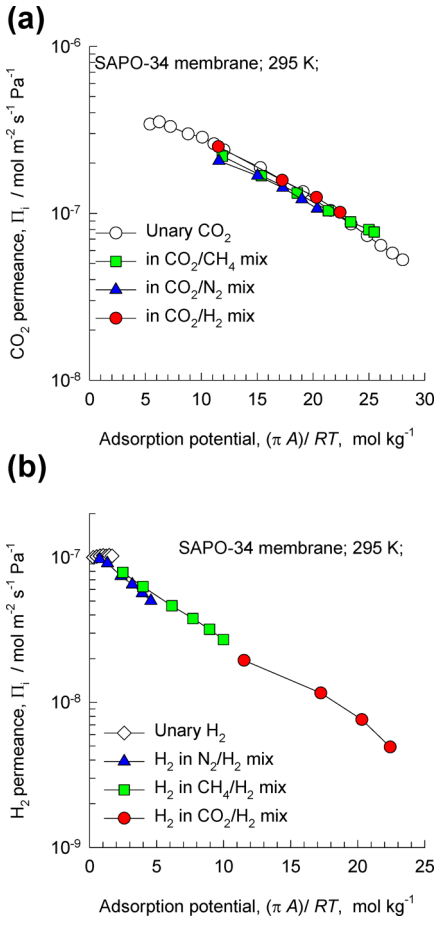

Figure 6. Experimental data of Li et al.[41−43] for permeances of (a) CO_2 and (b) H_2 determined for unary and equimolar binary mixture permeation across the SAPO-34 membrane at 295 K. The x axes in panels (a) and (b) represent the adsorption potential, corresponding to the conditions at the upstream face of the membrane.

In Figure 7a−c, the experimental data on component permeances for 50:50 CO_2/CH_4 and 50:50 N_2/CH_4 mixture permeation across a DDR membrane are plotted as a function of

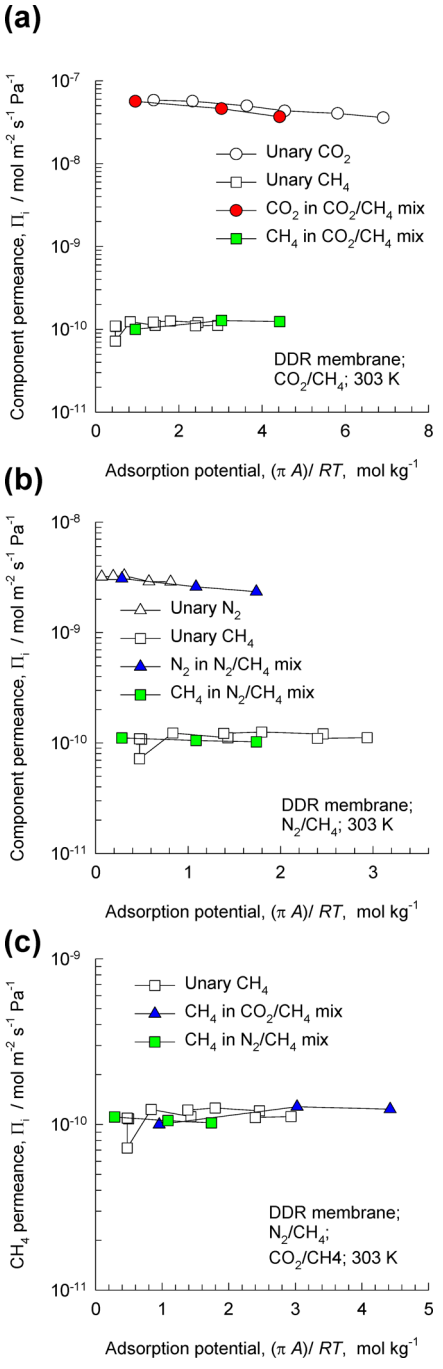

Figure 7. (a−c) Experimental data of Van den Bergh et al.[48,49] for component permeances for 50:50 CO_2/CH_4 and 50:50 N_2/CH_4 binary mixture permeation across the DDR membrane at 303 K. The x axes in panels (a), (b), and (c) represent the adsorption potential, corresponding to the conditions at the upstream face of the membrane.

DOI: 10.1021/acsomega.9b00907
ACS Omega 2019, 4, 9512−9521

the adsorption potential at the upstream face of the membrane. The intercage hopping of guest molecules is uncorrelated, and there are no slowing-down effects experienced by the more mobile partner species. The component permeances in the mixture have the same values as those in the corresponding unary systems. The CH_4 permeance is independent of the choice of CO_2 or N_2 as a partner in the mixture (see Figure 7c).

Experimental data for component permeances for 50:50 C_3H_6/C_3H_8 binary mixture permeation across the ZIF-8 membrane at 308 K have practically the same magnitudes as the corresponding unary permeances when compared at the same $\pi A/RT$ at the upstream face of the membrane (see Figure 8). The explanation is precisely analogous to that for SAPO-34 and DDR membranes.

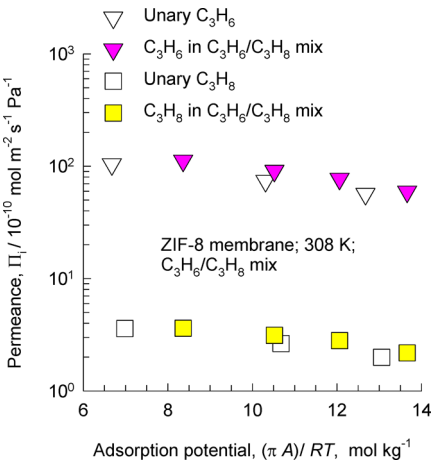

Figure 8. Experimental data of Liu et al.[50] for component permeances for 50:50 C_3H_6/C_3H_8 binary mixture permeation across the ZIF-8 membrane at 308 K, compared to unary permeation data. The data are plotted as a function of adsorption potential $\pi A/RT$ at the upstream face of the membrane.

3.2. Permeation across an MFI Membrane. Correlation or slowing-down effects are of significant importance for guest diffusion in MFI zeolite, as has been established by MD simulations[17−20] (see data on degrees of correlation in Figure 5c,d). Consequently, the permeance of more mobile partners should be expected to be lowered due to correlated jumps with the tardier partner species within the pores. Figure 9a,b compares the component permeances of 50:50 CO_2/H_2 feed mixtures in the MFI membrane with the corresponding values for the unary species. Also shown by continuous solid lines are the estimations using the M−S model.[19] In the model calculations, the occupancy dependence of each guest is assumed to follow eq 13 wherein the zero-loading diffusivities are fitted from the unary permeance data: $\rho Đ_1(0)/\delta$ = 3.2 and $\rho Đ_2(0)/\delta$ = 100 kg m^{-2} s^{-1}. The degree of correlation is taken to increase linearly with occupancy θ. The H_2 permeance is significantly influenced by correlation effects, as evidenced in Figure 9b for calculations with $Đ_2/Đ_{12}$ = 1.0θ, 3.0θ, and 10.0θ; the choice $Đ_2/Đ_{12}$ = 10.0θ affords the best match with experimental data and is also in accordance with the MD data in Figure 5d.

Figure 10a,b compares the permeances for (a) CH_4/C_2H_6 and (b) CH_4/C_3H_8 mixtures in MFI with the corresponding values for unary systems as a function of $\pi A/RT$. For both mixtures, the permeances of the more strongly adsorbed but tardier components in the two mixtures, C_2H_6 and C_3H_8, are practically

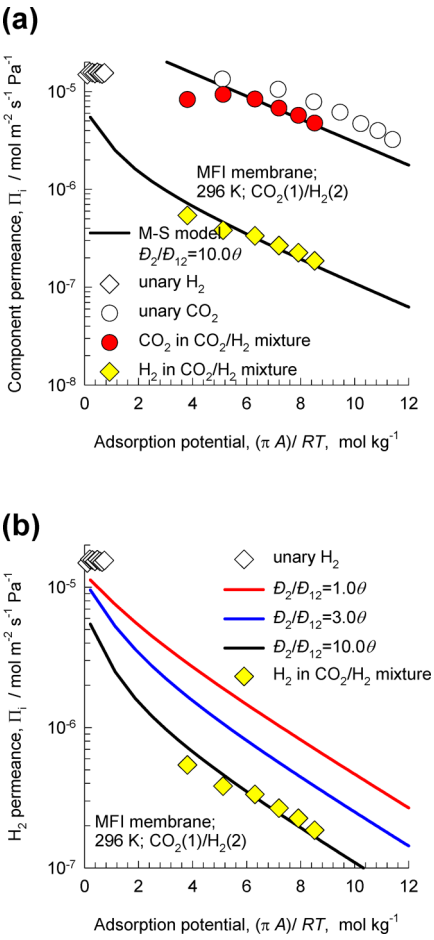

Figure 9. (a,b) Experimental data of Sandström et al.[44] for component permeances in 50:50 CO_2/H_2 feed mixtures across the MFI membrane at 296 K compared with the estimates using the M−S model (indicated by the continuous solid lines). The x axes represent the adsorption potential, corresponding to the conditions at the upstream face of the membrane.

the same as the unary values. The permeance of the more mobile CH_4 is reduced significantly below the unary values due to two separate reasons: (i) the M−S diffusivity of CH_4 reduces with increasing values of $\pi A/RT$[20] and (ii) the CH_4 mobility in the intersecting channel structures is strongly correlated with those of the tardier partners C_2H_6 and C_3H_8. The correlation effects increase with increasing values of $\pi A/RT$, as evidenced in the MD simulation data in Figure 5c. It is also noteworthy that the degree of correlations for CH_4/C_3H_8 mixtures is higher than that for CH_4/C_2H_6; this rationalizes the stronger reduction in the CH_4 permeance due to partnership with C_3H_8.

The influence of the operating temperature for CH_4/n-C_4H_{10} mixture permeation across the MFI membrane (cf. Figure 3d) is simply elucidated by plotting the permeances as a function of $\pi A/RT$, calculated at the upstream face of the membrane (see Figure 10c). The permeance of the tardier, more strongly adsorbed n-C_4H_{10} is practically the same as the corresponding values for unary diffusion. The permeance of the more mobile, poorly adsorbed CH_4 is reduced significantly below the unary values due to reduction in the M-S diffusivity of CH_4 with increased pore occupancy and the increasing influence of correlations, as evidenced in the MD simulation data in Figure 5c.

DOI: 10.1021/acsomega.9b00907
ACS Omega 2019, 4, 9512−9521

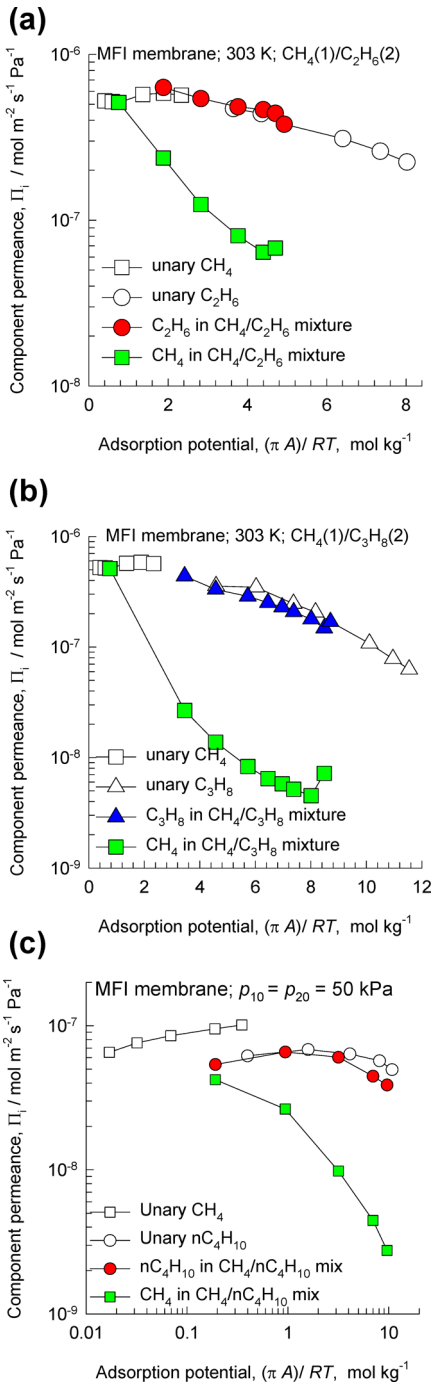

Figure 10. Experimental data of van de Graaf et al.[45] for component permeances of (a) CH_4/C_2H_6 and (b) CH_4/C_3H_8 mixtures in MFI membrane at 303 K. (c) Experimental data of Vroon et al.[46] for 50:50 CH_4/n-C_4H_{10} mixture permeation across the MFI membrane at a total pressure of 100 kPa and varying temperatures. The x axes in panels (a), (b), and (c) represent the adsorption potential, corresponding to the conditions at the upstream face of the membrane.

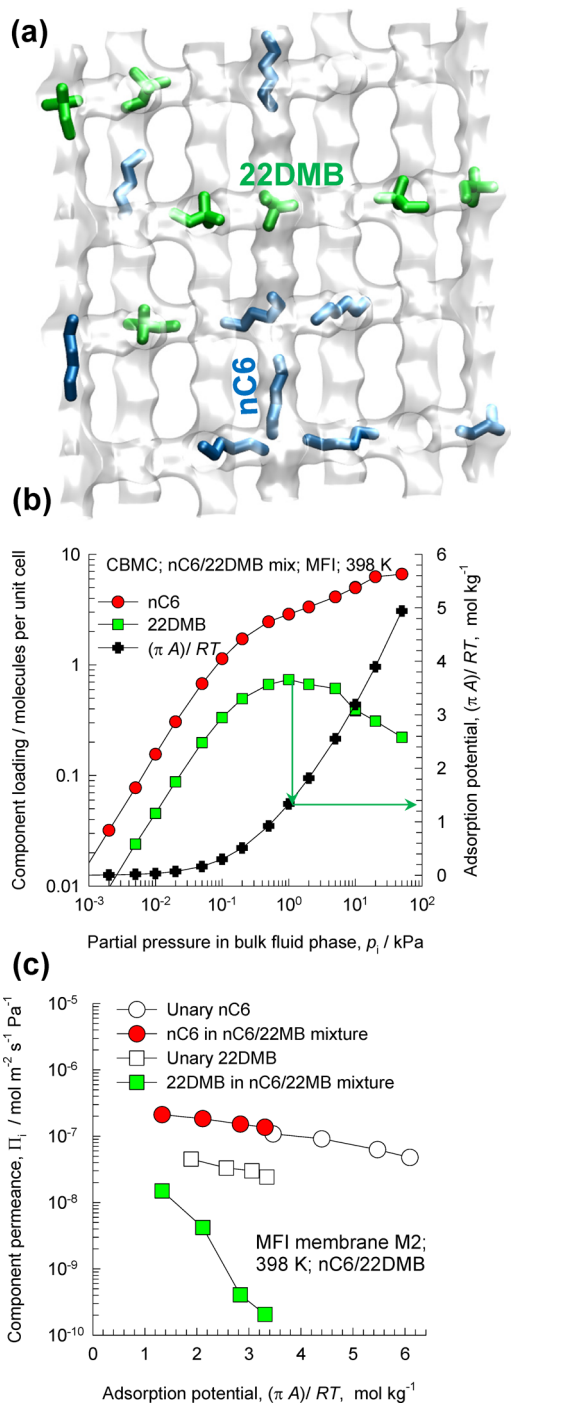

Figure 11. (a) Computational snapshots showing the location of nC6 and 22DMB within the intersecting channels of MFI zeolite. (b) Configurational-bias Monte Carlo simulations of nC6/22DMB mixture adsorption in MFI at 398 K. Also shown in the right y axis is the adsorption potential $\pi A/RT$. (c) Experimental data of Gump et al.[47] for component permeances for nC6/22DMB mixture in MFI membrane M2 at 398 K plotted as a function of the adsorption potential $\pi A/RT$ at the upstream face of the membrane.

The explanation of the nC6/22DMB mixture permeation data in Figure 4 requires insights into entropy effects in mixture adsorption,[33−38] gained from configurational-bias Monte Carlo (CBMC) simulations[25,36,37] for nC6/22DMB mixture adsorption. The linear nC6 molecule can locate along both the straight channels and zigzag channels, whereas the more compact but bulkier dibranched isomer 22DMB can locate only at the intersections (see computational snapshots in Figure 11a). Per unit cell of MFI, there are only four intersection sites, and therefore, the saturation capacity of 22DMB is restricted to four molecules per unit cell. On the other hand, the saturation capacity for nC6 is eight molecules per unit cell. CBMC simulations for nC6/22DMB mixture adsorption show that, for bulk phase partial pressure p_i = 1 kPa, the 22DMB loading

DOI: 10.1021/acsomega.9b00907
ACS Omega 2019, 4, 9512−9521

reaches a maximum value at an adsorption potential $\pi A/RT$ of 1.2 mol kg^{-1} (see Figure 11b). For p_i > 1 kPa and $\pi A/RT$ > 1.2 mol kg^{-1}, the increase of bulk phase partial pressures results in the decrease in the 22DMB loading, engendered by entropy effects that can be elucidated by invoking the entropy maximization principle of Boltzmann $S = k_B \ln(W)$.[33,39] The experimental permeance data for 50:50 *n*C6/22DMB mixtures were obtained under conditions corresponding to $\pi A/RT$ > 1.2 mol kg^{-1} (cf. Figure 11c), and the sharp reduction in 22DMB permeance below the unary permeance values is entirely ascribable to configurational entropy effects that cause 22DMB loading at the upstream to decrease despite the increase in the bulk phase partial pressures. Unusually, both adsorption and diffusion act in synergy to suppress 22DMB permeation; this synergy is also observed for transient uptake of hexane isomers in MFI zeolite.[40]

4. CONCLUSIONS

The following major conclusions emerge from our investigations.

(1) The adsorption potential, $\pi A/RT$, calculable from the IAST, is the proper yardstick to compare permeances in mixtures with the corresponding data for unary systems.

(2) The adsorption potential quantifies the thermodynamic equilibrium between the fluid mixture in the upstream compartment and the adsorbed phase in the upstream face of the membrane. The IAST prescribes that the adsorption potential $\pi A/RT$, a practical proxy for the spreading pressure π, be equal for each of the pure constituents and the mixture (see eq 6).

(3) The same parameter $\pi A/RT$ also dictates the variation of the Maxwell–Stefan diffusivities, $Đ_1$ and $Đ_2$ and the degree of correlations $Đ_1/Đ_{12}$ with pore occupancy (see Figure 5). The degree of correlations depends on the guest/host combination.

(4) For cage-type zeolite structures such as SAPO-34, DDR, and ZIF-8, the intercage hopping of guest molecules is practically uncorrelated. Therefore, the component permeances in such structures are uniquely dictated by the magnitude of $\pi A/RT$, irrespective of the partner species in the mixture.

(5) In topologies such as MFI, correlation effects cause the permeance of the more mobile, less strongly adsorbed component to be lowered due to correlations with the tardier, more strongly adsorbed partners; the extent of lowering also correlates with $\pi A/RT$.

(6) Also highlighted in this article is the permeation of *n*C6/22DMB mixtures in the MFI membrane; here, configurational entropy effects cause a significant lowering in the permeance of the tardier dibranched isomer.

ASSOCIATED CONTENT

Supporting Information

The Supporting Information is available free of charge on the ACS Publications website at DOI: 10.1021/acsomega.9b00907.

Detailed derivation of the IAST calculation procedures for the spreading pressure and the adsorption potential using the unary adsorption isotherms, structural details for host materials considered and analyzed in this article, and unary isotherm parameter fits for all guest/host combinations considered in our article (PDF)

AUTHOR INFORMATION

Corresponding Author

*E-mail: r.krishna@contact.uva.nl.

ORCID

Rajamani Krishna: 0000-0002-4784-8530

Notes

The author declares no competing financial interest.

ACKNOWLEDGMENTS

The author expresses his gratitude to Dr. Jasper van Baten for providing the computational snapshots and pore landscapes of microporous structures.

NOMENCLATURE

Latin Alphabet

A	surface area per kilogram of framework (m^2 kg^{-1})
b_i	Langmuir constant for species i (Pa^{-1})
$Đ_i$	Maxwell–Stefan diffusivity for molecule–wall interaction (m^2 s^{-1})
$Đ_i(0)$	M–S diffusivity at zero loading (m^2 s^{-1})
$Đ_{ij}$	M–S exchange coefficient (m^2 s^{-1})
n	number of species in the mixture, dimensionless
N_i	molar flux of species i with respect to framework (mol m^{-2} s^{-1})
p_i	partial pressure of species i (Pa)
q_i	component molar loading of species i (mol kg^{-1})
$q_{i,sat}$	molar loading of species i at saturation (mol kg^{-1})
q_t	total molar loading in mixture (mol kg^{-1})
R	gas constant (8.314 J mol^{-1} K^{-1})
T	absolute temperature (K)
w	energy of interaction (J mol^{-1})
x_i	mole fraction of species i in the adsorbed phase (dimensionless)
z	distance coordinate (m)

Greek Alphabet

δ	membrane thickness (m)
ζ	coordination number of lattice (dimensionless)
λ	jump distance in the lattice model (m)
μ_i	molar chemical potential of component i (J mol^{-1})
π	spreading pressure (N m^{-1})
Π_i	permeance of species i (mol m^{-2} s^{-1} Pa^{-1})
θ	fractional occupancy (dimensionless)
ν	jump frequency (s^{-1})
ρ	framework density (kg m^{-3})

Subscripts

1	referring to component 1
2	referring to component 2
i	referring to component i
t	referring to total mixture
sat	referring to saturation conditions

REFERENCES

(1) Sirkar, K. K. *Separation of Molecules, Macromolecules and Particles. Principles, Phenomena and Processes*; Cambridge University Press: Cambridge, 2014.

(2) Wesselingh, J. A.; Krishna, R. *Mass transfer in multicomponent mixtures*; VSSD: Delft, 2000.

(3) Caro, J.; Noack, M. Zeolite membranes - Recent Developments and Progress. *Microporous Mesoporous Mater.* **2008**, *115*, 215–233.

(4) Caro, J. Are MOF membranes better in gas separation than those made of zeolites? *Curr. Opin. Chem. Eng.* **2011**, *1*, 77–83.

DOI: 10.1021/acsomega.9b00907
ACS Omega 2019, 4, 9512–9521

(5) Hye Kwon, Y.; Kiang, C.; Benjamin, E.; Crawford, P.; Nair, S.; Bhave, R. Krypton-Xenon Separation Properties of SAPO-34 Zeolite Materials and Membranes. *AIChE J.* **2017**, *63*, 761−769.
(6) Feng, X.; Zong, Z.; Elsaidi, S. K.; Jasinski, J. B.; Krishna, R.; Thallapally, P. K.; Carreon, M. A. Kr/Xe Separation over a Chabazite Zeolite Membrane. *J. Am. Chem. Soc.* **2016**, *138*, 9791−9794.
(7) Bux, H.; Chmelik, C.; Krishna, R.; Caro, J. Ethene/Ethane Separation by the MOF Membrane ZIF-8: Molecular Correlation of Permeation, Adsorption, Diffusion. *J. Membr. Sci.* **2011**, *369*, 284−289.
(8) Bux, H.; Chmelik, C.; Van Baten, J. M.; Krishna, R.; Caro, J. Novel MOF-Membrane for Molecular Sieving Predicted by IR-Diffusion Studies and Molecular Modeling. *Adv. Mater.* **2010**, *22*, 4741−4743.
(9) Zhang, K.; Lively, R. P.; Dose, M. E.; Brown, A. J.; Zhang, C.; Chung, J.; Nair, S.; Koros, W. J.; Chance, R. R. Alcohol and Water Adsorption in Zeolitic Imidazolate Frameworks. *Chem. Commun.* **2013**, *49*, 3245−3247.
(10) Venna, S. R.; Carreon, M. A. Highly Permeable Zeolite Imidazolate Framework-8 Membranes for CO_2/CH_4 Separation. *J. Am. Chem. Soc.* **2010**, *132*, 76−78.
(11) Chmelik, C.; van Baten, J.; Krishna, R. Hindering effects in diffusion of CO_2/CH_4 mixtures in ZIF-8 crystals. *J. Membr. Sci.* **2012**, *397-398*, 87−91.
(12) Koros, W. J.; Zhang, C. Materials for Next-generation Molecularly Selective Synthetic Membranes. *Nat. Mater.* **2017**, *16*, 289−297.
(13) Lin, Y. S. Microporous and Dense Inorganic Membranes: Current Status and prospective. *Sep. Purif. Technol.* **2001**, *25*, 39−55.
(14) Anderson, M.; Wang, H.; Lin, Y. S. Inorganic membranes for carbon dioxide and nitrogen separation. *Rev. Chem. Eng.* **2012**, *28*, 101−121.
(15) Hasegawa, Y.; Abe, C.; Nishioka, M.; Sato, K.; Nagase, T.; Hanaoka, T. Formation of high flux CHA-type zeolite membranes and their application to the dehydration of alcohol solutions. *J. Membr. Sci.* **2010**, *364*, 318−324.
(16) Mittal, N.; Bai, P.; Siepmann, J. I.; Daoutidis, P.; Tsapatsis, M. Bioethanol Enrichment using Zeolite Membranes: Molecular Modeling, Conceptual Process Design and Techno-Economic Analysis. *J. Membr. Sci.* **2017**, *540*, 464−476.
(17) Krishna, R.; van Baten, J. M. Maxwell-Stefan modeling of slowing-down effects in mixed gas permeation across porous membranes. *J. Membr. Sci.* **2011**, *383*, 289−300.
(18) Krishna, R.; van Baten, J. M. Investigating the Influence of Diffusional Coupling on Mixture Permeation across Porous Membranes. *J. Membr. Sci.* **2013**, *430*, 113−128.
(19) Krishna, R. Using the Maxwell-Stefan formulation for Highlighting the Influence of Interspecies (1-2) Friction on Binary Mixture Permeation across Microporous and Polymeric Membranes. *J. Membr. Sci.* **2017**, *540*, 261−276.
(20) Krishna, R. Occupancy Dependency of Maxwell−Stefan Diffusivities in Ordered Crystalline Microporous Materials. *ACS Omega* **2018**, *3*, 15743−15753.
(21) Myers, A. L.; Prausnitz, J. M. Thermodynamics of Mixed-Gas Adsorption. *AIChE J.* **1965**, *11*, 121−127.
(22) Ruthven, D. M. *Principles of Adsorption and Adsorption Processes*; John Wiley: New York, 1984.
(23) Krishna, R.; van Baten, J. M.; Baur, R. Highlighting the Origins and Consequences of Thermodynamic Nonidealities in Mixture Separations using Zeolites and Metal-Organic Frameworks. *Microporous Mesoporous Mater.* **2018**, *267*, 274−292.
(24) Krishna, R.; Van Baten, J. M. Investigating the Non-idealities in Adsorption of CO_2-bearing Mixtures in Cation-exchanged Zeolites. *Sep. Purif. Technol.* **2018**, *206*, 208−217.
(25) Krishna, R. Describing the Diffusion of Guest Molecules inside Porous Structures. *J. Phys. Chem. C* **2009**, *113*, 19756−19781.
(26) Krishna, R. Diffusion in Porous Crystalline Materials. *Chem. Soc. Rev.* **2012**, *41*, 3099−3118.
(27) Krishna, R. The Maxwell-Stefan Description of Mixture Diffusion in Nanoporous Crystalline Materials. *Microporous Mesoporous Mater.* **2014**, *185*, 30−50.
(28) Krishna, R.; Baur, R. Modelling Issues in Zeolite Based Separation Processes. *Sep. Purif. Technol.* **2003**, *33*, 213−254.
(29) Krishna, R. The Maxwell-Stefan Description of Mixture Permeation across Nanoporous Graphene Membranes. *Chem. Eng. Res. Des.* **2018**, *133*, 316−325.
(30) Reed, D. A.; Ehrlich, G. Surface diffusion, atomic jump rates and thermodynamics. *Surf. Sci.* **1981**, *102*, 588−609.
(31) Krishna, R.; Paschek, D.; Baur, R. Modeling the occupancy dependence of diffusivities in zeolites. *Microporous Mesoporous Mater.* **2004**, *76*, 233−246.
(32) Krishna, R.; van Baten, J. M. A molecular dynamics investigation of a variety of influences of temperature on diffusion in zeolites. *Microporous Mesoporous Mater.* **2009**, *125*, 126−134.
(33) Krishna, R. Elucidation and Characterization of Entropy Effects in Mixture Separations with Micro-porous Crystalline Adsorbents. *Sep. Purif. Technol.* **2019**, *215*, 227−241.
(34) Vlugt, T. J. H.; Krishna, R.; Smit, B. Molecular Simulations of Adsorption Isotherms for Linear and Branched Alkanes and Their Mixtures in Silicalite. *J. Phys. Chem. B* **1999**, *103*, 1102−1118.
(35) Santilli, D. S. Pore probe: A new technique for measuring the concentrations of molecules inside porous materials at elevated temperatures. *J. Catal.* **1986**, *99*, 335−341.
(36) Calero, S.; Smit, B.; Krishna, R. Configurational entropy effects during sorption of hexane isomers in silicalite. *J. Catal.* **2001**, *202*, 395−401.
(37) Calero, S.; Smit, B.; Krishna, R. Separation of linear, mono-methyl and di-methyl alkanes in the 5-7 carbon atom range by exploiting configurational entropy effects during sorption on silicalite-1. *Phys. Chem. Chem. Phys.* **2001**, *3*, 4390−4398.
(38) Yu, M.; Falconer, J. L.; Noble, R. D. Adsorption of Liquid Mixtures on Silicalite-1 Zeolite: A Density-Bottle Method. *Langmuir* **2005**, *21*, 7390−7397.
(39) Krishna, R.; van Baten, J. M. Commensurate-Incommensurate Adsorption and Diffusion in Ordered Crystalline Microporous Materials. *Phys. Chem. Chem. Phys.* **2017**, *19*, 20320−20337.
(40) Titze, T.; Chmelik, C.; Kärger, J.; van Baten, J. M.; Krishna, R. Uncommon Synergy Between Adsorption and Diffusion of Hexane Isomer Mixtures in MFI Zeolite Induced by Configurational Entropy Effects. *J. Phys. Chem. C* **2014**, *118*, 2660−2665.
(41) Li, S.; Falconer, J. L.; Noble, R. D.; Krishna, R. Modeling permeation of CO_2/CH_4, CO_2/N_2, and N_2/CH_4 mixtures across SAPO-34 membrane with the Maxwell-Stefan equations. *Ind. Eng. Chem. Res.* **2007**, *46*, 3904−3911.
(42) Li, S.; Falconer, J. L.; Noble, R. D.; Krishna, R. Interpreting unary, binary and ternary mixture permeation across a SAPO-34 membrane with loading-dependent Maxwell-Stefan diffusivities. *J. Phys. Chem. C* **2007**, *111*, 5075−5082.
(43) Krishna, R.; Li, S.; van Baten, J. M.; Falconer, J. L.; Noble, R. D. Investigation of slowing-down and speeding-up effects in binary mixture permeation across SAPO-34 and MFI membranes. *Sep. Purif. Technol.* **2008**, *60*, 230−236.
(44) Sandström, L.; Sjöberg, E.; Hedlund, J. Very high flux MFI membrane for CO_2 separation. *J. Membr. Sci.* **2011**, *380*, 232−240.
(45) van de Graaf, J. M.; Kapteijn, F.; Moulijn, J. A. Modeling permeation of binary mixtures through zeolite membranes. *AIChE J.* **1999**, *45*, 497−511.
(46) Vroon, Z. A. E. P.; Keizer, K.; Gilde, M. J.; Verweij, H.; Burggraaf, A. J. Transport properties of alkanes through ceramic thin zeolite MFI membranes. *J. Membr. Sci.* **1996**, *113*, 293−300.
(47) Gump, C. J.; Noble, R. D.; Falconer, J. L. Separation of hexane isomers through nonzeolite pores in ZSM-5 zeolite membranes. *Ind. Eng. Chem. Res.* **1999**, *38*, 2775−2781.
(48) van den Bergh, J.; Zhu, W.; Groen, J. C.; Kapteijn, F.; Moulijn, J. A.; Yajima, K.; Nakayama, K.; Tomita, T.; Yoshida, S. Natural Gas Purification with a DDR Zeolite Membrane; Permeation Modelling with Maxwell-Stefan Equations. *Stud. Surf. Sci. Catal.* **2007**, *170*, 1021−1027.

DOI: 10.1021/acsomega.9b00907
ACS Omega 2019, 4, 9512−9521

(49) van den Bergh, J.; Zhu, W.; Gascon, J.; Moulijn, J. A.; Kapteijn, F. Separation and Permeation Characteristics of a DD3R Zeolite Membrane. *J. Membr. Sci.* **2008**, *316*, 35−45.
(50) Liu, D.; Ma, X.; Xi, H.; Lin, Y. S. Gas transport properties and propylene/propane separation characteristics of ZIF-8 membranes. *J. Membr. Sci.* **2014**, *451*, 85−93.

DOI: 10.1021/acsomega.9b00907
ACS Omega 2019, 4, 9512−9521

Thermodynamic Insights into the Characteristics of Unary and Mixture Permeances in Microporous Membranes

Rajamani Krishna*

Van 't Hoff Institute for Molecular Sciences

University of Amsterdam

Science Park 904

1098 XH Amsterdam, The Netherlands

email: r.krishna@contact.uva.nl

Table of Contents

1 Preamble

The Supporting Information accompanying our article *Thermodynamic Insights into the Characteristics of Unary and Mixture Permeances in Microporous Membranes* provides (a) detailed derivation of the IAST calculation procedures for the spreading pressure, and its proxy $\frac{\pi A}{RT}$, using the unary adsorption isotherms, (b) structural details for zeolites considered and analyzed in this article, and (c) Unary isotherm parameter fits for all guest/host combinations considered in our article.

2 Thermodynamics of Mixture Adsorption in Micro-porous Materials

Within microporous crystalline materials, the guest molecules exist in the adsorbed phase, and the thermodynamics of mixture adsorption has an important bearing on the diffusion characteristics of guest molecules. For that reason, we provide below a brief summary of the Ideal Adsorbed Solution Theory (IAST) theory of Myers and Prausnitz.[1]

2.1 Brief outline of IAS theory

The Gibbs adsorption equation[2] in differential form is

$$Ad\pi = \sum_{i=1}^{n} q_i d\mu_i \tag{S1}$$

The quantity A is the surface area per kg of framework, with units of m^2 per kg of the framework of the crystalline material; q_i is the molar loading of component i in the adsorbed phase with units moles per kg of framework; μ_i is the molar chemical potential of component i. The spreading pressure π has the same units as surface tension, i.e. N m^{-1}.

The chemical potential of any component in the adsorbed phase, μ_i, equals that in the bulk fluid phase. If the partial fugacities in the bulk fluid phase are f_i, we have

$$d\mu_i = RTd \ln f_i \tag{S2}$$

where R is the gas constant (= 8.314 J mol^{-1} K^{-1}).

Briefly, the basic equation of Ideal Adsorbed Solution Theory (IAST) theory of Myers and Prausnitz[1] is the analogue of Raoult's law for vapor-liquid equilibrium, i.e.

$$f_i = P_i^0 x_i; \quad i = 1,2,...n \tag{S3}$$

where x_i is the mole fraction in the adsorbed phase

$$x_i = \frac{q_i}{q_1 + q_2 + ...q_n} \tag{S4}$$

and P_i^0 is the pressure for sorption of every component *i*, which yields the same spreading pressure, π for each of the pure components, as that for the mixture:

$$\frac{\pi A}{RT} = \int_0^{P_1^0} \frac{q_1^0(f)}{f} df = \int_0^{P_2^0} \frac{q_2^0(f)}{f} df = \int_0^{P_3^0} \frac{q_3^0(f)}{f} df = ... \tag{S5}$$

where $q_i^0(f)$ is the *pure* component adsorption isotherm. For *n*-component adsorption, there are a set of *n*-1 independent equalities in Equations (S5). The units of $\frac{\pi A}{RT}$, also called the adsorption potential,[3] are mol kg^{-1}. Each of the integrals in Equation (S5) can be evaluated analytically.

The unary isotherms may be described by say the dual-Langmuir-Freundlich model

$$q^0(f) = q_{A,sat} \frac{b_A f^{\nu A}}{1 + b_A f^{\nu A}} + q_{B,sat} \frac{b_B f^{\nu B}}{1 + b_B f^{\nu B}} \tag{S6}$$

For the dual-site Langmuir-Freundlich isotherm, the integration yields for component *i*,

$$\frac{\pi A}{RT} = \int_{f=0}^{P_i^0} \frac{q^0(f)}{f} df = \frac{q_{A,sat}}{\nu_A} \ln\left(1 + b_A \left(P_i^0\right)^{\nu_A}\right) + \frac{q_{B,sat}}{\nu_B} \ln\left(1 + b_B \left(P_i^0\right)^{\nu_B}\right) \tag{S7}$$

Invoking equation (S3) to express the sorption pressures in terms of the partial fugacities and component mole fractions we obtain

$$\frac{\pi A}{RT} = \int_{f=0}^{P_i^0} \frac{q^0(f)}{f} df = \frac{q_{A,sat}}{\nu_A} \ln\left(1 + b_A \left(\frac{f_i}{x_i}\right)^{\nu_A}\right) + \frac{q_{B,sat}}{\nu_B} \ln\left(1 + b_B \left(\frac{f_i}{x_i}\right)^{\nu_B}\right) \tag{S8}$$

For a specified set of partial fugacities f_i in the bulk fluid phase, a total of *n* in number, the right hand side of equation (S8) is a function of the mole fraction in the adsorbed phase x_i. For *n*-component adsorption, there are *n*-1 independent mole fractions x_i that are determined by solving the set of *n*-1 independent equalities in Equations (S5). These constraints may be solved using a suitable equation solver to determine the x_1, x_2, x_3,.. x_{n-1}, and $x_n = 1 - x_1 - x_2 - ... - x_{n-1}$. In all of the calculations

presented in this article, the set of *n*-1 non-linear equations were solved using the Given-Find solve block of MathCad 15.[4] For a binary mixture, a simple root finder is required to solve a single non-linear equation.

From knowledge of the adsorbed phase mole fractions x_i, the sorption pressures P_1^0, P_2^0, P_3^0,.. P_n^0 are then determined from

$$P_i^0 = \frac{f_i}{x_i}; \quad i = 1, 2, ...n \tag{S9}$$

A key assumption of the IAST is that the enthalpies and surface areas of the adsorbed molecules do not change upon mixing. If the total mixture loading is q_t, the area covered by the adsorbed mixture is $\frac{A}{q_t}$ with units of m^2 (mol mixture)$^{-1}$. Therefore, the assumption of no surface area change due to mixture adsorption translates as $\frac{A}{q_t} = \frac{Ax_1}{q_1^0\left(P_1^0\right)} + \frac{Ax_2}{q_2^0\left(P_2^0\right)} + \cdots \frac{Ax_n}{q_n^0\left(P_n^0\right)}$; the total mixture loading is q_t is calculated from

$$q_t = q_1 + q_2 ... + q_n = \frac{1}{\frac{x_1}{q_1^0(P_1^0)} + \frac{x_2}{q_2^0(P_2^0)} + ... + \frac{x_n}{q_n^0(P_n^0)}} \tag{S10}$$

in which $q_1^0(P_1^0)$, $q_2^0(P_2^0)$,… $q_n^0(P_n^0)$ are determined from the unary isotherm fits, using the sorption pressures for each component P_1^0, P_2^0, P_3^0,.. P_n^0 that are available from the solutions of Equations (S5), (S8), and (S9).

From knowledge of the adsorption potential, $\frac{\pi A}{RT}$, the fractional occupancy for mixture adsorption is then calculated using

$$\theta = 1 - \exp\left(-\frac{\pi A}{q_{sat,mix} RT}\right) \tag{S11}$$

For a binary mixture, the saturation capacity $q_{sat,mix}$ is calculated from the saturation capacities of the constituent guests

$$q_{sat,mix} = \frac{1}{\dfrac{x_1}{q_{1,sat}} + \dfrac{x_2}{q_{2,sat}}}; \quad q_{1,sat} = q_{1,A,sat} + q_{1,B,sat}; \quad q_{2,sat} = q_{2,A,sat} + q_{2,B,sat} \tag{S12}$$

where

$$x_1 = \frac{q_1}{q_1 + q_2}; \quad x_2 = \frac{q_2}{q_1 + q_2} \tag{S13}$$

are the mole fractions in the adsorbed mixture. For equimolar mixtures, $x_1 = x_2 = 0.5$, equation (S13) simplifies to yield $q_{sat,mix} = \dfrac{2}{\dfrac{1}{q_{1,sat}} + \dfrac{1}{q_{2,sat}}}$.

The fundamental justification of Equation (S12) is provided by applying equation (S10) to pore saturation conditions.

Equation (S11) is the appropriate generalization of Equation (S25), derived in the following section for the mixed-gas Langmuir model. It is also to be noted that equation (15) of our earlier publication[5] has a typographical error in the calculation of $q_{sat,mix}$; the correct form is given by equation (S12).

2.2 IAST model: 1-site Langmuir isotherms

The IAST procedure will be applied for binary mixture adsorption in which the unary isotherms are described by the 1-site Langmuir model in which the saturation capacities of components 1 and 2 are identical to each other, i.e. $q_{1,sat} = q_{2,sat} = q_{sat}$:

$$q^0(f) = q_{sat}\frac{bf}{1+bf}; \quad \theta = \frac{bf}{1+bf} \tag{S14}$$

where we define the fractional *occupancy* of the adsorbate molecules, $\theta = q^0(f)/q_{sat}$. The superscript 0 is used to emphasize that $q^0(f)$ relates the *pure component* loading to the bulk fluid fugacity.

For unary adsorption, the adsorption potential for a 1-site Langmuir isotherm can be calculated analytically

$$\frac{\pi A}{RT} = q_{sat} \ln\left(1 + bP^0\right) \tag{S15}$$

The objective is to determine the molar loadings, q_1, and q_2, in the adsorbed phase.

Performing the integration of Equation (S5) results in an expression relating the sorption pressures P_i^0 of the two species

$$\begin{aligned} &\frac{\pi A}{RT} = q_{sat} \ln\left(1 + b_1 P_1^0\right) = q_{sat} \ln\left(1 + b_2 P_2^0\right) \\ &b_1 P_1^0 = b_2 P_2^0 = \exp\left(\frac{\pi A}{q_{sat} RT}\right) - 1 \end{aligned} \tag{S16}$$

The adsorbed phase mole fractions of component 1, and component 2 are given by equation (S9)

$$x_1 = \frac{f_1}{P_1^0}; \quad x_2 = 1 - x_1 = \frac{f_2}{P_2^0} \tag{S17}$$

Combining equations (S16), and (S17):

$$\begin{aligned} &\exp\left(\frac{\pi A}{q_{sat} RT}\right) - 1 = b_1 \frac{f_1}{x_1} = b_2 \frac{f_2}{1 - x_1} \\ &\frac{\pi A}{q_{sat} RT} = \ln\left(1 + b_1 \frac{f_1}{x_1}\right) = \ln\left(1 + b_2 \frac{f_2}{x_2}\right) \end{aligned} \tag{S18}$$

The adsorbed phase mole fractions can be determined

$$\frac{x_1}{x_2} = \frac{q_1}{q_2} = \frac{b_1 f_1}{b_2 f_2}; \quad x_1 = \frac{q_1}{q_t} = \frac{b_1 f_1}{b_1 f_1 + b_2 f_2}; \quad x_2 = \frac{q_2}{q_t} = \frac{b_2 f_2}{b_1 f_1 + b_2 f_2} \tag{S19}$$

Once x_1, and $x_2 = 1 - x_1$ are determined, the sorption pressures can be calculated:

$$P_1^0 = \frac{f_1}{x_1}; \quad P_2^0 = \frac{f_2}{x_2} = \frac{f_2}{1 - x_1} \tag{S20}$$

From equations (S16), (S19), and (S20) we get

$$\begin{aligned} &b_i P_1^0 = \frac{b_1 f_1}{x_1} = b_2 P_2^0 = \frac{b_2 f_2}{x_2} = b_1 f_1 + b_2 f_2 \\ &1 + b_i P_1^0 = 1 + b_2 P_2^0 = 1 + b_1 f_1 + b_2 f_2 \end{aligned} \tag{S21}$$

Combining equations (S18), and (S21) we get the following expression for the adsorption potential for the mixture

$$\frac{\pi A}{RT} = q_{sat} \ln\left(1 + b_1 f_1 + b_2 f_2\right) \tag{S22}$$

The total amount adsorbed, $q_t = q_1 + q_2$ can be calculated from Equation (S10)

$$q_t = q_1 + q_2 = q_{sat} \frac{b_1 P_1^0}{1 + b_1 P_1^0} = q_{sat} \frac{b_2 P_2^0}{1 + b_2 P_2^0} = q_{sat} \frac{b_1 f_1 + b_2 f_2}{1 + b_1 f_1 + b_2 f_2} \tag{S23}$$

Combining equations (S19), and (S23) we obtain the following explicit expressions for the component loadings, and fractional occupancies

$$\theta_1 = \frac{q_1}{q_{sat}} = \frac{b_1 f_1}{1 + b_1 f_1 + b_2 f_2}; \quad \theta_2 = \frac{q_2}{q_{sat}} = \frac{b_2 f_2}{1 + b_1 f_1 + b_2 f_2} \tag{S24}$$

Equation (S24) is commonly referred to as the mixed-gas Langmuir model.

From equations (S16), (S23), and (S24) we derive the following expression for the total occupancy of the mixture

$$\theta = \theta_1 + \theta_2 = \frac{q_t}{q_{sat}} = 1 - \exp\left(-\frac{\pi A}{q_{sat} RT}\right) = \frac{b_1 f_1 + b_2 f_2}{1 + b_1 f_1 + b_2 f_2} \tag{S25}$$

For *unary* adsorption of component *i*, say, $f_i = P_i^0$, the occupancy of component 1 is

$$\theta_i = 1 - \exp\left(-\frac{\pi A}{q_{sat} RT}\right) = \frac{b_i f_i}{1 + b_i f_i}; \quad \text{unary adsorption of species i} \tag{S26}$$

From equations (S25), and (S26) we may also conclude the *occupancy* may be considered to be the appropriate *proxy* for the spreading pressure. The conclusion that we draw from the foregoing analysis is that the equalities of spreading pressures for unary adsorption of component 1, unary adsorption of component 2, and binary 1-2 mixture adsorption also implies the corresponding equalities of the corresponding *occupancies* for unary adsorption of component 1, unary adsorption of component 2, and binary 1-2 mixture adsorption.

3 Diffusion in Microporous Crystalline Materials

3.1 The Maxwell-Stefan (M-S) description of diffusion

Within micro-porous crystalline materials, such as zeolites, metal-organic frameworks (MOFs), and zeolitic imidazolate frameworks (ZIFs), the guest molecules exist in the adsorbed phase. The Maxwell-Stefan (M-S) equations for *n*-component diffusion in porous materials is applied in the following manner[6-13]

$$-\rho\frac{q_i}{RT}\frac{\partial\mu_i}{\partial r}=\sum_{\substack{j=1\\ j\neq i}}^{n}\frac{x_jN_i-x_iN_j}{Đ_{ij}}+\frac{N_i}{Đ_i};\qquad i=1,2,..n \tag{S27}$$

where ρ is the framework density with units of kg m^{-3}, q_i is the molar loading of adsorbate, and the adsorbed phase mole fractions are $x_i=q_i/q_t$ where q_t is the *total* mixture loading $q_t=\sum_{i=1}^{n}q_i$. The fluxes N_i in equations (S27) are defined in terms of the moles transported per m^2 of the *total surface of crystalline material*.

An important, persuasive, argument for the use of the M-S formulation for mixture diffusion is that the M-S diffusivity $Đ_i$ in mixtures can be estimated using information on the loading dependence of the corresponding unary diffusivity values, provided the comparison is made at the same value of the adsorption potential, calculated from IAST usingEquation (S5), or its proxy the occupancy, θ, calculated using equations (S11), (S12), (S13). Essentially this implies that the M-S diffusivity $Đ_i$ can be estimated from experimental data on *unary* diffusion in the porous material.

The *exchange coefficients* $Đ_{ij}$, defined by the first right member equations (S27), are introduced to quantify the coupling between species diffusion. At the molecular level, the $Đ_{ij}$ reflect how the facility for transport of species *i correlates* with that of species *j*.

The Maxwell-Stefan diffusion formulation is consistent with the theory of irreversible thermodynamics. The Onsager Reciprocal Relations imply that the M-S pair diffusivities are symmetric

$$Đ_{ij} = Đ_{ji} \tag{S28}$$

3.2 Thermodynamic correction factors

At thermodynamic equilibrium, the chemical potential of component *i* in the bulk fluid mixture equals the chemical potential of that component in the adsorbed phase. For the bulk fluid phase mixture we have

$$\frac{1}{RT}\frac{\partial \mu_i}{\partial r} = \frac{\partial \ln f_i}{\partial r} = \frac{1}{f_i}\frac{\partial f_i}{\partial r}; \qquad i = 1, 2, ..n \tag{S29}$$

The chemical potential gradients $\partial \mu_i / \partial r$ can be related to the gradients of the molar loadings, q_i, by defining thermodynamic correction factors Γ_{ij}

$$\frac{q_i}{RT}\frac{\partial \mu_i}{\partial r} = \sum_{j=1}^{n} \Gamma_{ij}\frac{\partial q_j}{\partial r}; \quad \Gamma_{ij} = \frac{q_i}{f_i}\frac{\partial f_i}{\partial q_j}; \qquad i, j = 1, ...n \tag{S30}$$

The thermodynamic correction factors Γ_{ij} can be calculated by differentiation of the model describing mixture adsorption equilibrium. Generally speaking, the Ideal Adsorbed Solution Theory (IAST) of Myers and Prausnitz[1] is the preferred method for estimation of mixture adsorption equilibrium. In the special case in which the unary isotherms are described for every component with the 1-site Langmuir model with equal saturation capacities, the mixed-gas Langmuir model

$$\frac{q_i}{q_{sat}} = \theta_i = \frac{b_i f_i}{1 + \sum_{i=1}^{n} b_i f_i}; \quad i = 1, 2, ...n \tag{S31}$$

Is derivable from the IAST. Analytic differentiation of equation (S31) yields

$$\Gamma_{ij} = \delta_{ij} + \left(\frac{\theta_i}{\theta_V}\right); \qquad i, j = 1, 2 \ldots n \tag{S32}$$

where the fractional vacancy θ_V is defined as

$$\theta_V = 1 - \theta_t = 1 - \sum_{i=1}^{n} \theta_i \tag{S33}$$

The elements of the matrix of thermodynamic factors Γ_{ij} can be calculated explicitly from information on the component loadings q_i in the adsorbed phase; this is the persuasive advantage of the use of the mixed-gas Langmuir model. By contrast, the IAST does not allow the calculation of Γ_{ij} explicitly from knowledge on the component loadings q_i in the adsorbed phase; a numerical procedure is required.

3.3 M-S formulation for binary mixture diffusion

For binary mixture diffusion inside microporous crystalline materials the Maxwell-Stefan equations (S27) are written

$$\begin{aligned} -\rho\frac{q_1}{RT}\frac{\partial\mu_1}{\partial r} &= \frac{x_2N_1 - x_1N_2}{Đ_{12}} + \frac{N_1}{Đ_1} \\ -\rho\frac{q_2}{RT}\frac{\partial\mu_2}{\partial r} &= \frac{x_1N_2 - x_2N_1}{Đ_{12}} + \frac{N_2}{Đ_2} \end{aligned} \tag{S34}$$

The first members on the right hand side of Equation (S34) are required to quantify slowing-down effects that characterize binary mixture diffusion.[8, 9, 14] There is no experimental technique for direct determination of the exchange coefficients $Đ_{12}$, that quantify molecule-molecule interactions.

In two-dimensional matrix notation, equation (S30) take the form

$$-\begin{pmatrix} \frac{q_1}{RT}\frac{\partial\mu_1}{\partial r} \\ \frac{q_2}{RT}\frac{\partial\mu_2}{\partial r} \end{pmatrix} = [\Gamma]\begin{pmatrix} \frac{\partial q_1}{\partial r} \\ \frac{\partial q_2}{\partial r} \end{pmatrix} \tag{S35}$$

For the mixed-gas Langmuir model, equation (S31), we can derive simple analytic expressions for the four elements of the matrix of thermodynamic factors:[15]

$$\begin{bmatrix} \Gamma_{11} & \Gamma_{12} \\ \Gamma_{21} & \Gamma_{22} \end{bmatrix} = \frac{1}{1-\theta_1-\theta_2}\begin{bmatrix} 1-\theta_2 & \theta_1 \\ \theta_2 & 1-\theta_1 \end{bmatrix} \tag{S36}$$

where the fractional occupancies, θ_i, are defined by equation (S31).

Let us define the square matrix [B]

$$[B]=\begin{bmatrix} \frac{1}{Đ_1}+\frac{x_2}{Đ_{12}} & -\frac{x_1}{Đ_{12}} \\ -\frac{x_2}{Đ_{12}} & \frac{1}{Đ_2}+\frac{x_1}{Đ_{12}} \end{bmatrix};\quad [B]^{-1}=\frac{1}{1+\frac{x_1Đ_2}{Đ_{12}}+\frac{x_2Đ_1}{Đ_{12}}}\begin{bmatrix} Đ_1\left(1+\frac{x_1Đ_2}{Đ_{12}}\right) & \frac{x_1Đ_1Đ_2}{Đ_{12}} \\ \frac{x_2Đ_1Đ_2}{Đ_{12}} & Đ_2\left(1+\frac{x_2Đ_1}{Đ_{12}}\right) \end{bmatrix} \tag{S37}$$

In proceeding further, it is convenient to define a 2×2 dimensional square matrix $[\Lambda]$:

$$[\Lambda]=\begin{bmatrix} \frac{1}{Đ_1}+\frac{x_2}{Đ_{12}} & -\frac{x_1}{Đ_{12}} \\ -\frac{x_2}{Đ_{12}} & \frac{1}{Đ_2}+\frac{x_1}{Đ_{12}} \end{bmatrix}^{-1}=\frac{1}{1+\frac{x_1Đ_2}{Đ_{12}}+\frac{x_2Đ_1}{Đ_{12}}}\begin{bmatrix} Đ_1\left(1+\frac{x_1Đ_2}{Đ_{12}}\right) & \frac{x_1Đ_1Đ_2}{Đ_{12}} \\ \frac{x_2Đ_1Đ_2}{Đ_{12}} & Đ_2\left(1+\frac{x_2Đ_1}{Đ_{12}}\right) \end{bmatrix} \tag{S38}$$

Equation (S34) can be re-cast into 2-dimensional matrix notation

$$(N)=-\rho[\Lambda][\Gamma]\frac{\partial(q)}{\partial r};$$

$$\begin{pmatrix} N_1 \\ N_2 \end{pmatrix}=-\frac{\rho}{1+\frac{x_1Đ_2}{Đ_{12}}+\frac{x_2Đ_1}{Đ_{12}}}\begin{bmatrix} Đ_1\left(1+\frac{x_1Đ_2}{Đ_{12}}\right) & \frac{x_1Đ_1Đ_2}{Đ_{12}} \\ \frac{x_2Đ_1Đ_2}{Đ_{12}} & Đ_2\left(1+\frac{x_2Đ_1}{Đ_{12}}\right) \end{bmatrix}\begin{bmatrix} \Gamma_{11} & \Gamma_{12} \\ \Gamma_{21} & \Gamma_{22} \end{bmatrix}\begin{pmatrix} \frac{\partial q_1}{\partial r} \\ \frac{\partial q_2}{\partial r} \end{pmatrix} \tag{S39}$$

The elements of $[B]$ can be obtained by inverting the matrix $[\Lambda]$:

$$\begin{bmatrix} B_{11} & B_{12} \\ B_{21} & B_{22} \end{bmatrix}=\begin{bmatrix} \frac{1}{Đ_1}+\frac{x_2}{Đ_{12}} & -\frac{x_1}{Đ_{12}} \\ -\frac{x_2}{Đ_{12}} & \frac{1}{Đ_2}+\frac{x_1}{Đ_{12}} \end{bmatrix}=[\Lambda]^{-1} \tag{S40}$$

3.4 Negligible correlations scenario for M-S diffusivities

For values of $Đ_1/Đ_{12}\to 0$, and $Đ_2/Đ_{12}\to 0$, the contribution of the first right member of M-S Equation (S34) can be ignored and correlations can be considered to be of negligible importance; we derive

$$\frac{Đ_1}{Đ_{12}} \to 0; \quad \frac{Đ_2}{Đ_{12}} \to 0; \quad \begin{bmatrix} \Lambda_{11} & \Lambda_{12} \\ \Lambda_{21} & \Lambda_{22} \end{bmatrix} \to \begin{bmatrix} Đ_1 & 0 \\ 0 & Đ_2 \end{bmatrix}$$

$$\begin{pmatrix} N_1 \\ N_2 \end{pmatrix} = -\rho \begin{bmatrix} Đ_1 & 0 \\ 0 & Đ_2 \end{bmatrix} \begin{bmatrix} \Gamma_{11} & \Gamma_{12} \\ \Gamma_{21} & \Gamma_{22} \end{bmatrix} \begin{pmatrix} \frac{\partial q_1}{\partial r} \\ \frac{\partial q_2}{\partial r} \end{pmatrix} \tag{S41}$$

Equation (S41) is valid, as a first approximation, for diffusion in cage-type zeolites with 8-ring windows (CHA, LTA, DDR, ERI) and ZIF-8.[10, 16-22] When correlation effects are negligible, the diffusional coupling effects are solely traceable to mixture adsorption thermodynamics, embodied in the matrix $[\Gamma]$.

4 Quasi-Chemical Theory for Occupancy Dependence of Unary Diffusivity

The simplest model to describe this occupancy dependence is

$$Đ_i = Đ_i(0)\left(1-\theta\right) = Đ_i(0)\theta_V \tag{S42}$$

where $Đ_i(0)$ is the M-S diffusivity at "zero-loading", and $\theta_V = \left(1-\theta\right)$ is the fractional vacancy, determined from Equation (S11), where the saturation capacity is determined from the unary isotherm fits. Equation (S42) is essentially based on a simple hopping model in which a molecule can jump from one adsorption site to an adjacent one, provided it is not already occupied. The loading dependence portrayed in equation (S42) has been termed the "strong confinement" scenario by Krishna and Baur.[15]

For the specific case of a binary mixture, the hopping of molecules from one site to another on a 2D lattice is depicted in Figure S1. Using a simple lattice model, the M-S diffusivity in the limit of vanishingly small occupancies, $Đ_i(0) = \frac{1}{\zeta}\nu_i(0)\lambda^2$, where $\zeta = 4$ is the coordination number of the 2D array of lattice sites, λ is the jump distance on the square lattice, and $\nu_i(0)$ is the jump frequency at vanishingly small occupancy.[23]

More generally, molecule-molecule interactions serve to influence the jump frequencies by a factor that depends on the energy of interaction, *w*. For repulsive interactions, $w > 0$, whereas for attractive interactions, $w < 0$. Using the quasi-chemical approach of Reed and Ehrlich[24] to quantify such interactions, the following expression is obtained for the occupancy dependence of the M-S diffusivities [23, 25, 26]

$$Đ_i = Đ_i(0)\left(\frac{1+\beta_i}{2\,(1-\theta_i)}\right)^{-\zeta}\left(1+\frac{(\beta_i-1+2\theta_i)\phi}{2\,(1-\theta_i)}\right)^{\zeta-1} \tag{S43}$$

where the following dimensionless parameters are defined

$$\beta_i = \sqrt{1 - 4\,\theta_i(1-\theta_i)(1-1/\phi)}; \quad \phi = \exp(w/RT) \tag{S44}$$

In the limiting case of negligible molecule-molecule interactions, $w = 0$, $\phi = 1$, $\beta_i = 1$ equations (S43), and (S44) degenerate to yield Equation (S42).

4.1 List of Figures for Quasi-Chemical Theory for Occupancy Dependence of Unary Diffusivity

$$-\frac{d\mu_1}{dz} = -RT\frac{d\ln p_1}{dz} = \frac{RT}{Đ_{12}}\theta_2(u_1-u_2)+\frac{RT}{Đ_{1V}}\theta_V(u_1-u_V)$$

$$-\frac{d\mu_2}{dz} = -RT\frac{d\ln p_2}{dz} = \frac{RT}{Đ_{12}}\theta_1(u_2-u_1)+\frac{RT}{Đ_{2V}}\theta_V(u_2-u_V)$$

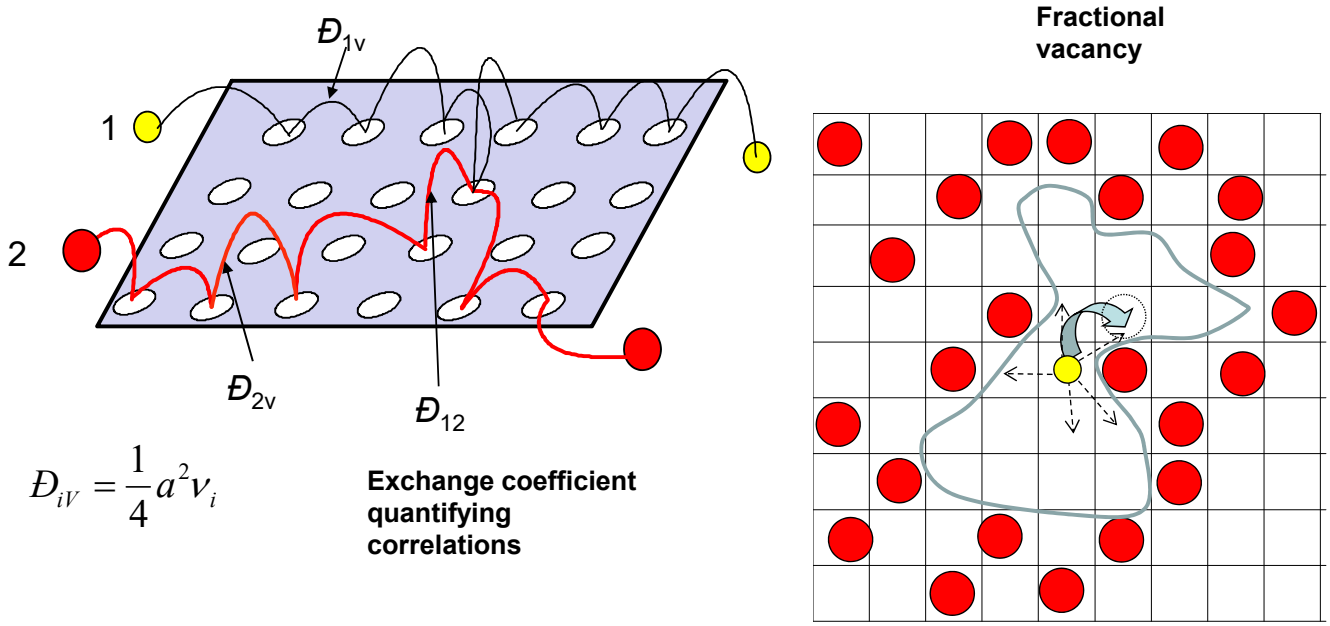

$$Đ_{iV} = \frac{1}{4}a^2\nu_i$$

Figure S1. The Maxwell- Stefan description of hopping of molecules on a 2D surface.

5 SAPO-34 membrane permeation

SAPO-34 has the same structural topology as CHA zeolite, consisting of cages of volume 316 Å^3, separated by 3.8 Å × 4.2 Å 8-ring windows; the pore landscape and structural details are provided in Figure S2, and Figure S3.[27-30]

For adsorption in SAPO-34, the model based on statistical thermodynamics described in Chapter 3 of Ruthven[2] is particularly relevant and useful

$$q_i = \frac{q_{i,sat}}{\Omega_i} \frac{b_i f_i + \sum_{m=2}^{\Omega_i} \frac{(b_i f_i)^m}{(m-1)!} \left[\frac{1 - \frac{m}{\Omega_i + 1}}{1 - \frac{1}{\Omega_i + 1}} \right]^m}{1 + b_i f_i + \sum_{m=2}^{\Omega_i} \frac{(b_i f_i)^m}{(m)!} \left[\frac{1 - \frac{m}{\Omega_i + 1}}{1 - \frac{1}{\Omega_i + 1}} \right]^m} \tag{S45}$$

In Equation (S45) q_i represents the loading in mol kg^{-1}, $q_{i,sat}$ is the saturation loading in mol kg^{-1}, and Ω_i is maximum capacity expressed in molecules per cage. Based on the atomic composition of SAPO-34 used in our experiments of Li et al.,[31] $(Si_{0.061}Al_{0.483}P_{0.455})O_2$, we calculate $q_{i,sat} = 1.369\Omega_i$.

The unary isotherms fit parameters are provided in Table S1.

The mixture adsorption equilibrium was determined using the IAST.

Experimental data of Li et al.[31-33] for component permeances for CO_2/CH_4, CO_2/H_2, CO_2/N_2, CH_4/H_2, CH_4/N_2, CH_4/Ar, and N_2/H_2 mixtures in SAPO-34 membrane at 295 K are compared to unary permeation data in Figure S4, Figure S5, Figure S6, Figure S7, Figure S8,Figure S9, Figure S10. The permeance data are plotted as function of (a) upstream partial pressures, p_{i0}, (b) adsorption potential $\pi A/RT$ and (c) occupancy θ at the upstream face of the membrane.

Experimental data of Li et al.[31-33] for permeances of CO_2, CH_4, N_2, and H_2 determined for unary and equimolar binary mixture permeation across SAPO-34 membrane at 295 K are presented in Figure S11

and Figure S12. The data are plotted, respectively, as function of the adsorption potential $\pi A/RT$ and occupancy θ at the upstream face of the membrane.

From the experimental data on the component permeances, the transport coefficients $\rho Đ_i/\delta$ can be backed-out; details of the backing-out procedure are provided in Li et al.[31-33]. Figure S13 presents plots of the transport coefficients $\rho Đ_i/\delta$, with units kg m^{-2} s^{-1}, of CO_2, CH_4, N_2, and H_2 determined for unary and equimolar binary mixture permeation across SAPO-34 membrane at 295 K. The data are plotted as function of the occupancy θ at the upstream face of the membrane. The continuous solid lines are the Reed-Ehrlich[24] model calculations that quantifies the occupancy dependence of the transport coefficients.

The continuous solid lines in Figure S13 are fits of the experimental data on transport coeffficients by fitting the sets of parameters: $\rho Đ_i(0)/\delta$, and $\phi = \phi_0 \exp(-a\theta)$. For all four guest molecules in SAPO-34, equations (S43), and (S44) degenerate provide good descriptions of the occupancy dependence.

5.1 List of Tables for SAPO-34 membrane permeation

Table S1. Pure component isotherm fit data for guest species in SAPO-34, as tabulated in Li et al.[31]

Molecule	b_i	Ω_i	$q_{i,sat}$
CO_2	7.67×10^{-5}	6	8.2
CH_4	5.87×10^{-6}	6	8.2
N_2	1.26×10^{-6}	6	8.2
H_2	2.84×10^{-7}	9	12.3
O_2	1.2×10^{-6}	6	8.2
CO	2.31×10^{-6}	6	8.2
Ar	1.26×10^{-6}	6	8.2

b_i is expressed in Pa^{-1}, Ω_i in molecules per cage, $q_{i,sat}$ in mol kg^{-1}.

5.2 List of Figures for SAPO-34 membrane permeation

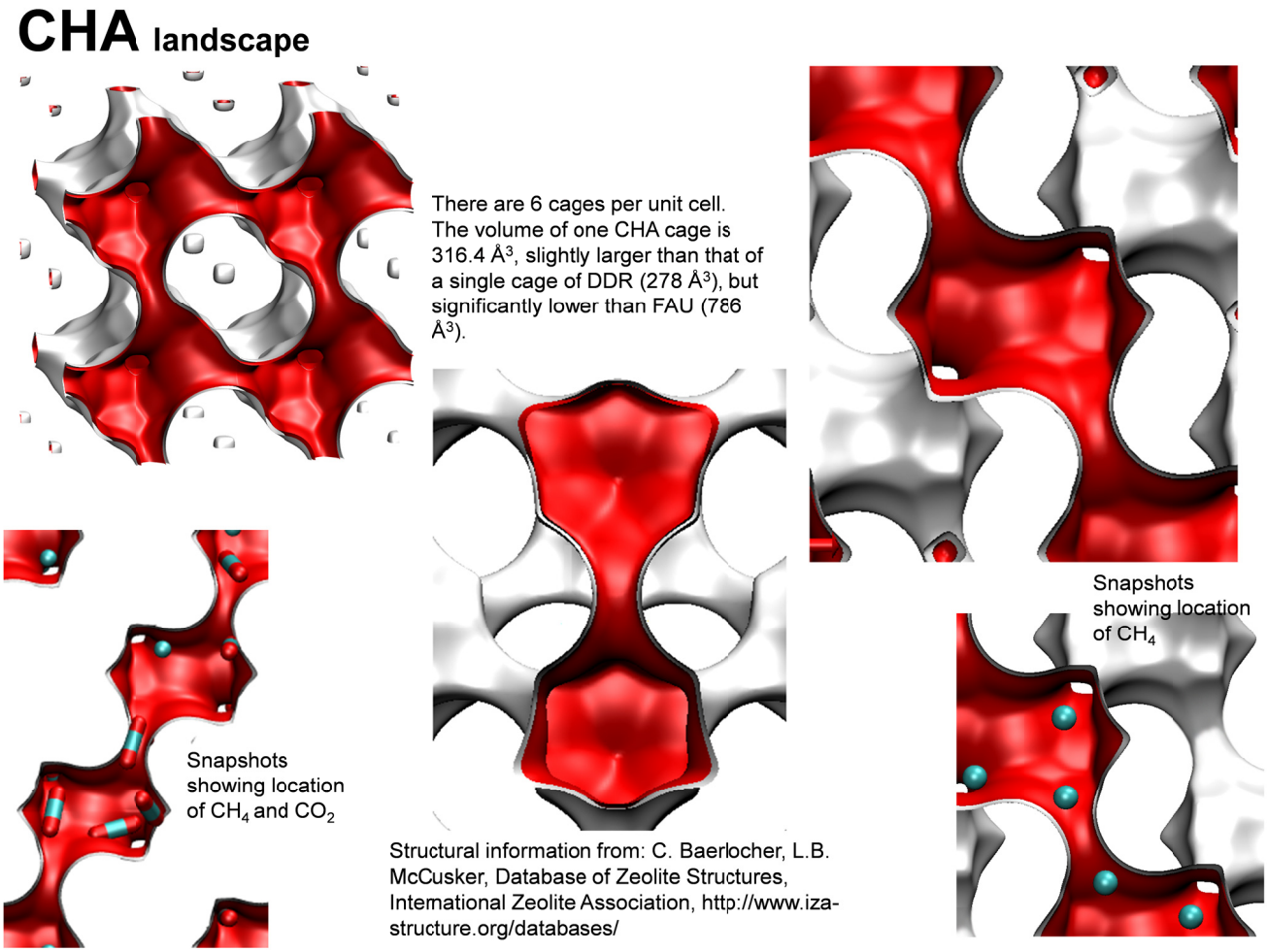

Figure S2. Pore landscape and structural details of all-silica CHA zeolite.

CHA window and pore dimensions

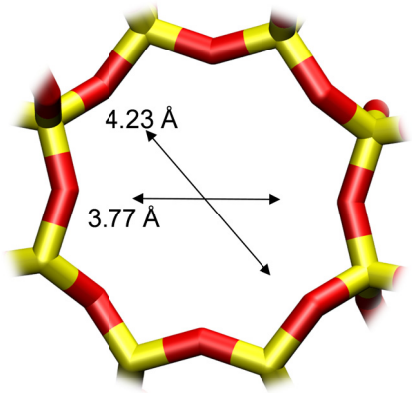

CHA

The window dimensions calculated using the van der Waals diameter of framework atoms = 2.7 Å are indicated above by the arrows.

	CHA
a /Å	15.075
b /Å	23.907
c /Å	13.803
Cell volume / Å^3	4974.574
conversion factor for [molec/uc] to [mol per kg Framework]	0.2312
conversion factor for [molec/uc] to [kmol/m^3]	0.8747
ρ [kg/m3]	1444.1
MW unit cell [g/mol(framework)]	4326.106
ψ, fractional pore volume	0.382
open space / Å^3/uc	1898.4
Pore volume / cm^3/g	0.264
Surface area /m^2/g	758.0
DeLaunay diameter /Å	3.77

Figure S3. Pore landscape and structural details of all-silica CHA zeolite.

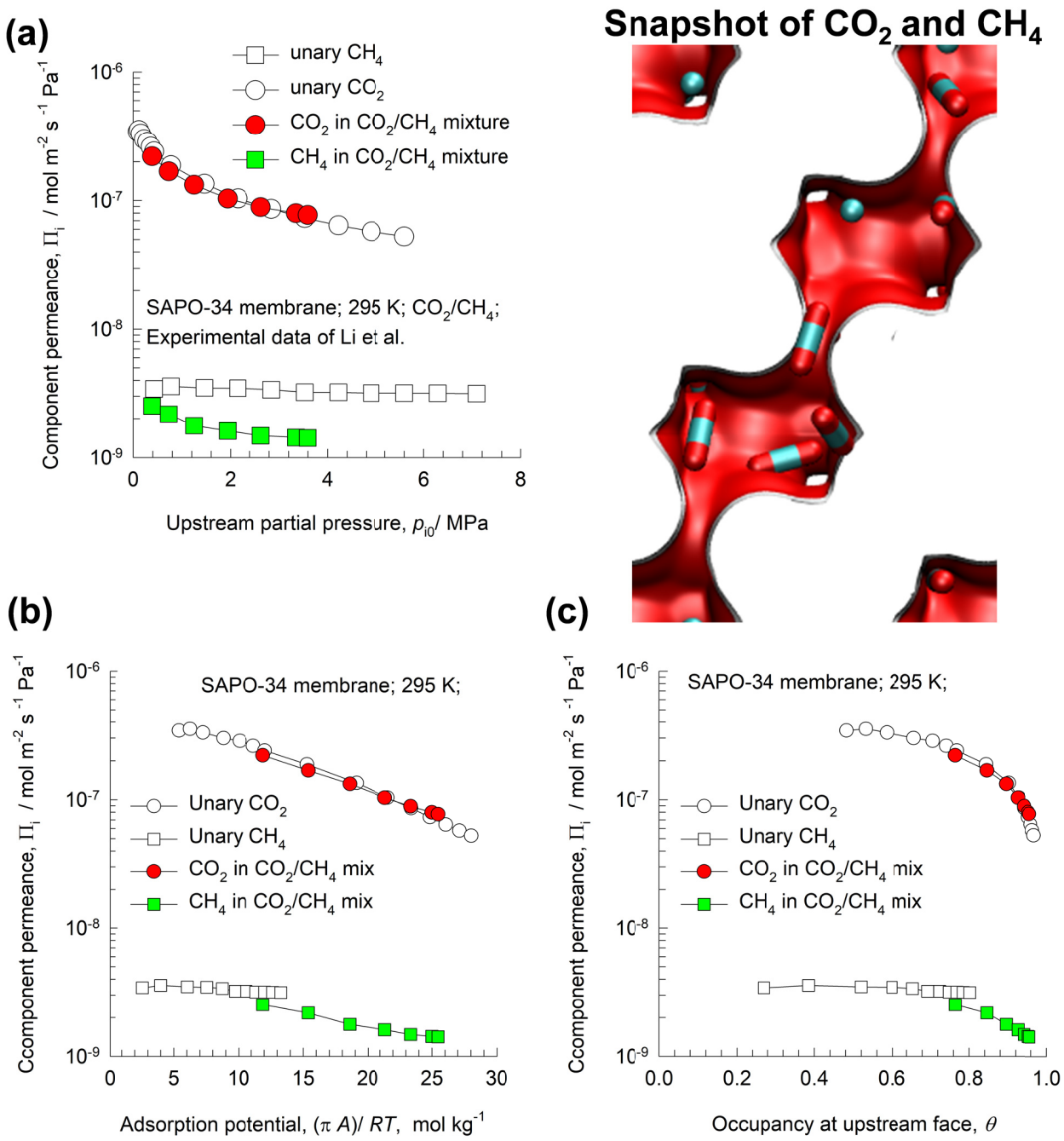

Figure S4. Experimental data of Li et al.[31-33] for component permeances for CO_2/CH_4 mixtures in SAPO-34 membrane at 295 K, compared to unary permeation data. The data are plotted as function of (a) upstream partial pressures, p_{i0}, (b) adsorption potential $\pi A/RT$ and (c) occupancy θ at the upstream face of the membrane.

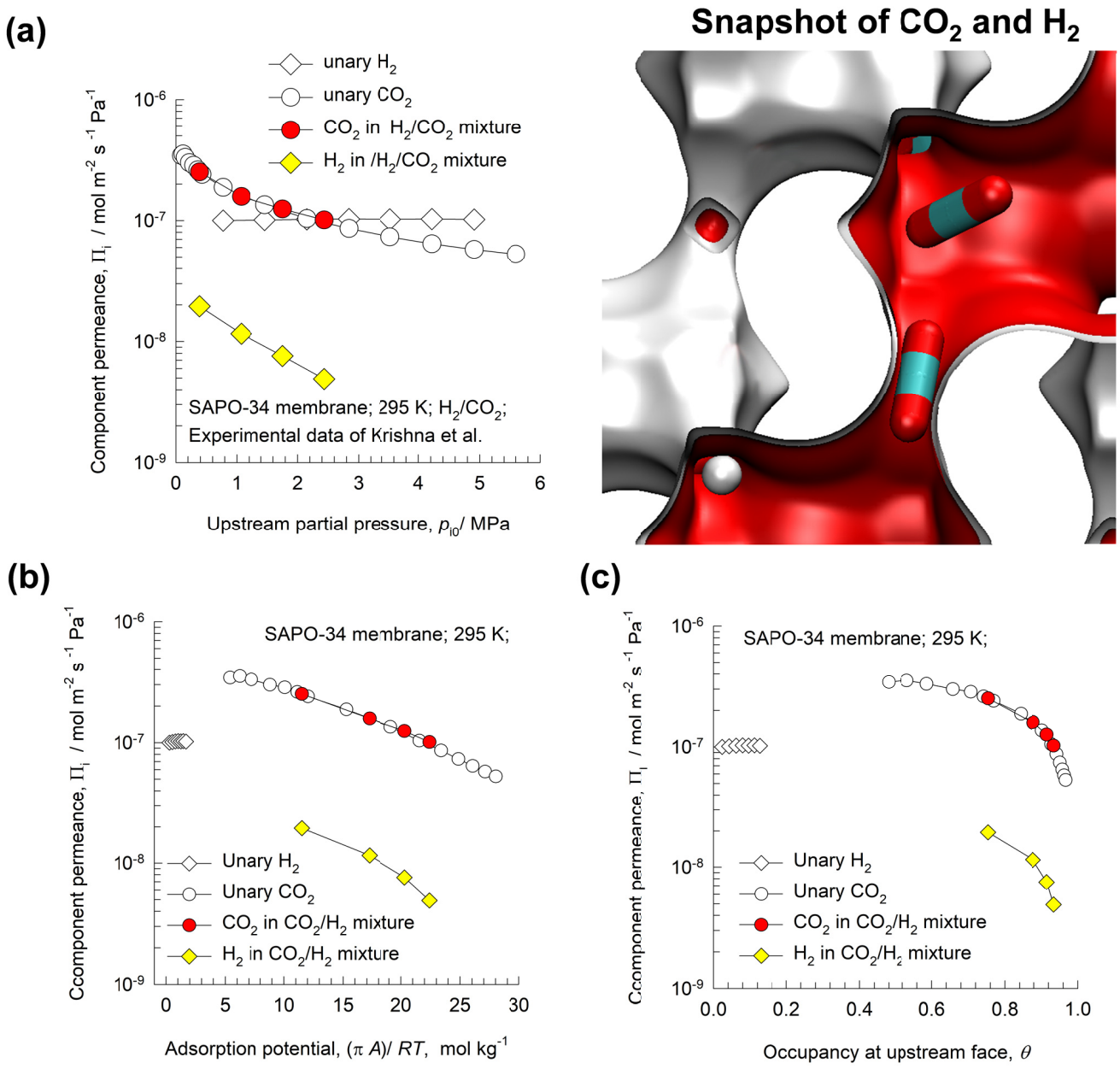

Figure S5. Experimental data of Li et al.[31-33] for component permeances for CO_2/H_2 mixtures in SAPO-34 membrane at 295 K, compared to unary permeation data. The data are plotted as function of (a) upstream partial pressures, p_{i0}, (b) adsorption potential $\pi A/RT$ and (c) occupancy θ at the upstream face of the membrane.

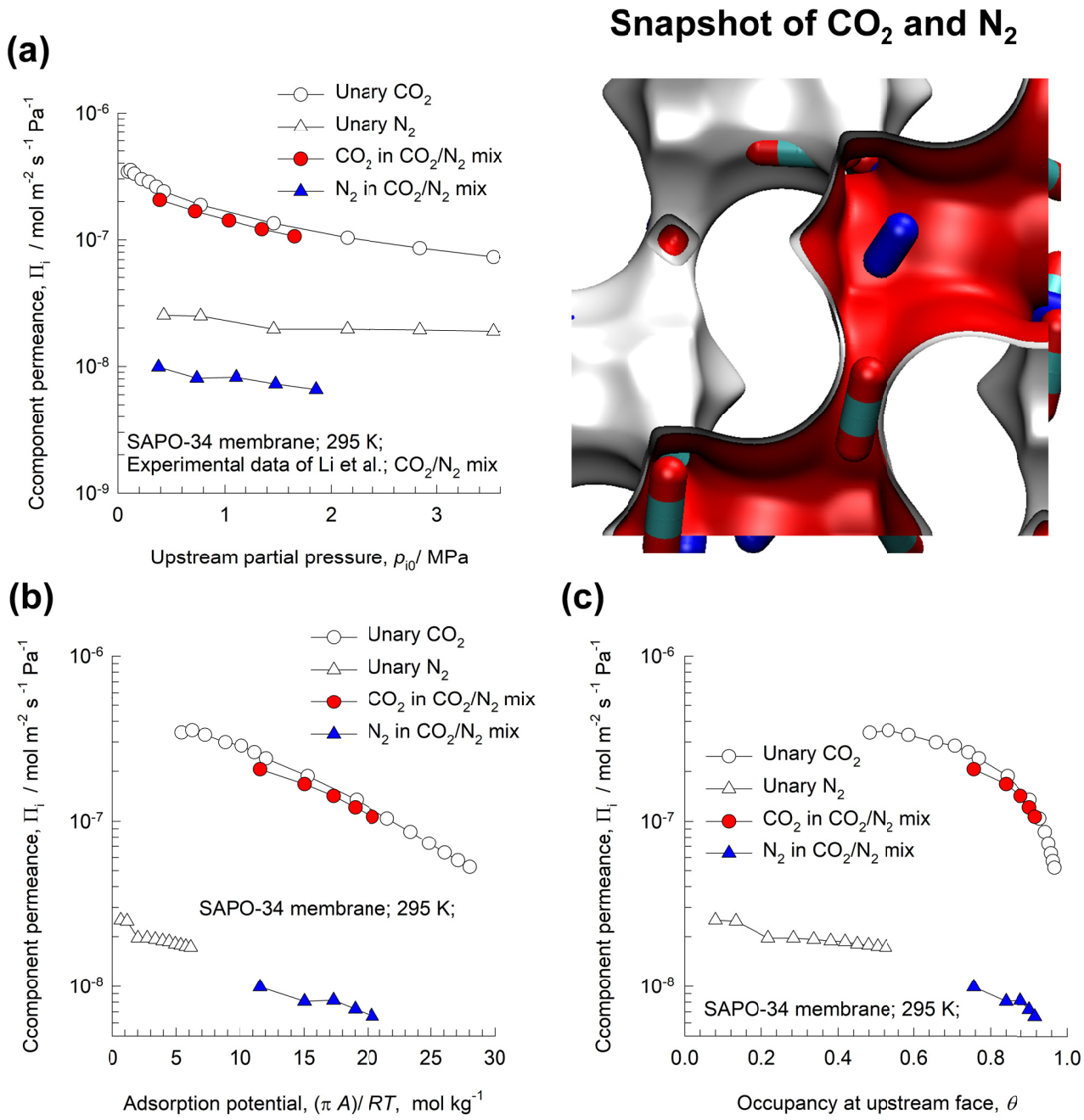

Figure S6. Experimental data of Li et al.[31-33] for component permeances for CO_2/N_2 mixtures in SAPO-34 membrane at 295 K, compared to unary permeation data. The data are plotted as function of (a) upstream partial pressures, p_{i0}, (b) adsorption potential $\pi A/RT$ and (c) occupancy θ at the upstream face of the membrane.

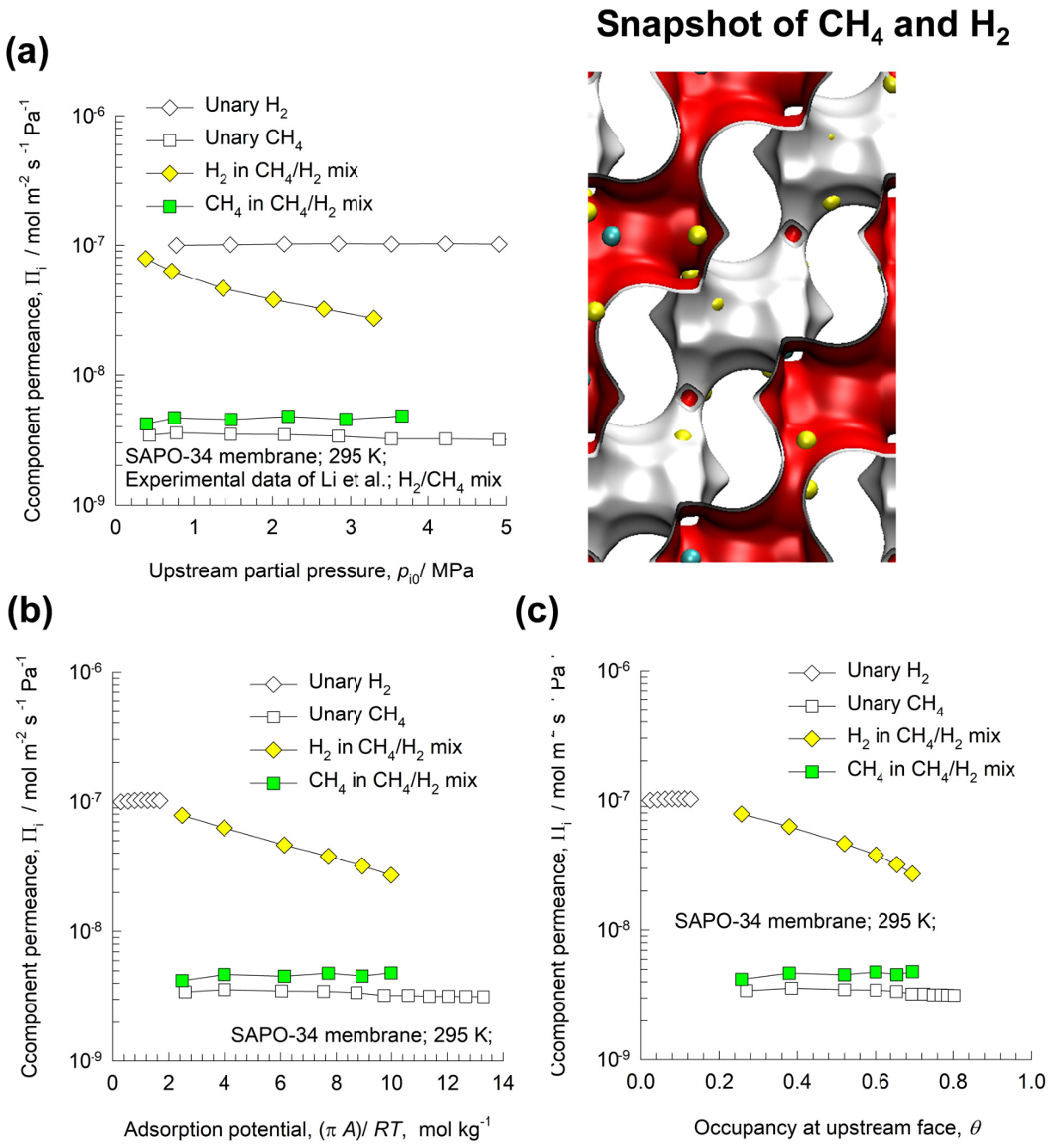

Figure S7. Experimental data of Li et al.[31-33] for component permeances for CH_4/H_2 mixtures in SAPO-34 membrane at 295 K, compared to unary permeation data. The data are plotted as function of (a) upstream partial pressures, p_{i0}, (b) adsorption potential $\pi A/RT$ and (c) occupancy θ at the upstream face of the membrane.

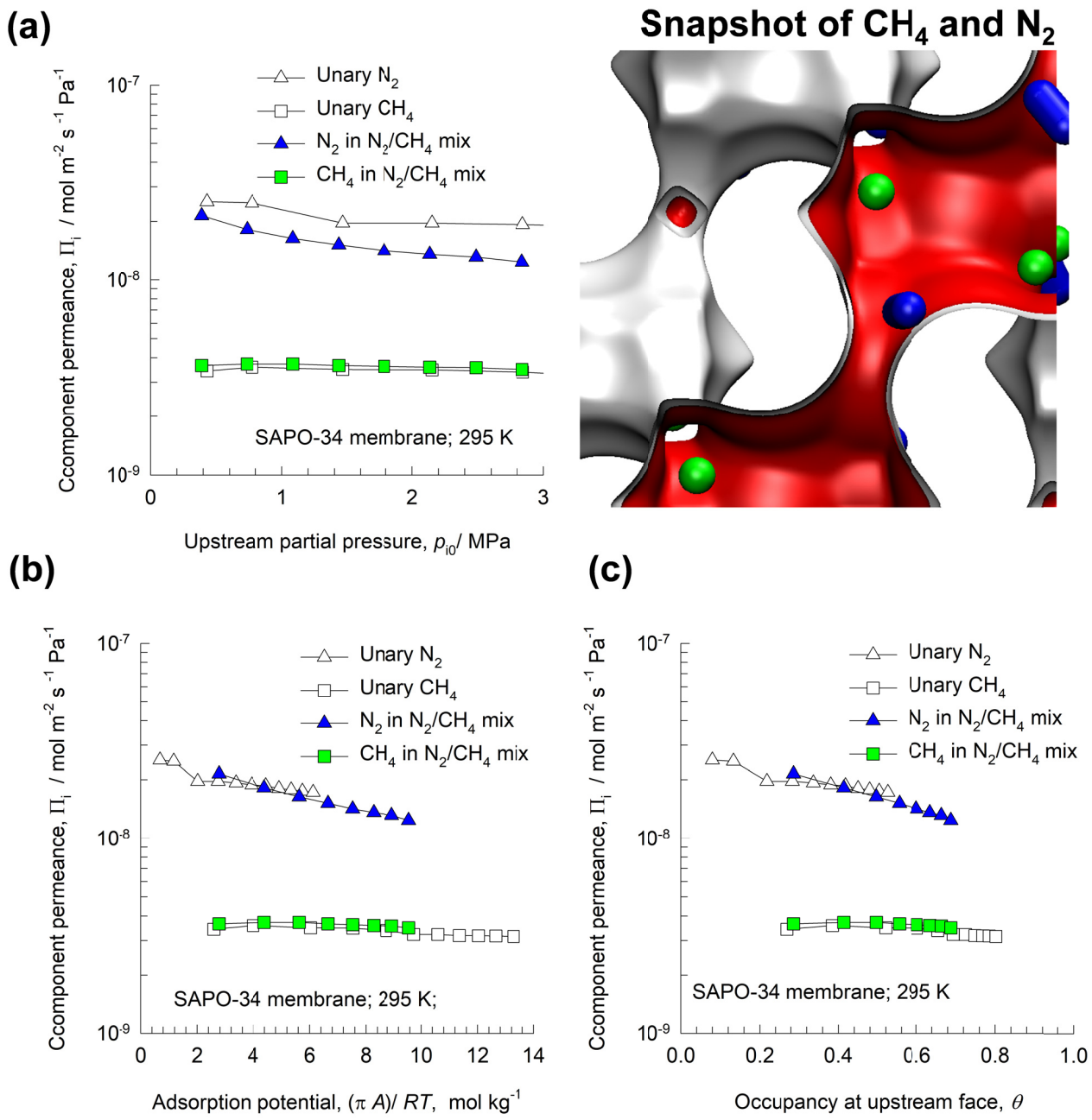

Figure S8. Experimental data of Li et al.[31-33] for component permeances for CH_4/N_2 mixtures in SAPO-34 membrane at 295 K, compared to unary permeation data. The data are plotted as function of (a) upstream partial pressures, p_{i0}, (b) adsorption potential $\pi A/RT$ and (c) occupancy θ at the upstream face of the membrane.

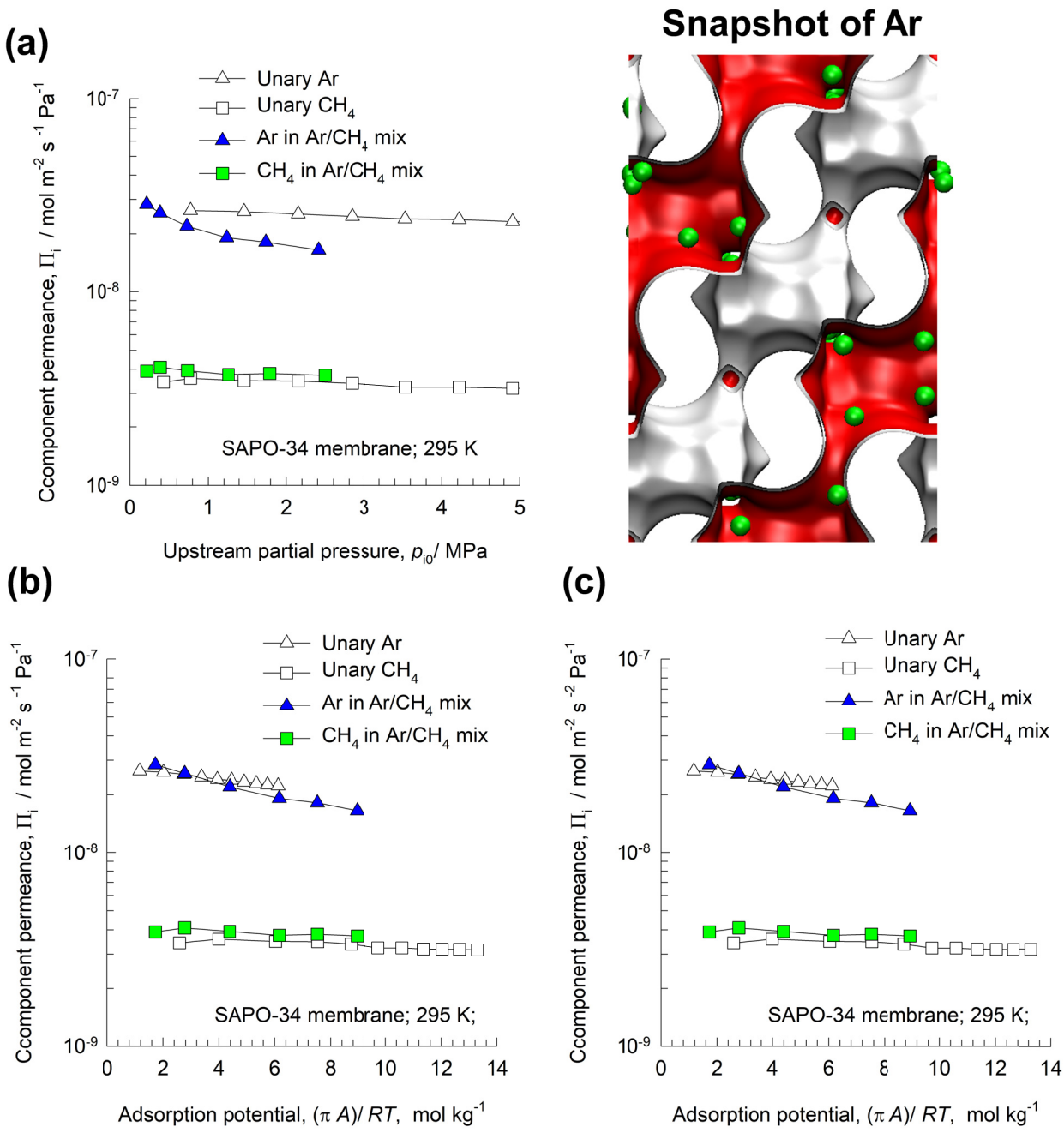

Figure S9. Experimental data of Li et al.[31-33] for component permeances for CH_4/Ar mixtures in SAPO-34 membrane at 295 K, compared to unary permeation data. The data are plotted as function of (a) upstream partial pressures, p_{i0}, (b) adsorption potential $\pi A/RT$ and (c) occupancy θ at the upstream face of the membrane.

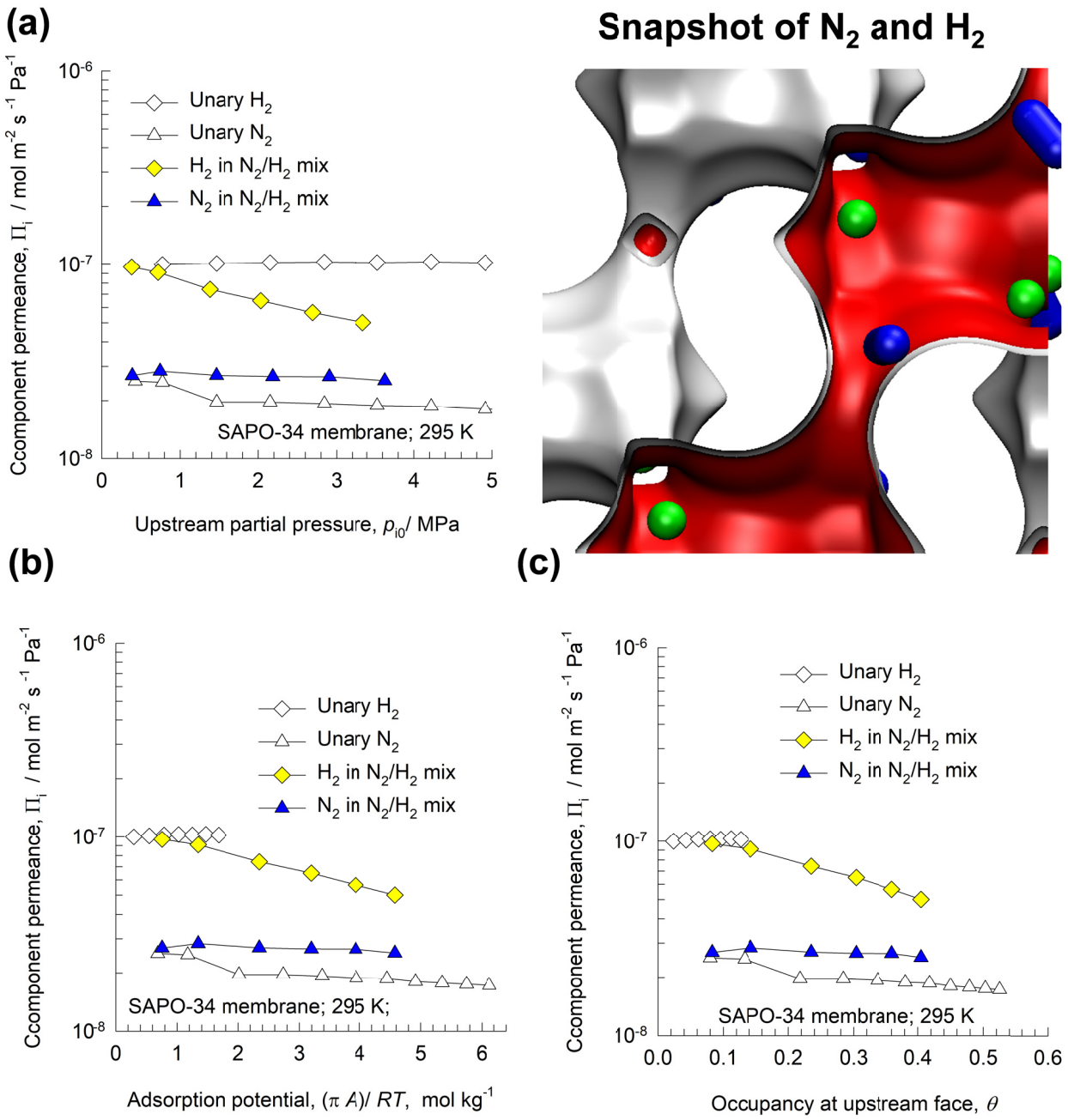

Figure S10. Experimental data of Li et al.[31-33] for component permeances for N_2/H_2 mixtures in SAPO-34 membrane at 295 K, compared to unary permeation data. The data are plotted as function of (a) upstream partial pressures, p_{i0}, (b) adsorption potential $\pi A/RT$ and (c) occupancy θ at the upstream face of the membrane.

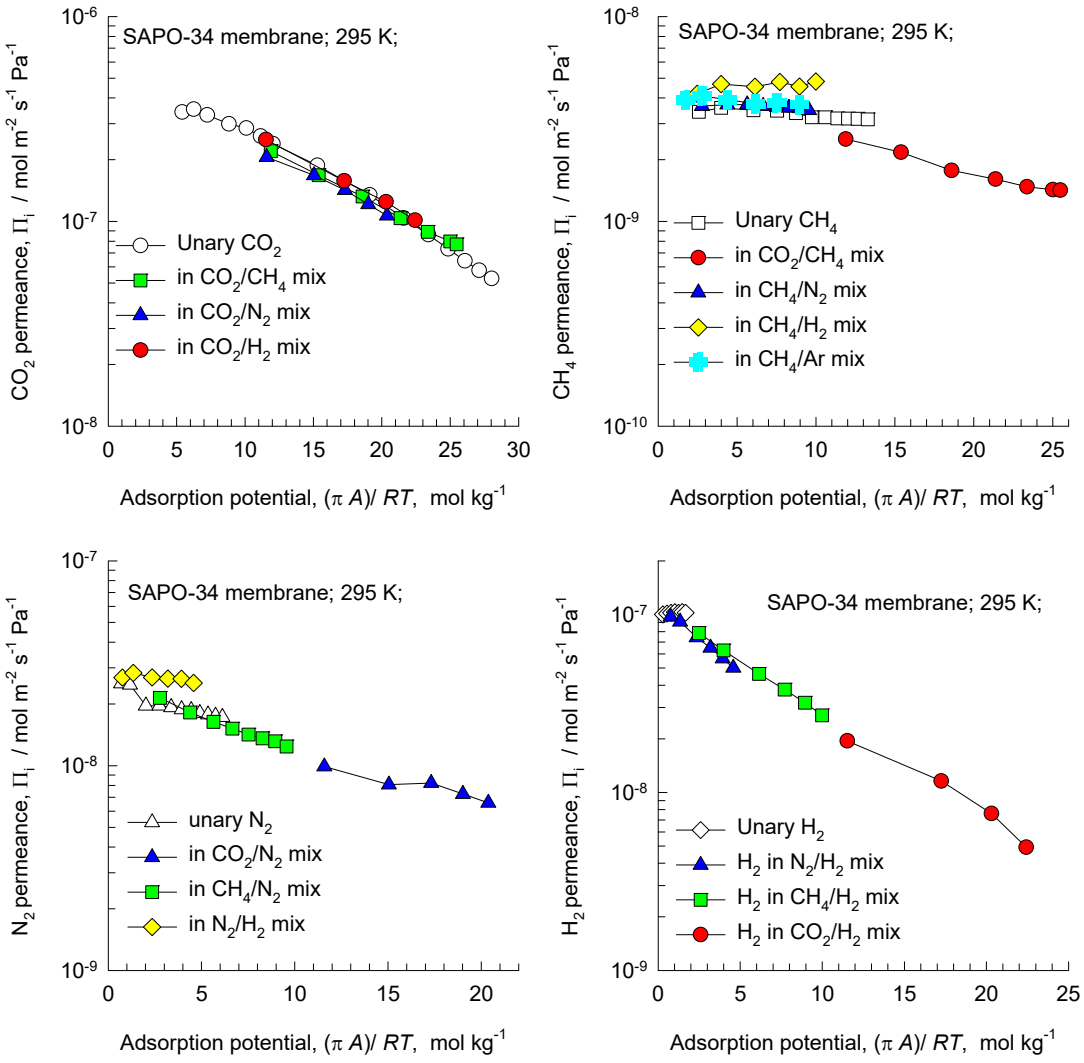

Figure S11. Experimental data of Li et al.[31-33] for permeances of CO_2, CH_4, N_2, and H_2 determined for unary and equimolar binary mixture permeation across SAPO-34 membrane at 295 K. The data are plotted as function of the adsorption potential $\pi A/RT$ at the upstream face of the membrane.

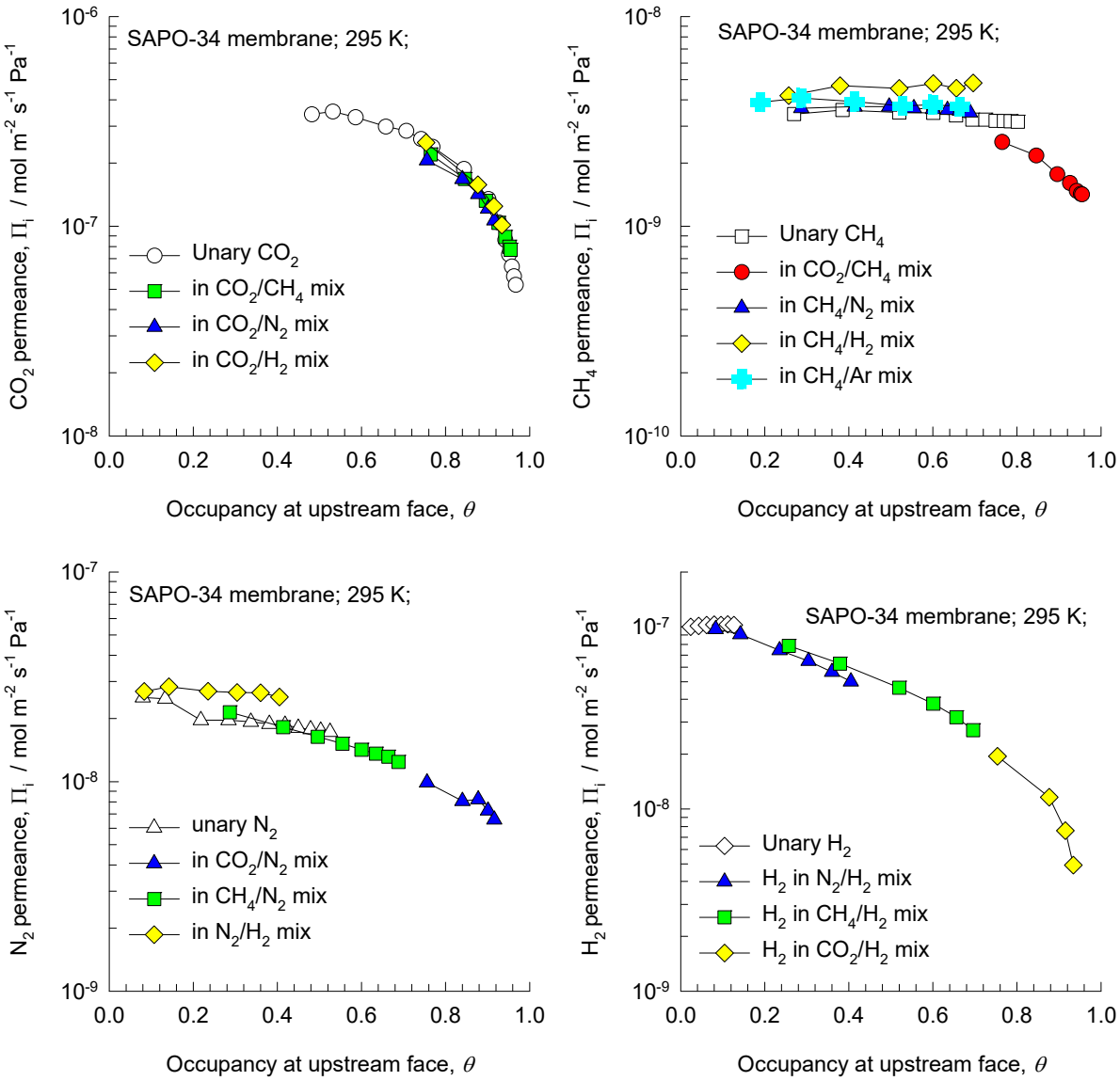

Figure S12. Experimental data of Li et al.[31-33] for permeances of CO_2, CH_4, N_2, and H_2 determined for unary and equimolar binary mixture permeation across SAPO-34 membrane at 295 K. The data are plotted as function of the occupancy θ at the upstream face of the membrane.

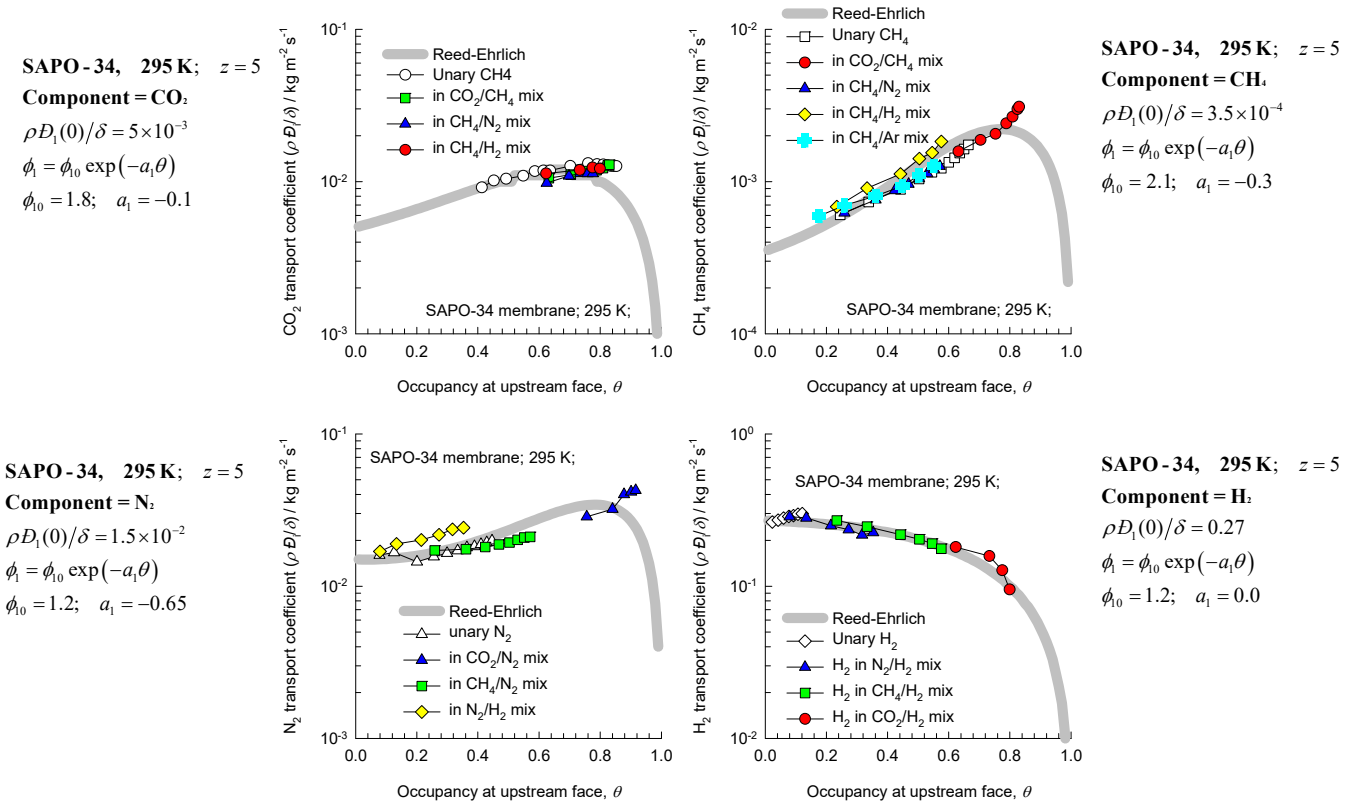

Figure S13. Experimental data of Li et al.[31-33] for transport coefficients $\rho \mathcal{D}_i/\delta$ of CO_2, CH_4, N_2, and H_2 determined for unary and equimolar binary mixture permeation across SAPO-34 membrane at 295 K. The data are plotted as function of the occupancy θ at the upstream face of the membrane. The continuous solid lines are the Reed-Ehrlich model calculations, equations (S43), and (S44), with the parameters as indicated alongside the corresponding Figures.

6 DDR membrane permeation

DDR consists of cages of 277.8 Å^3 volume, separated by 3.65 Å × 4.37 Å 8-ring windows; the pore landscapes and structural details are provided in Figure S14, and Figure S15. The guest molecules jump one-at-a-time across the narrow 8-ring windows.

CBMC simulations of the unary isotherm data for CO_2, CH_4, and N_2 for a variety of temperatures were fitted with a 3-site Langmuir model in previous work; see Figure S16, and Figure S17.[19] The 3-site Langmuir parameters are provided in Table S2. The CBMC simulations are in very good agreement with the experimental data of Himeno et al.;[34-36] see comparisons in Figure S16.

Experimental data of Van den Bergh et al.[37, 38] for component permeances for 50/50 CO_2/CH_4, and 50/50 N_2/CH_4 mixtures in DDR membrane at 303 K are compared to unary permeation data in Figure S18, and Figure S19. The permeance data are plotted as function of (a) upstream partial pressures, p_{i0}, (b) adsorption potential $\pi A/RT$ and (c) occupancy θ at the upstream face of the membrane.

Figure S20 presents a comparison of CH_4 component permeances for 50/50 CO_2/CH_4 and 50/50 N_2/CH_4 binary mixture permeation across DDR membrane at 303 K, compared to unary permeance. The data are plotted as function of the adsorption potential $\pi A/RT$ and occupancy θ at the upstream face of the membrane.

Figure S21 presents experimental data of Himeno et al.[35] for component permeances for 50/50 CO_2/CH_4 binary mixture permeation across DDR membrane at 298 K, compared to unary permeation data. The data are plotted as function of (a) upstream partial pressures, p_{i0}, (b) adsorption potential $\pi A/RT$ and (c) occupancy θ at the upstream face of the membrane.

When compared at the same adsorption potential, or occupancy, the component permeances are the same for mixtures as for unary systems.

6.1 List of Tables for DDR membrane permeation

Table S2. Temperature dependent 3-site Langmuir parameters for CO_2, CH_4, and N_2 in DDR. The fits are those reported in the Supplementary Material accompanying Krishna and van Baten.[19]

$$q = \frac{q_{sat,A} b_A f}{1 + b_A f} + \frac{q_{sat,B} b_B f}{1 + b_B f} + \frac{q_{sat,C} b_C f}{1 + b_C f}$$

For CO_2: $b_A = 7.8 \times 10^{-11} \exp(\frac{3400}{T})$; $q_{sat,A} = 3.0$ mol/kg;

$b_B = 2 \times 10^{-13} \exp(\frac{3800}{T})$; $q_{sat,B} = 1.0$ mol/kg; $b_C = 1.9 \times 10^{-14} \exp(\frac{3450}{T})$; $q_{sat,C} = 0.6$ mol/kg

For CH_4: $b_A = 2.39 \times 10^{-9} \exp(\frac{2200}{T})$; $q_{sat,A} = 1.6$ mol/kg;

$b_B = 1.24 \times 10^{-11} \exp(\frac{2200}{T})$; $q_{sat,B} = 1.6$ mol/kg; $b_C = 1.27 \times 10^{-12} \exp(\frac{1000}{T})$; $q_{sat,C} = 1.0$ mol/kg

For N_2: $b_A = 1.57 \times 10^{-9} \exp(\frac{1650}{T})$; $q_{sat,A} = 1.8$ mol/kg;

$b_B = 4.5 \times 10^{-11} \exp(\frac{1650}{T})$; $q_{sat,B} = 1.8$ mol/kg; $b_C = 3 \times 10^{-13} \exp(\frac{1650}{T})$; $q_{sat,C} = 1.8$ mol/kg

6.2 List of Figures for DDR membrane permeation

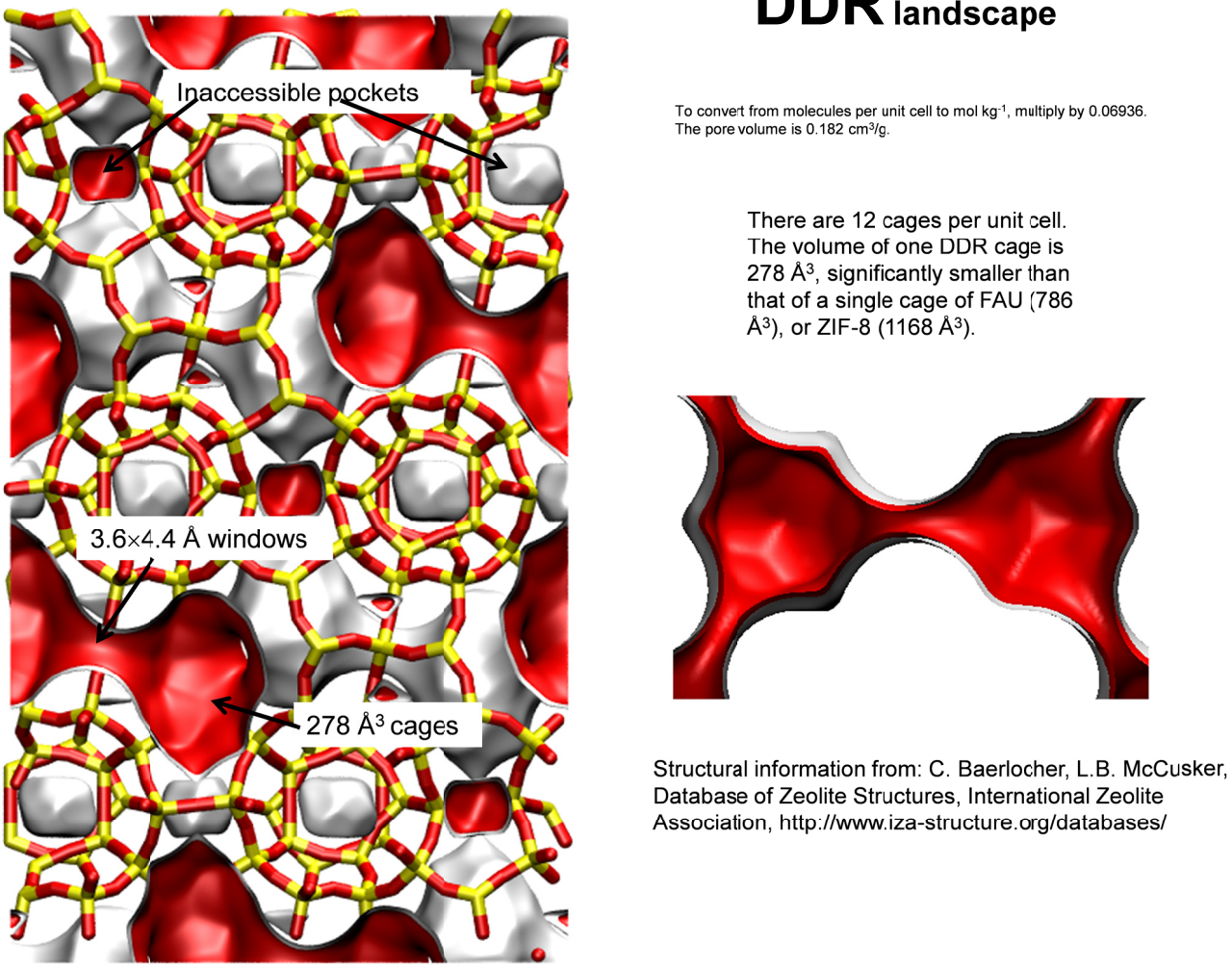

Figure S14. Pore landscape of all-silica DDR zeolite.

DDR window and pore dimensions

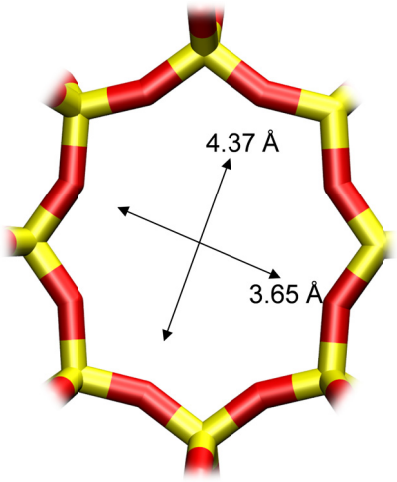

DDR

The window dimensions calculated using the van der Waals diameter of framework atoms = 2.7 Å are indicated above by the arrows.

	DDR
a /Å	24.006
b /Å	13.86
c /Å	40.892
Cell volume / Å^3	13605.72
conversion factor for [molec/uc] to [mol per kg Framework]	0.0693
conversion factor for [molec/uc] to [kmol/m^3]	0.4981
ρ [kg/m3]	1759.991
MW unit cell [g/mol(framework)]	14420.35
ϕ, fractional pore volume	0.245
open space / Å^3/uc	3333.5
Pore volume / cm^3/g	0.139
Surface area /m^2/g	350.0
DeLaunay diameter /Å	3.65

Figure S15. Structural details of all-silica DDR zeolite.

DDR membrane permeation

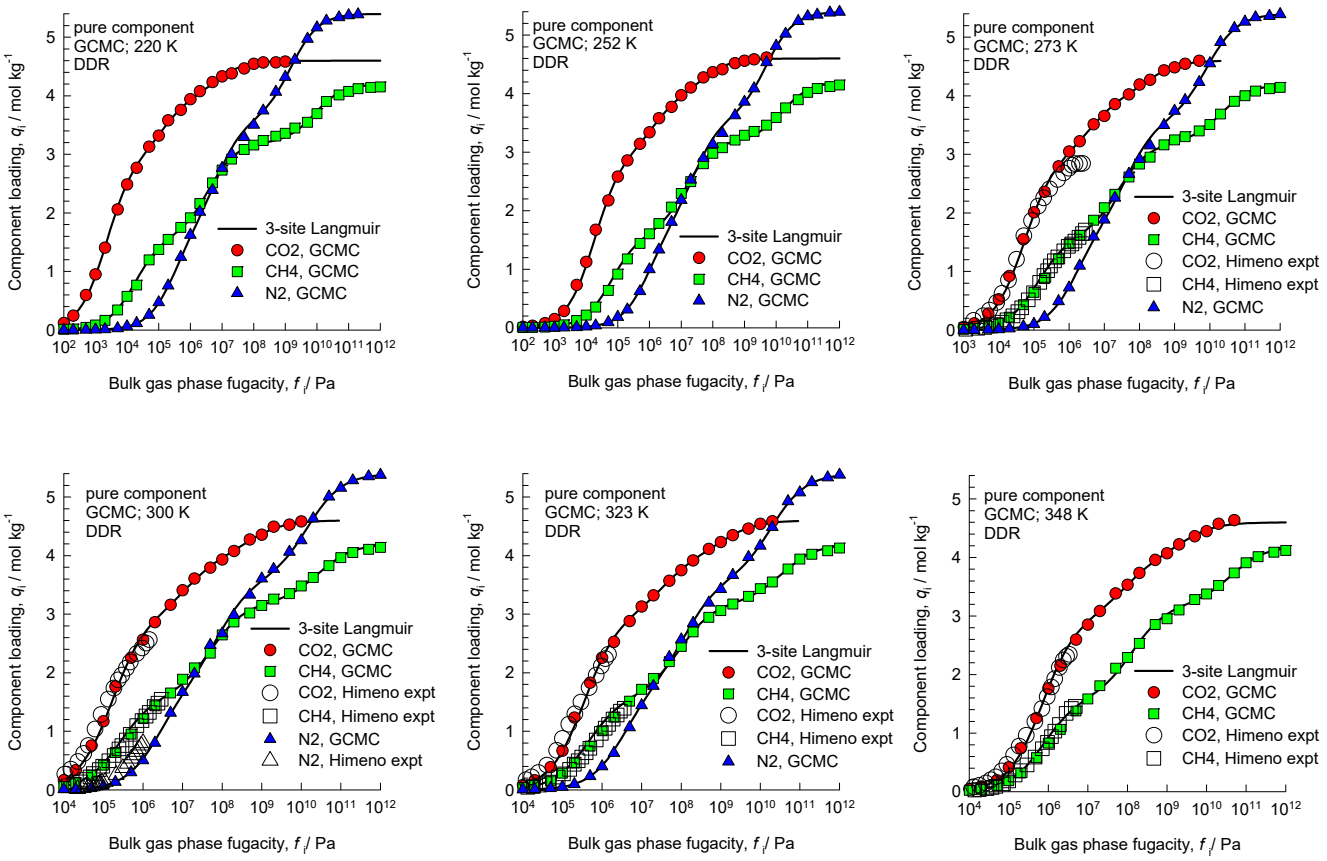

Figure S16. Comparison of CBMC simulated isotherms[19] for CO_2, CH_4 and N_2 with experimental data of Himeno et al.[34-36] Also shown by the continuous solid lines are the 3-site Langmuir fits of the isotherms using the parameters specified in Table S2.

DDR membrane permeation

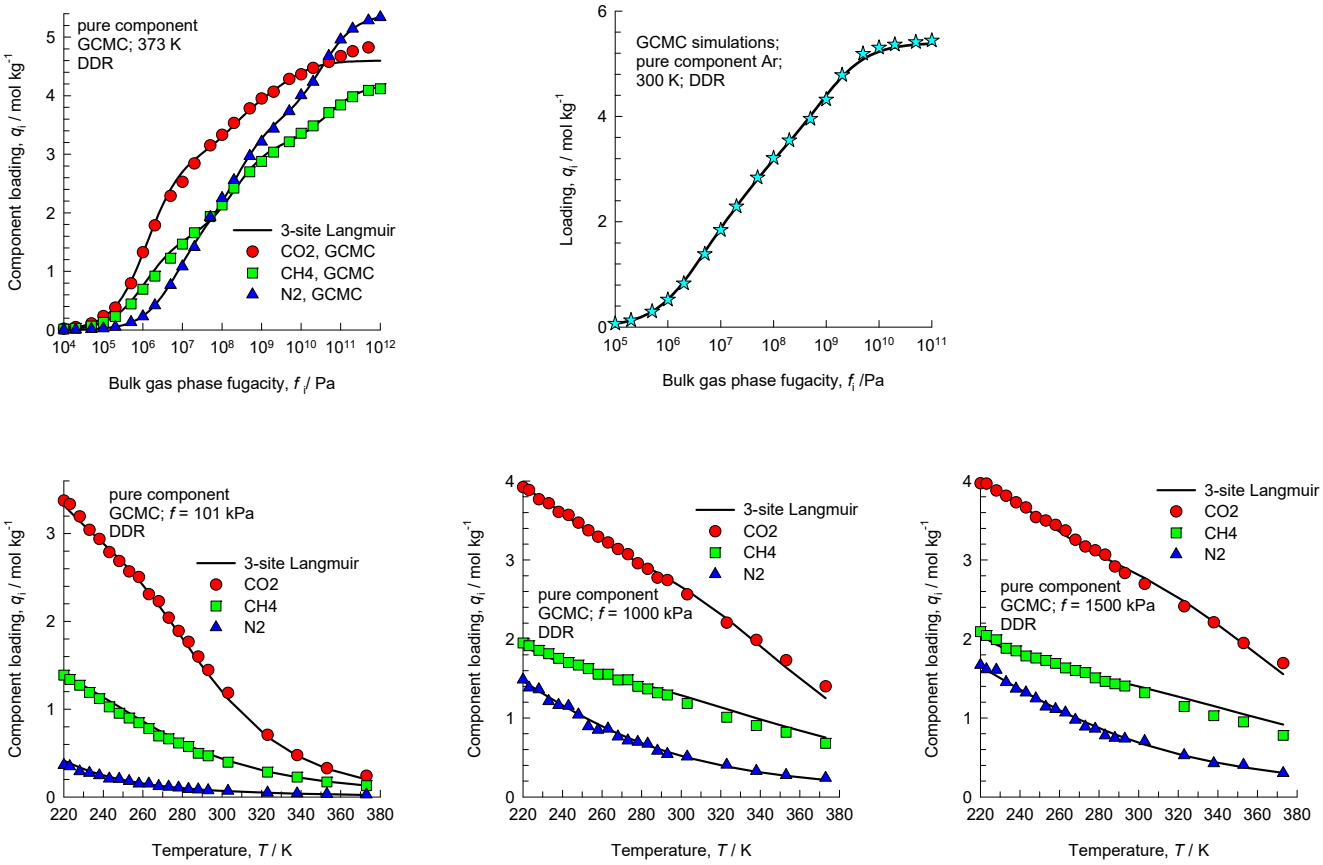

Figure S17. Comparison of CBMC simulated isotherms[19] for CO_2, CH_4, N_2 and Ar with 3-site Langmuir fits of the isotherms using the parameters specified in Table S2.

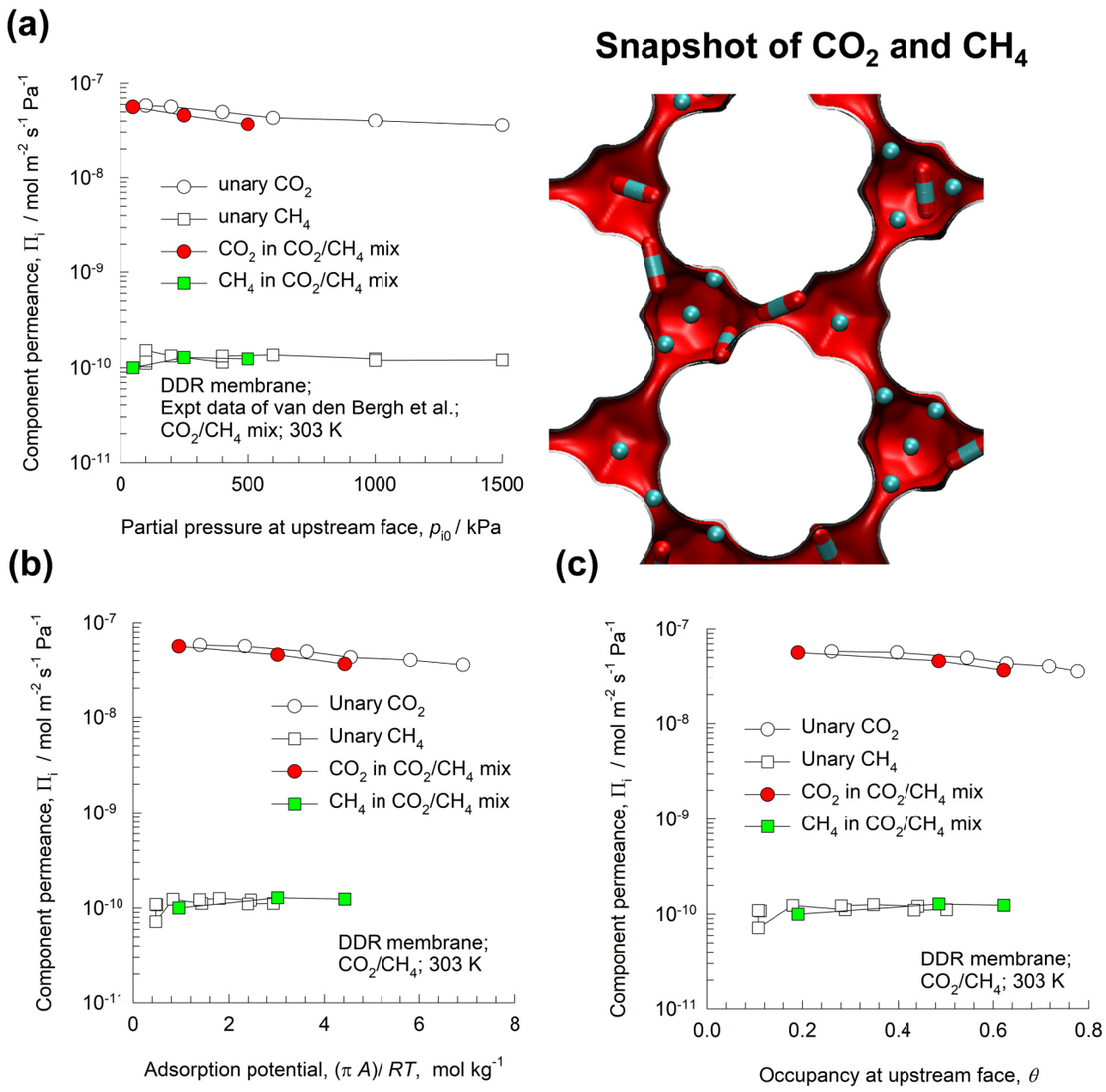

Figure S18. Experimental data of Van den Bergh et al.[37, 38] for component permeances for 50/50 CO_2/CH_4 binary mixture permeation across DDR membrane at 303 K, compared to unary permeation data. The data are plotted as function of (a) upstream partial pressures, p_{i0}, (b) adsorption potential $\pi A/RT$ and (c) occupancy θ at the upstream face of the membrane.

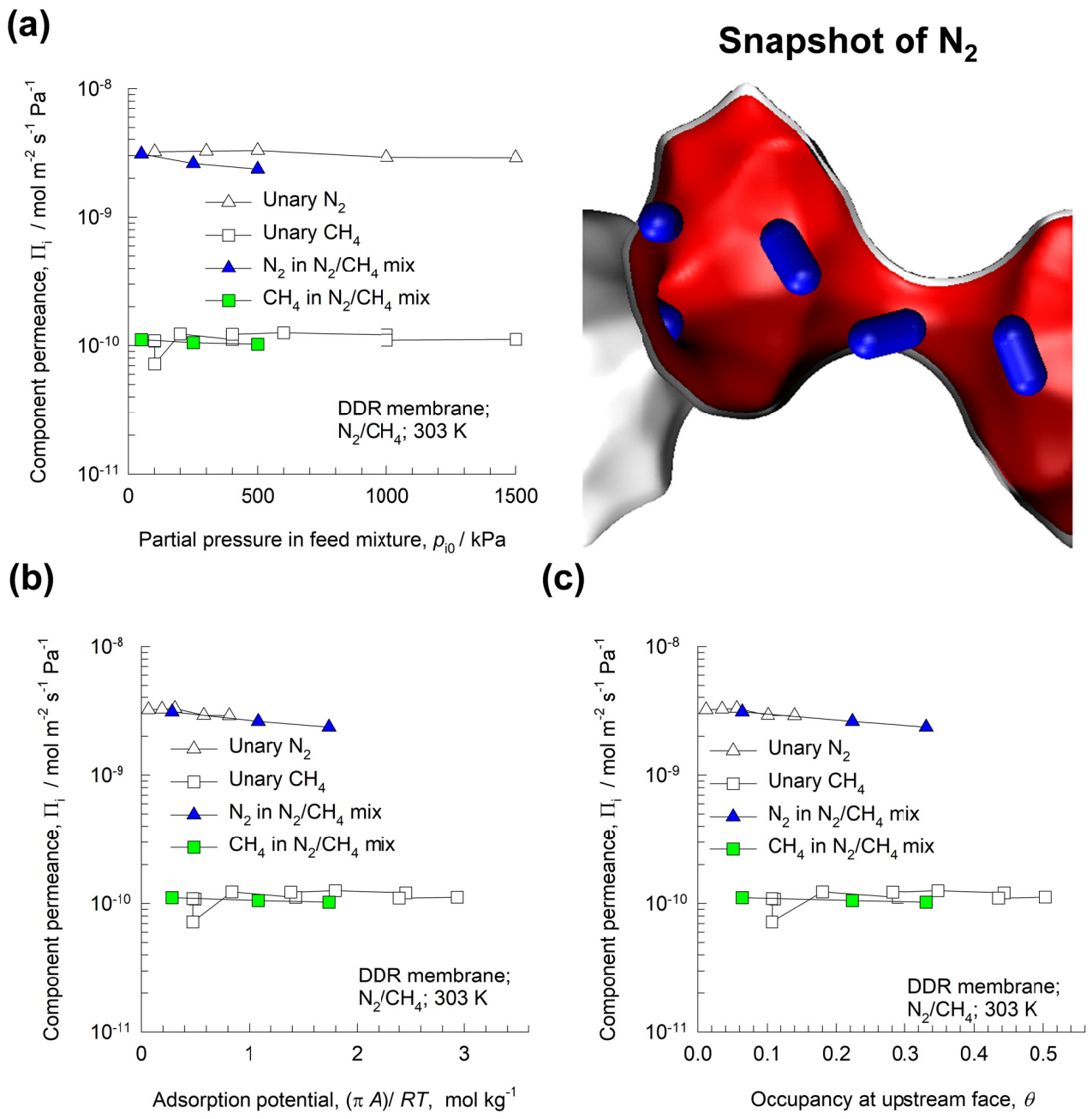

Figure S19. Experimental data of Van den Bergh et al.[37, 38] for component permeances for 50/50 N_2/CH_4 binary mixture permeation across DDR membrane at 303 K, compared to unary permeation data. The data are plotted as function of (a) upstream partial pressures, p_{i0}, (b) adsorption potential $\pi A/RT$ and (c) occupancy θ at the upstream face of the membrane.

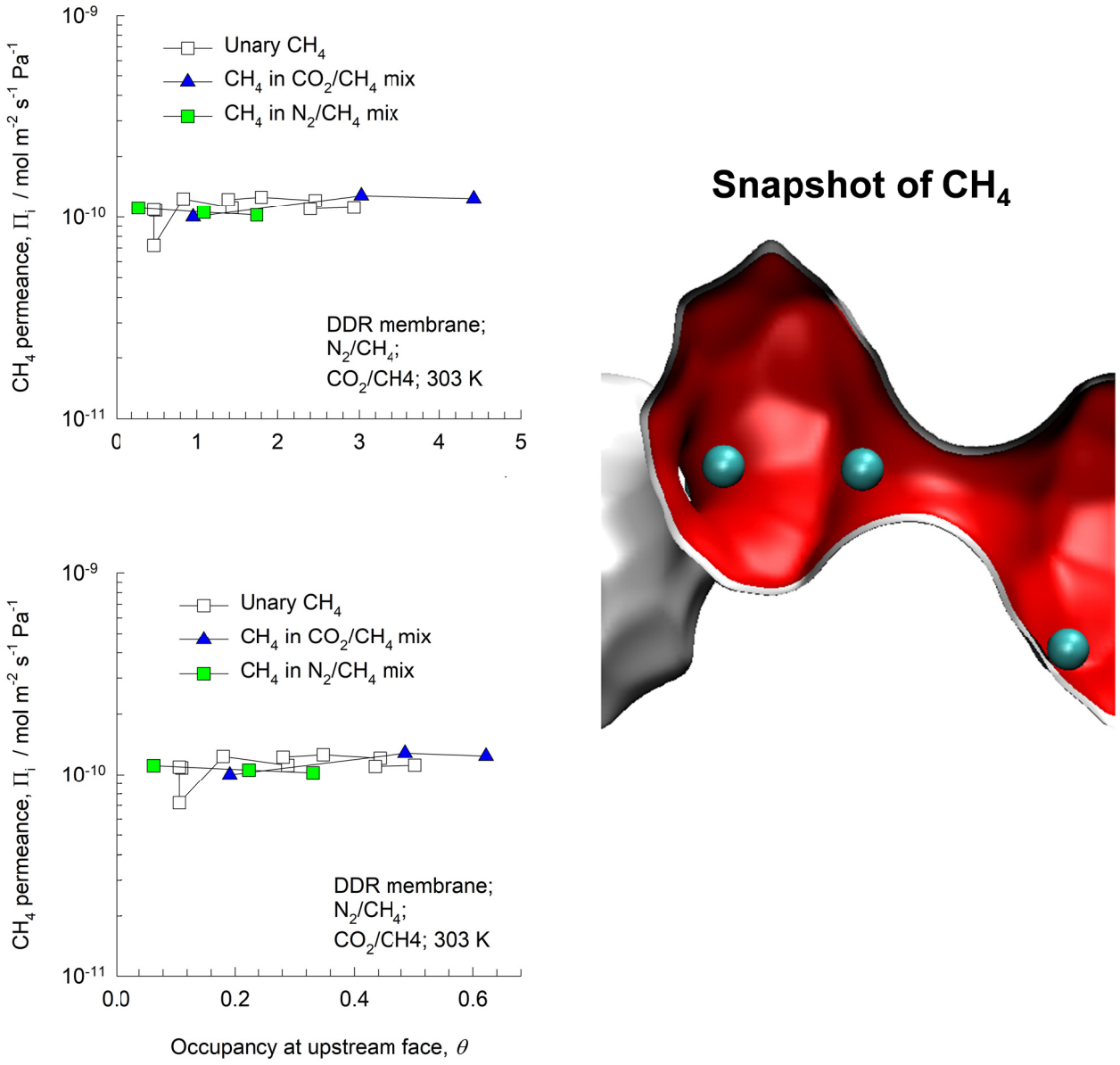

Figure S20. Comparison of CH_4 component permeances for 50/50 CO_2/CH_4 and 50/50 N_2/CH_4 binary mixture permeation across DDR membrane at 303 K, compared to unary permeance. The data are plotted as function of the adsorption potential $\pi A/RT$ and occupancy θ at the upstream face of the membrane.

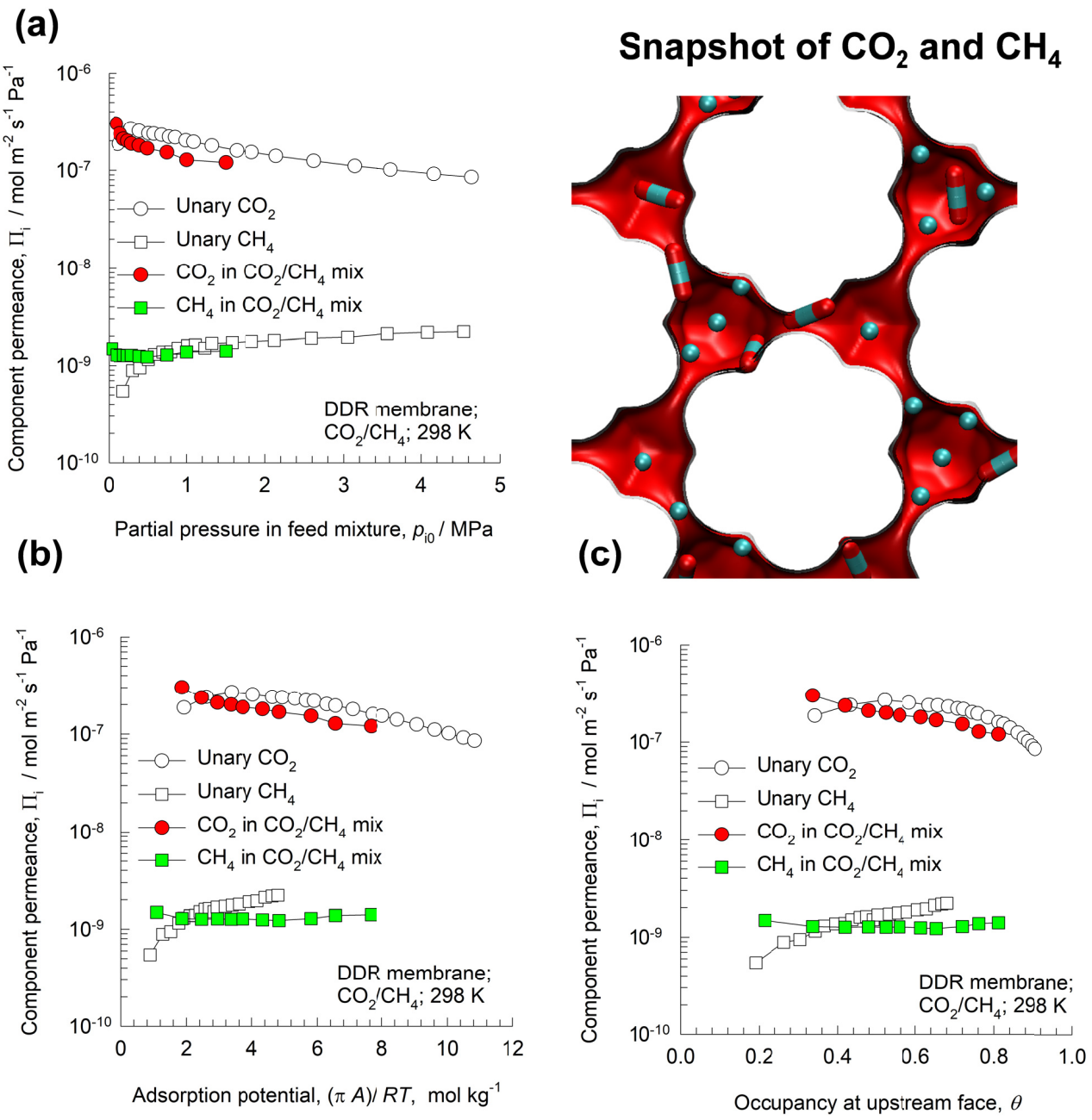

Figure S21. Experimental data of Himeno et al.,[35] scanned from Figures 6, 10, and 11 of their paper, for component permeances for 50/50 CO_2/CH_4 binary mixture permeation across DDR membrane at 298 K, compared to unary permeation data. The data are plotted as function of (a) upstream partial pressures, p_{i0}, (b) adsorption potential $\pi A/RT$ and (c) occupancy θ at the upstream face of the membrane.

7 ZIF-8 membrane permeation

ZIF-8 has a cage-window SOD (sodalite) topology (see pore landscapes in Figure S22, and Figure S23). The crystallographic size of the windows of ZIF-8 are 3.3 Å, but the windows are flexible. The separation of C_2H_4/C_2H_6, and C_3H_6/C_3H_8 mixtures using ZIF-8 membranes is primarily based on differences in the diffusivities of the alkenes and alkanes; such differences arise due to subtle differences in bond lengths and bond angles.[39] The ratio of the diffusivity of C_3H_6 propene to that of C_3H_8 in ZIF-8 has a value of 125 based on the uptake data of Li et al.[40] A further confirmation of the subtle influence of bond lengths and bond angles on diffusivities of alkenes and alkanes is provided by Ruthven and Reyes[29] who report diffusion selectivity values for C_3H_6/C_3H_8 mixtures in excess of 1000 for CHA and DDR zeolites.

The adsorption selectivities for C_2H_4/C_2H_6, and C_3H_6/C_3H_8 mixtures using ZIF-8 favor the saturated alkane; this implies that adsorption and diffusion do not proceed hand in hand. The diffusion selectivities over-ride the adsorption selectivties, yielding permeation selectivities in favor of the unsaturated alkene. From the unary isotherm data in Table S4, the ratio of single-site Langmuir parameters b_2/b_1 for C_3H_6/C_3H_8 is 1.08 at 308 K.

Figure S24 presents the Experimental data of Bux et al.[41] for component permeances for 50/50 $C_2H_4/C2_3H_6$ binary mixture permeation across ZIF-8 membrane at 298 K, compared to unary permeances. The data are plotted as function (a) upstream partial pressures, p_{i0}, (b) adsorption potential $\pi A/RT$ and (c) occupancy θ at the upstream face of the membrane.

Figure S25 presents the experimental data Liu et al.[42] of permeances for 50/50 C_3H_6/C_3H_8 mixtures in ZIF-8 membrane at 308 K, compared to unary permeances. The data are plotted as function of (a) upstream partial pressures, p_{i0}, (b) adsorption potential $\pi A/RT$ and (c) occupancy θ at the upstream face of the membrane.

7.1 List of Tables for ZIF-8 membrane permeation

Table S3. 1-site Langmuir-Freundlich parameters for ethene and ethane in ZIF-8.[43] The *T*-dependent parameters are obtained by fitting the combined sets of pure component isotherm data of Böhme et al.[44] determined for a variety of temperatures in the range 273 K to 408 K.

$$q = q_{sat}\frac{bp^{\nu}}{1+bp^{\nu}} \quad b_A = b_0 \exp\left(\frac{E}{RT}\right)$$

	q_{sat} mol kg^{-1}	b_0 Pa$^{-\nu}$	E kJ mol^{-1}	ν dimensionless
ethene	12	9.37×10^{-11}	21.5	1.08
ethane	12	8.55×10^{-11}	23.2	1.08

ZIF-8 membrane permeation

Table S4. 1-site Langmuir parameters for propene and propane in ZIF-8.[43] The *T*-dependent parameters are obtained by fitting the combined sets of pure component isotherm data of Li et al.[40] and Böhme et al.[44] determined for a variety of temperatures in the range 273 K to 408 K.

$$q = q_{sat}\frac{bp}{1+bp};\ b_A = b_0 \exp\left(\frac{E}{RT}\right)$$

	q_{sat} mol kg^{-1}	b_0 Pa^{-1}	E kJ mol^{-1}
propene	5.2	4.57×10^{-11}	33.9
propane	5.2	1.39×10^{-10}	31.3

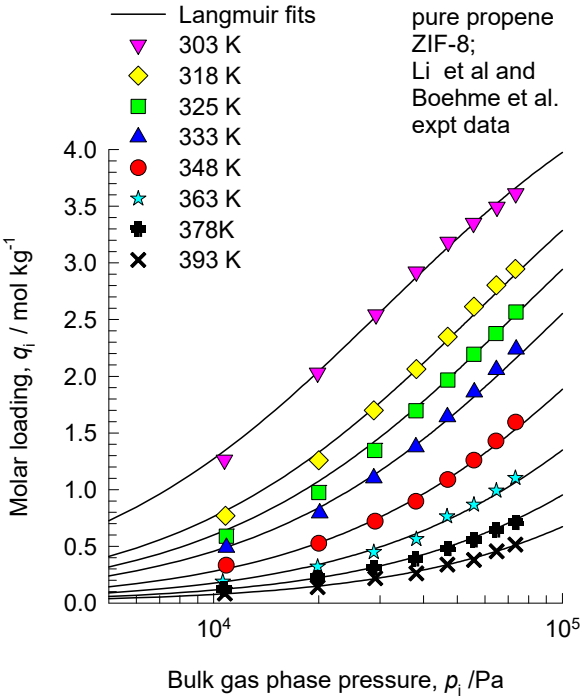

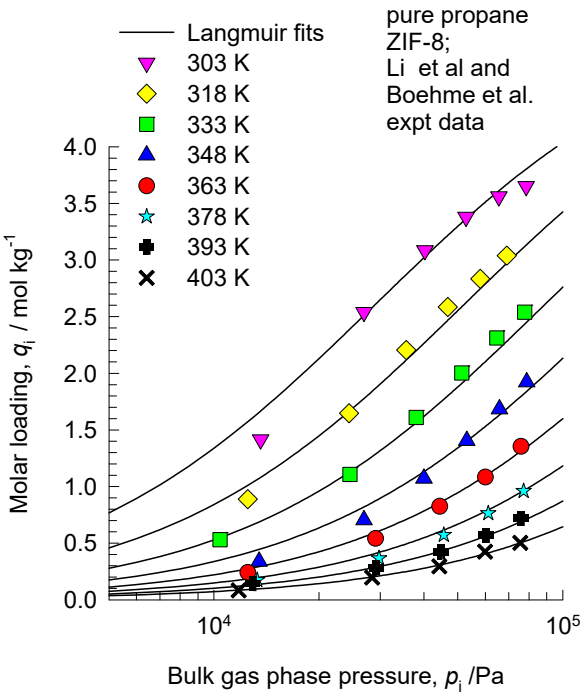

7.2 List of Figures for ZIF-8 membrane permeation

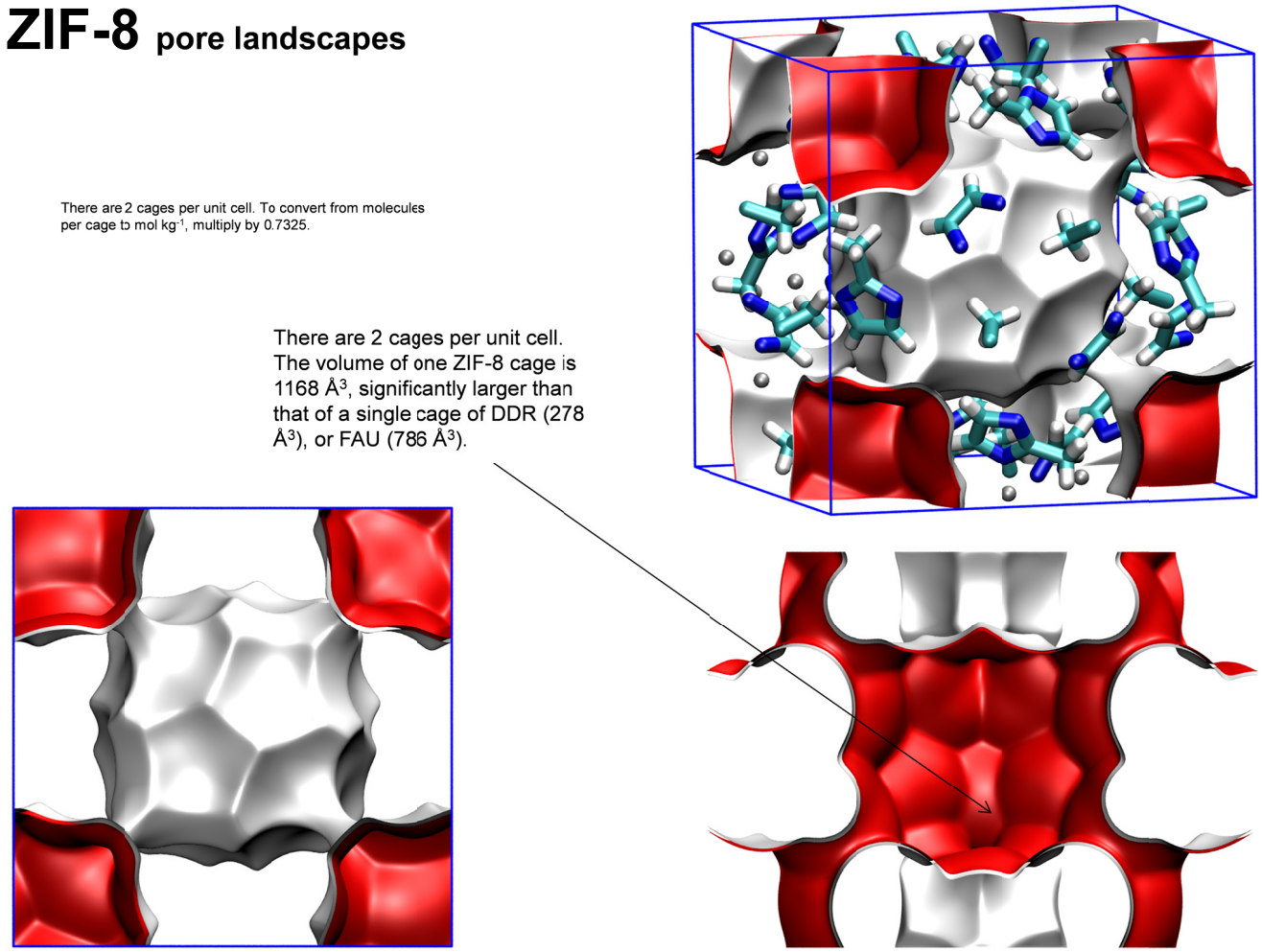

Figure S22. Pore landscape and structural details of ZIF-8.

ZIF-8 dimensions

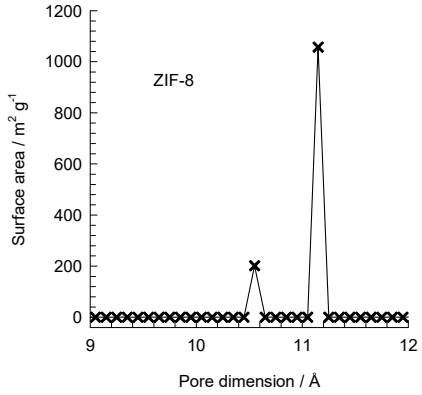

This plot of surface area versus pore dimension is determined using a combination of the DeLaunay triangulation method for pore dimension determination, and the procedure of Düren for determination of the surface area.

	ZIF-8
a /Å	16.991
b /Å	16.991
c /Å	16.991
Cell volume / Å^3	4905.201
conversion factor for [molec/uc] to [mol per kg Framework]	0.3663
conversion factor for [molec/uc] to [kmol/m^3]	0.7106
ρ [kg/m3]	924.253
MW unit cell [g/mol(framework)]	2730.182
ϕ, fractional pore volume	0.476
open space / Å^3/uc	2337.0
Pore volume / cm^3/g	0.515
Surface area /m^2/g	1164.7
DeLaunay diameter /Å	3.26

Figure S23. Pore landscape and structural details of ZIF-8.

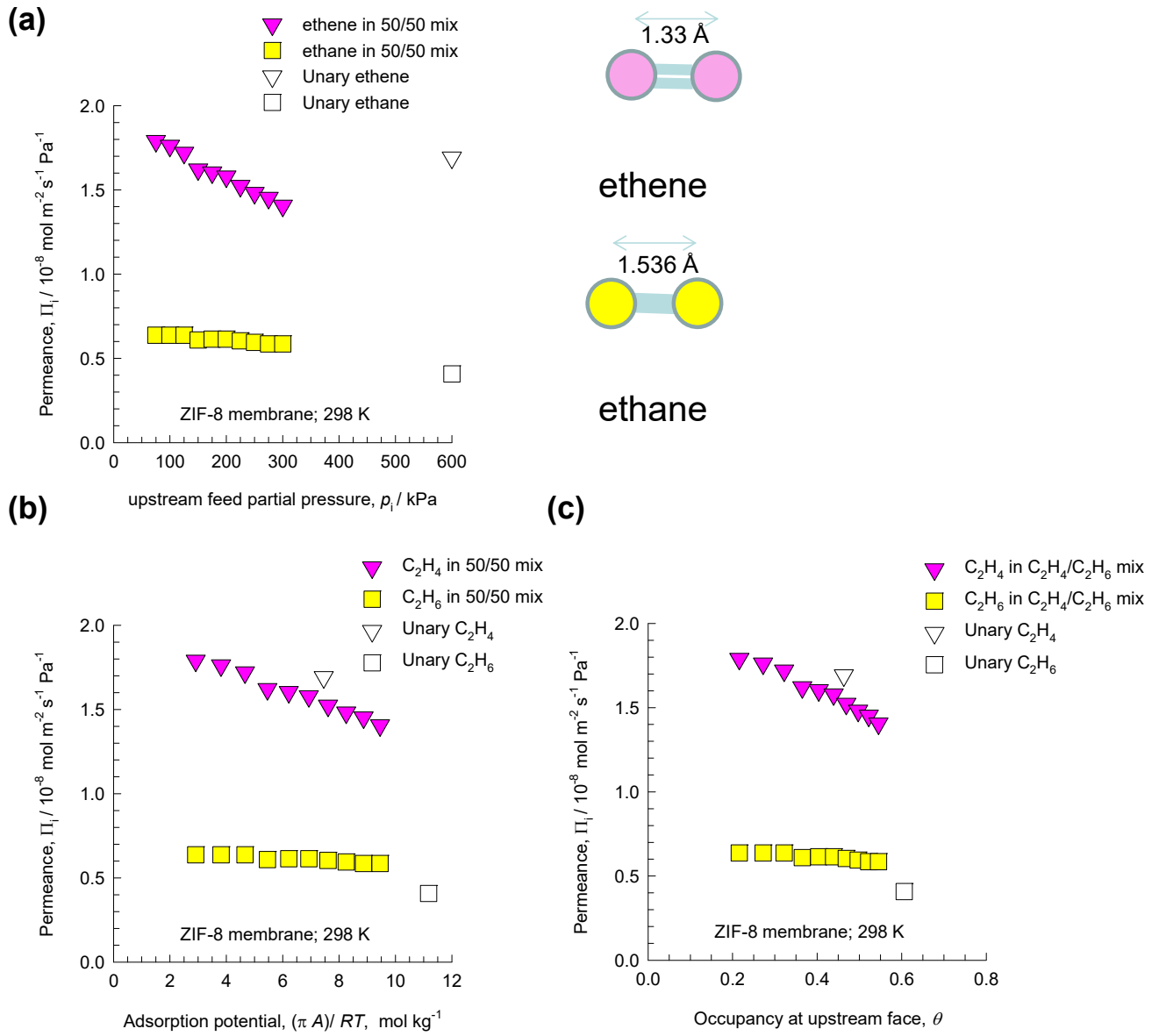

Figure S24. Experimental data of Bux et al.[41] for component permeances for 50/50 $C_2H_4/C2_3H_6$ binary mixture permeation across ZIF-8 membrane at 308 K, compared to unary permeation data. The data are plotted as function of (a) upstream partial pressures, p_{i0}, (b) adsorption potential $\pi A/RT$ and (c) occupancy θ at the upstream face of the membrane. The isotherm data are provided in Table S3.

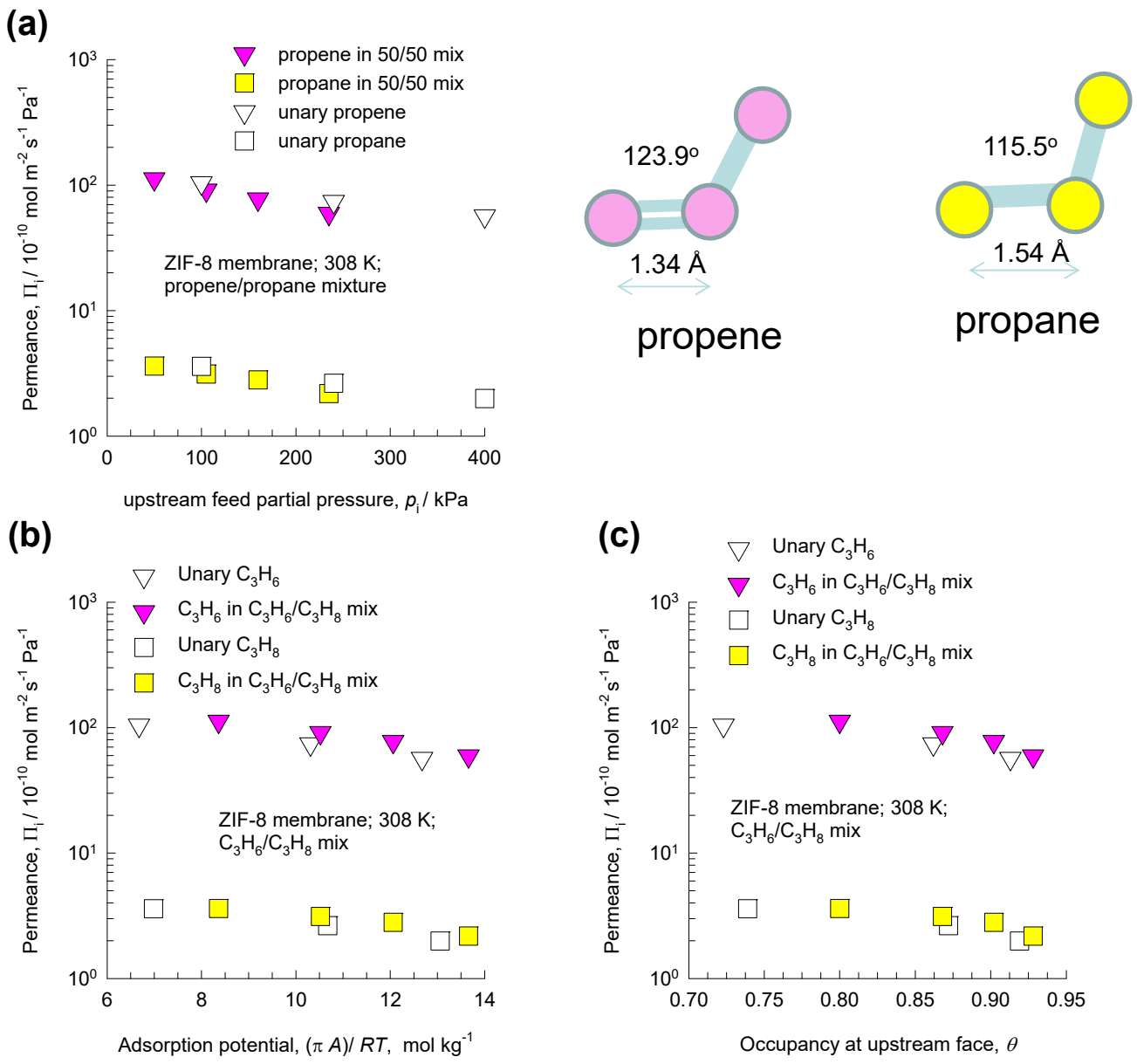

Figure S25. Experimental data of Liu et al.[42] for component permeances for 50/50 C_3H_6/C_3H_8 binary mixture permeation across ZIF-8 membrane at 308 K, compared to unary permeation data. The data are plotted as function of (a) upstream partial pressures, p_{i0}, (b) adsorption potential $\pi A/RT$ and (c) occupancy θ at the upstream face of the membrane. The isotherm data are provided in Table S4.

8 MFI zeolite membrane permeation

8.1 MFI structural details

MFI zeolite (also called silicalite-1) has a topology consisting of a set of intersecting straight channels, and zig-zag (or sinusoidal) channels of approximately 5.5 Å size. The pore landscapes and structural details are provided in Figure S26, and Figure S27.

8.2 CO_2/H_2 permeation at 296 K, and 273 K

For analysis of the CO_2/H_2 permeation data of Sandström et al.,[45] measured at 296 K the required isotherm parameters are specified in Table S5. The isotherms are fitted with the single-site Langmuir model with equal saturation capacities for either species, equation (S14). The analysis of the experimental permeation data is summarized in Figure S28.

The experimental data are amenable to modeling using the Maxwell-Stefan equations:

$$\begin{aligned} -\rho\frac{q_1}{RT}\frac{d\mu_1}{dz} &= \frac{x_2N_1 - x_1N_2}{Đ_{12}} + \frac{N_1}{Đ_1};\\ -\rho\frac{q_2}{RT}\frac{d\mu_2}{dz} &= \frac{x_1N_2 - x_2N_1}{Đ_{12}} + \frac{N_2}{Đ_2} \end{aligned} \tag{S46}$$

where ρ represents the framework density of the microporous crystalline material. For steady state permeation across a microporous membrane of thickness δ (see schematic in Figure S29), the M-S equations can be solved using the simple linearization technique described in earlier work to yield

$$\begin{aligned} \begin{pmatrix} N_1 \\ N_2 \end{pmatrix} &= \frac{\rho}{\delta}[\Lambda][\Gamma]\begin{pmatrix} q_{10} - q_{1\delta} \\ q_{20} - q_{2\delta} \end{pmatrix};\\ [\Lambda] &= \frac{1}{1 + \frac{x_1Đ_2}{Đ_{12}} + \frac{x_2Đ_1}{Đ_{12}}}\begin{bmatrix} Đ_1\left(1 + \frac{x_1Đ_2}{Đ_{12}}\right) & \frac{x_1Đ_1Đ_2}{Đ_{12}} \\ \frac{x_2Đ_1Đ_2}{Đ_{12}} & Đ_2\left(1 + \frac{x_2Đ_1}{Đ_{12}}\right) \end{bmatrix}\\ [\Gamma] &= \frac{1}{1-\theta_1-\theta_2}\begin{bmatrix} 1-\theta_2 & \theta_1 \\ \theta_2 & 1-\theta_1 \end{bmatrix} \end{aligned} \tag{S47}$$

A simple approach is to assume that the two-dimensional square matrices $[\Lambda]$ and $[\Gamma]$ are independent of loadings in the membrane, and evaluated at conditions corresponding to the upstream face of the membrane that is in equilibrium with the feed mixture in the upstream compartment. The component loadings q_{10}, q_{20}, adsorbed phase mole fractions, x_1, x_2, and the fractional occupancies θ_1, θ_2, can be evaluated using the mixed-gas Langmuir model Equation (S24). The model calculations are shown by the continuous solid lines in Figure S30. The zero-loading M-S diffusivities are fitted from unary permeance data: $\rho Đ_1(0)/\delta = 3.2$, and $\rho Đ_2(0)/\delta = 100$ kg m^{-2} s^{-1}. The degree of correlations is taken to increase linearly with occupancy θ: $Đ_2/Đ_{12} = b\theta = b(\theta_1 + \theta_2)$. The H_2 permeance is significantly influenced by correlation effects, as is evidenced in Figure S30 for calculations taking $Đ_2/Đ_{12} = 1.0\theta$, 3.0θ, and 10.0θ; the choice $Đ_2/Đ_{12} = 10.0\theta$ affords the best match with experimental data of Sandström et al..[45]

For analysis of the experimental CO_2/H_2 permeation data of Sjöberg et al.,[46] measured at 273 K the required isotherm parameters are also specified in Table S5. The analysis of the permeation data is summarized in Figure S31. The continuous solid lines in Figure S31 are the M-S model calculations using precisely the same model parameters as used in the analysis of the experimental data of Sandström et al.:[45] $\rho Đ_1(0)/\delta = 3.2$, $\rho Đ_2(0)/\delta = 100$ kg m^{-2} s^{-1}, and $Đ_2/Đ_{12} = 10.0\theta$. The only essential difference in the calculations presented in Figure S30 and Figure S31 are that use of two different single-site Langmuir parameters for the 296 K, and 273 K, respectively.

8.3 CH_4/C_2H_6, and CH_4/C_3H_8 permeation at 303 K

For analysis of the CH_4/C_2H_6, and CH_4/C_3H_8 permeation data at 303 K of van de Graaf et al.[47] the required isotherm parameters are specified in Table S6. The analysis of the permeation data are summarized in Figure S32, and Figure S33.

8.4 CH_4/n-C_4H_{10} permeation at various temperatures

For analysis of the experimental data of Vroon et al.[48] for CH_4/n-C_4H_{10} permeation the required unary isotherm fit parameters are provided in Table S7. The analysis of the permeation data is summarized in Figure S34.

8.5 nC6/22DMB permeation at 398 K

For analysis of the experimental data of Gump et al.[49] for nC6/22DMBpermeation data at 398 K, the required unary isotherm fit parameters are provided in Table S8. The unary isotherm fits are based on CBMC simulation data presented in Figure S35. The analysis of the permeation data is summarized in Figure S36.

8.6 List of Tables for MFI zeolite membrane permeation

Table S5. Langmuir parameter fits for CO_2 and H_2 in MFI (silicalite-1) zeolite. The CO_2 isotherm fits are based on CBMC simulation data at three different temperatures, 200 K, 253 K, and 300 K. The H_2 fits are based on CBMC simulation data at 300 K, combined with experimental data of Golden and Sircar[50] at 305.15 K, and 353.25 K. The *T*-dependent isotherm fits from the sets of data were interpolated, or extrapolated, to 273 K and 296 K. The single-site Langmuir parameters at these two temperatures are provided below.

T = 273 K:

$q = \frac{q_{sat} bp}{1 + bp}$	q_{sat} mol kg^{-1}	b Pa^{-1}
CO_2	3.7	1.447×10^{-5}
H_2	3.7	7.70×10^{-8}

T = 296 K:

$q = \frac{q_{sat} bp}{1 + bp}$	q_{sat} mol kg^{-1}	b Pa^{-1}
CO_2	3.7	5.94×10^{-6}
H_2	3.7	5.50×10^{-8}

MFI zeolite membrane permeation

Table S6. Dual-site Langmuir-Freundlich parameters for CH_4, C_2H_6, and C_3H_8 molecules in MFI at 303 K. The isotherm parameters were obtained by fitting to CBMC simulated isotherms as reported in earlier work.[5] To convert saturation loadings from molecules uc^{-1} to mol kg^{-1}, multiply by 0.173367.

	Site A			Site B		
	$\Theta_{A,sat}$ molecules uc^{-1}	b_A $Pa^{-\nu}$	ν_A dimensionless	$\Theta_{B,sat}$ molecules uc^{-1}	b_B $Pa^{-\nu}$	ν_B dimensionless
CH_4	7	5.00E-09	1	16	3.10E-06	1
C_2H_6	3.3	4.08E-07	1	13	7.74E-05	1
C_3H_8	1.4	3.35E-04	0.67	10.7	6.34E-04	1.06

MFI zeolite membrane permeation

Table S7. Dual-site Langmuir-Freundlich parameters for CH_4, and n-C_4H_{10} molecules in MFI at various temperatures *T*. CBMC simulations of unary isotherms at various temperatures were fitted with

$q = q_{A,sat}\frac{b_A p^{\nu_A}}{1+b_A p^{\nu_A}} + q_{B,sat}\frac{b_B p^{\nu_B}}{1+b_B p^{\nu_B}}$. The *b* parameters for each site are temperature-dependent

$b_A = b_{A0}\exp\left(\frac{E_A}{RT}\right)$; $b_b = b_{B0}\exp\left(\frac{E_B}{RT}\right)$. The parameters are provided in the Table below. To convert saturation loadings from molecules uc^{-1} to mol kg^{-1}, multiply by 0.173367.

	Site A				Site B			
	$q_{A,sat}$ molecule uc^{-1}	b_{A0} $Pa^{-\nu_A}$	E_A kJ mol^{-1}	ν_A dimensionless	$q_{B,sat}$ molecule uc^{-1}	b_{B0} $Pa^{-\nu_B}$	E_B kJ mol^{-1}	ν_B dimensionless
CH_4	7	9.52E-08	10	0.6	16	5.51E-10	21	1
nC_4H_{10}	2.5	6.6E-09	35	10.64	7.4	3.98E-15	70	1.35

MFI zeolite membrane permeation

Table S8. Dual-site Langmuir-Freundlich parameters for nC6, and 22DMB molecules in MFI at 398 K. The isotherm parameters were obtained by fitting to CBMC simulated isotherms as reported in earlier work.[5] To convert saturation loadings from molecules uc^{-1} to mol kg^{-1}, multiply by 0.173367.

	Site A			Site B		
	$\Theta_{A,sat}$ molecules uc^{-1}	b_A $Pa^{-\nu}$	ν_A dimensionless	$\Theta_{B,sat}$ molecules uc^{-1}	b_B $Pa^{-\nu}$	ν_B dimensionless
nC6	4	4.00E-03	1	3.7	1.104E-04	1
22DMB	4	1.24E-03	1			

8.7 List of Figures for MFI zeolite membrane permeation

MFI pore landscape

	MFI
a /Å	20.022
b /Å	19.899
c /Å	13.383
Cell volume / Å^3	5332.025
conversion factor for [molec/uc] to [mol per kg Framework]	0.1734
conversion factor for [molec/uc] to [kmol/m^3]	1.0477
ρ [kg/m3]	1796.386
MW unit cell [g/mol(framework)]	5768.141
ϕ, fractional pore volume	0.297
open space / Å^3/uc	1584.9
Pore volume / cm^3/g	0.165
Surface area /m^2/g	487.0
DeLaunay diameter /Å	5.16

Structural information from: C. Baerlocher, L.B. McCusker,
Database of Zeolite Structures, International Zeolite Association,
http://www.iza-structure.org/databases/

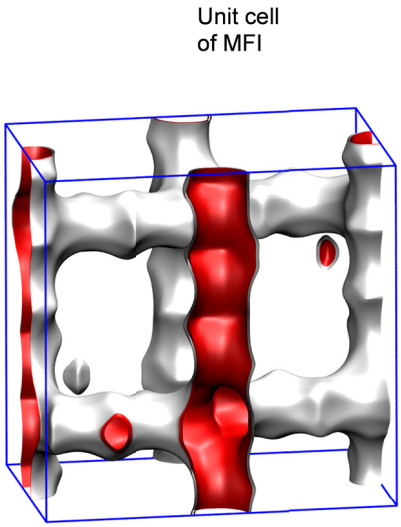

Figure S26. Structural details and pore landscape for MFI zeolite.

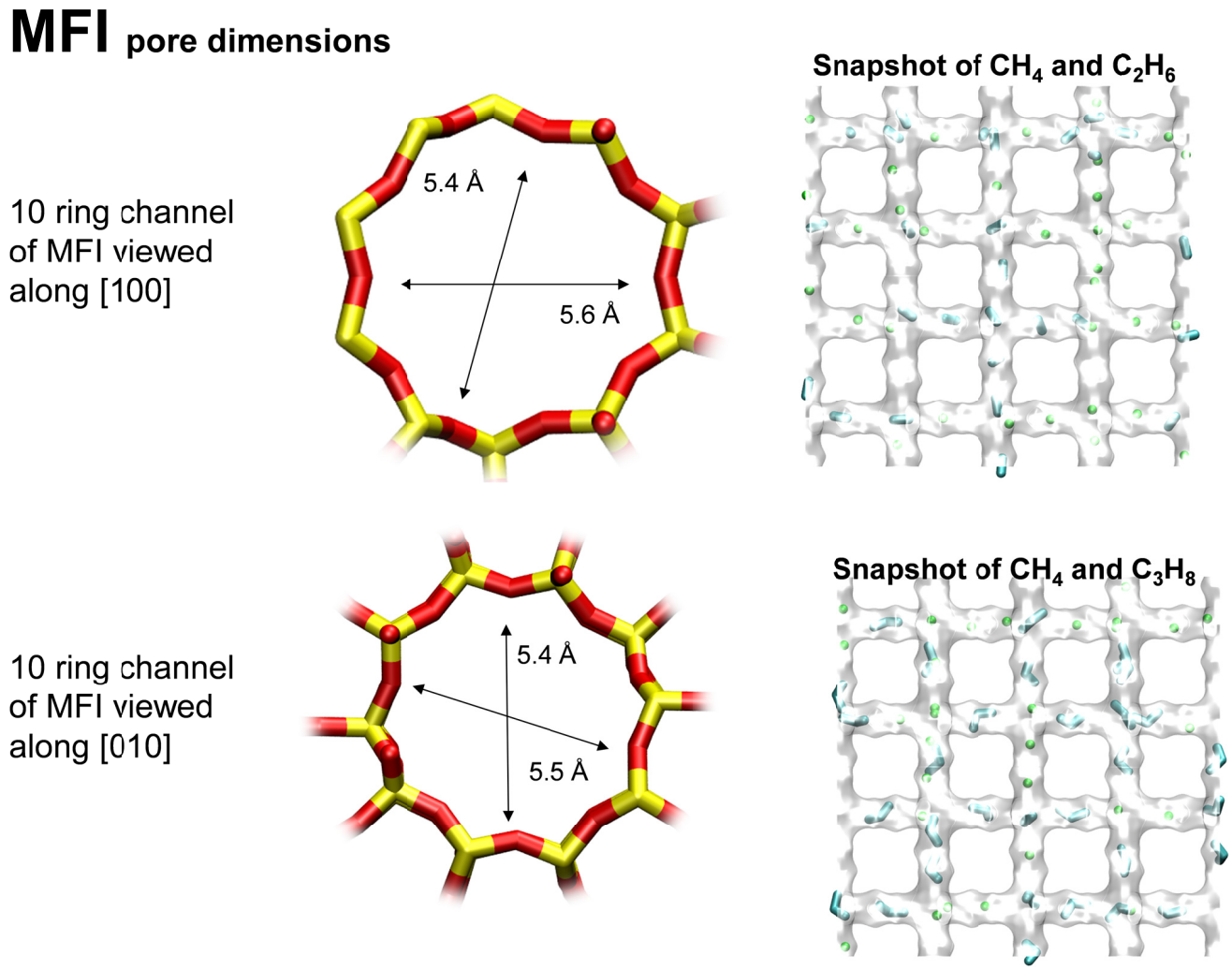

Figure S27. Structural details and pore landscape for MFI zeolite.

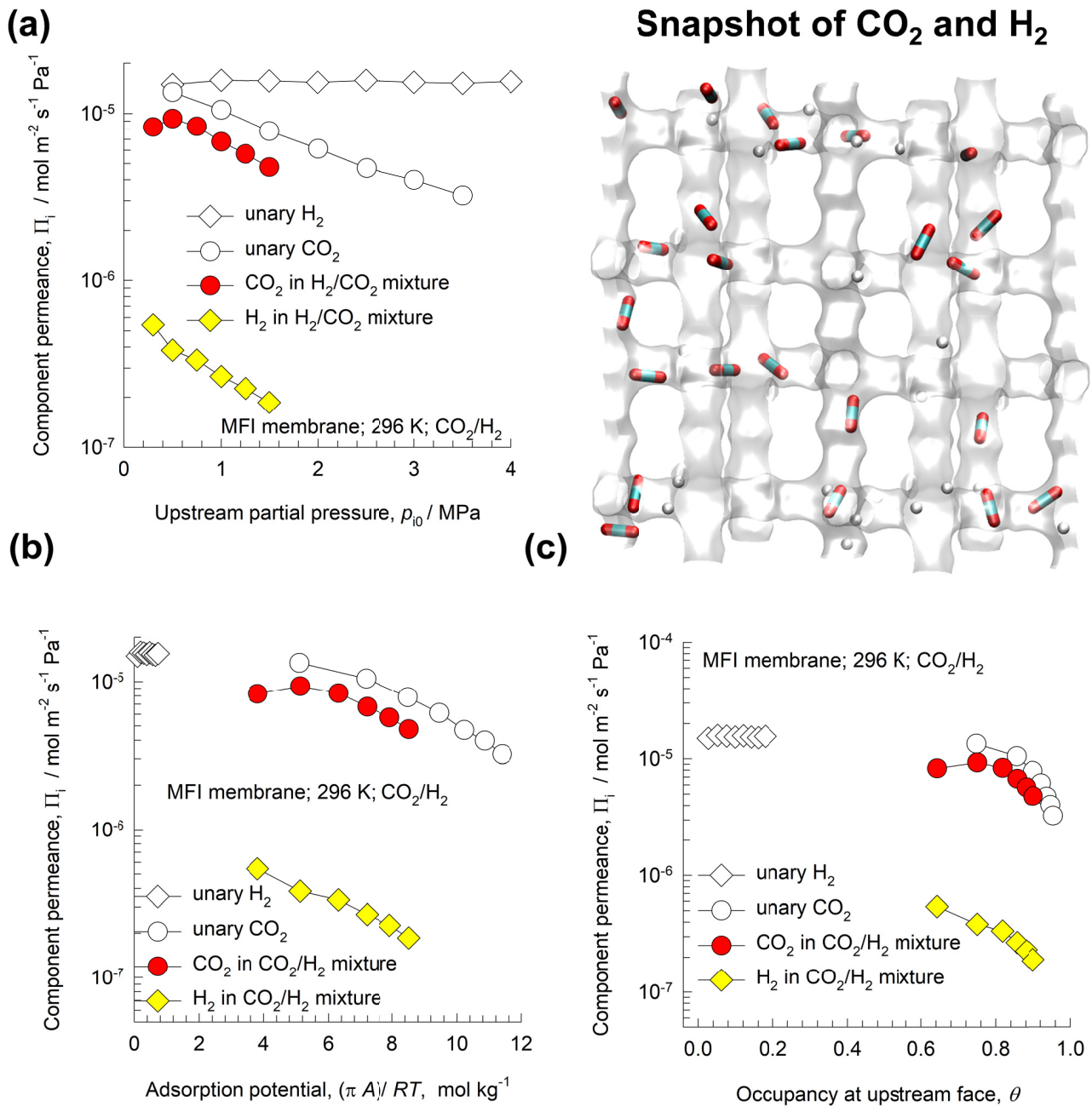

Figure S28. Experimental data of Sandström et al.[45] on component permeances for 50/50 CO_2/H_2 binary mixture permeation across MFI membrane at 296 K, compared to unary permeation data. The data are plotted as function of (a) upstream partial pressures, p_{i0}, (b) adsorption potential $\pi A/RT$ and (c) occupancy θ at the upstream face of the membrane.

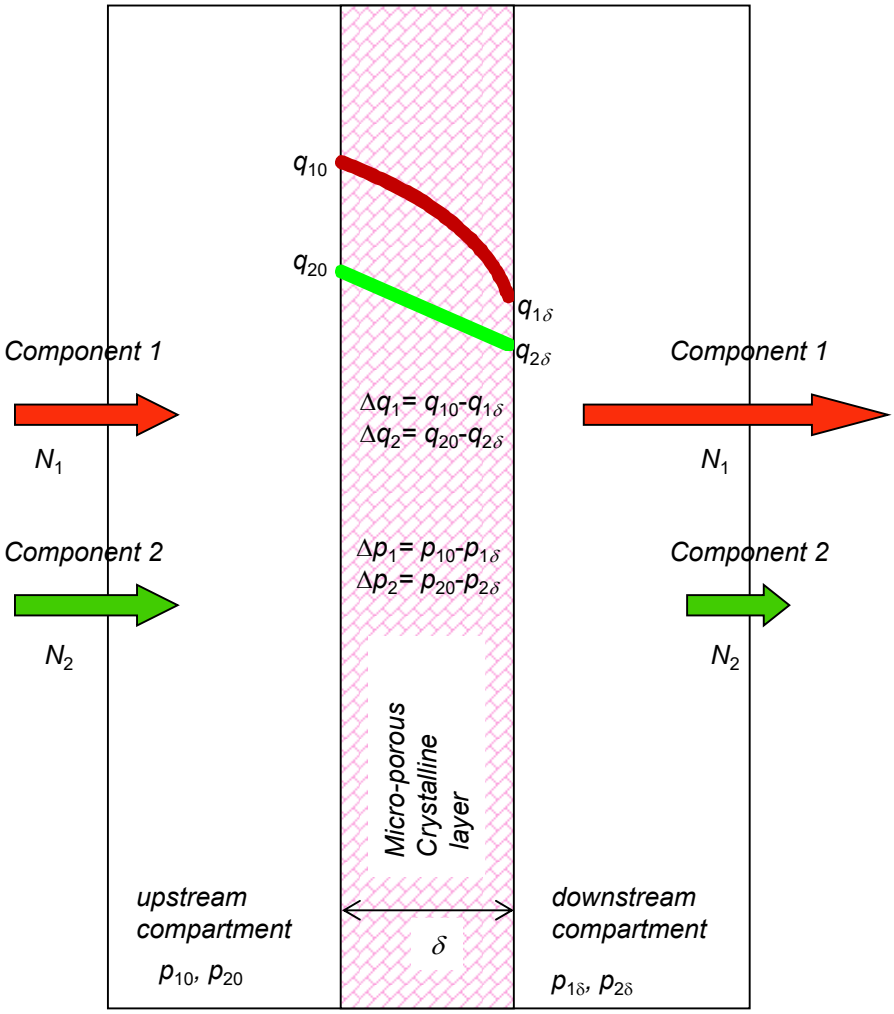

Figure S29. Schematic showing binary mixture permeation across microporous membrane.

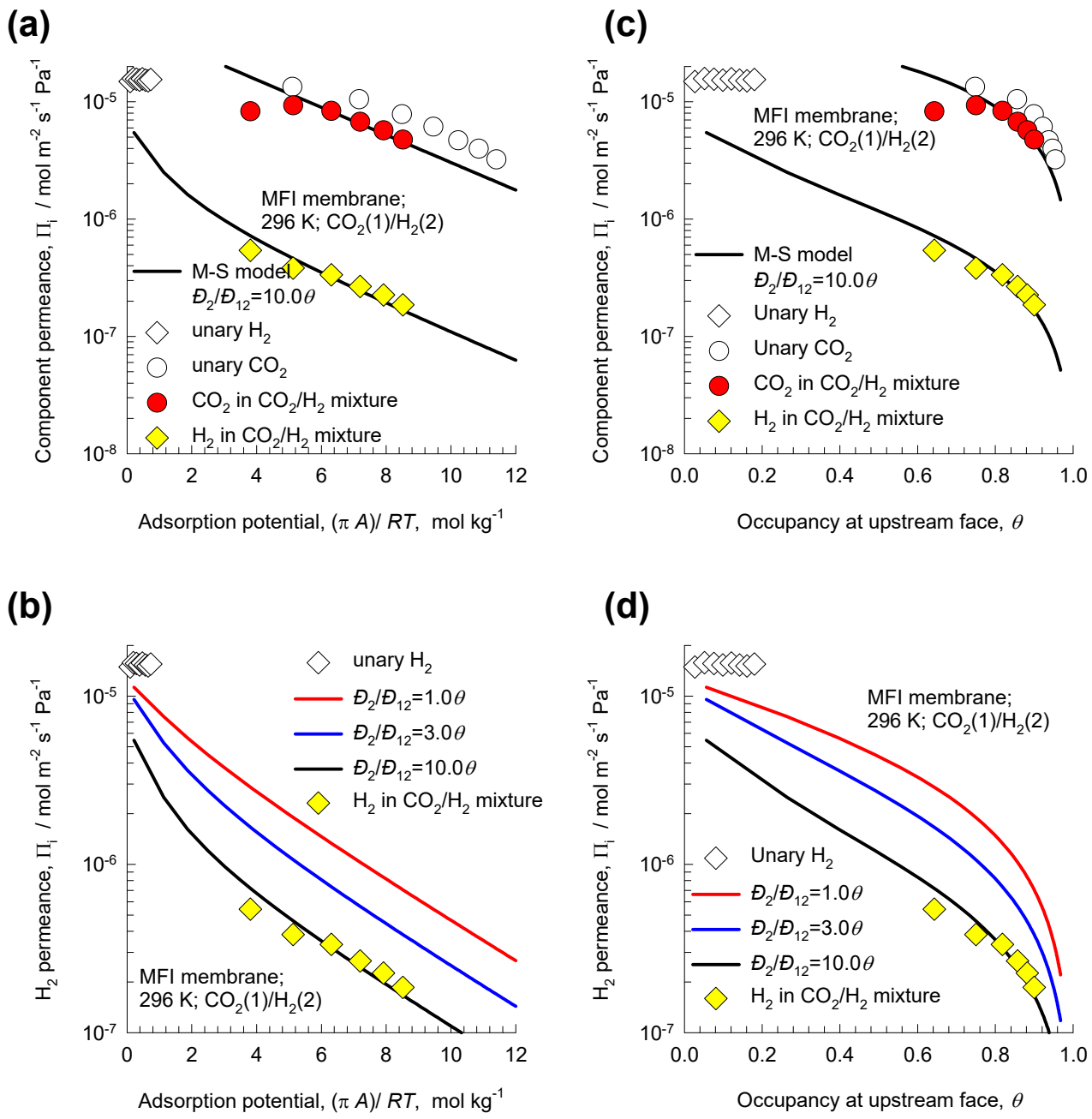

Figure S30. Experimental data of Sandström et al.[45] on component permeances for 50/50 CO_2/H_2 binary mixture permeation across MFI membrane at 296 K, compared with the M-S model calculations for various values of the degrees of correlation. The data are plotted as function of (a, b) adsorption potential $\pi A/RT$ and (c, d) occupancy θ at the upstream face of the membrane.

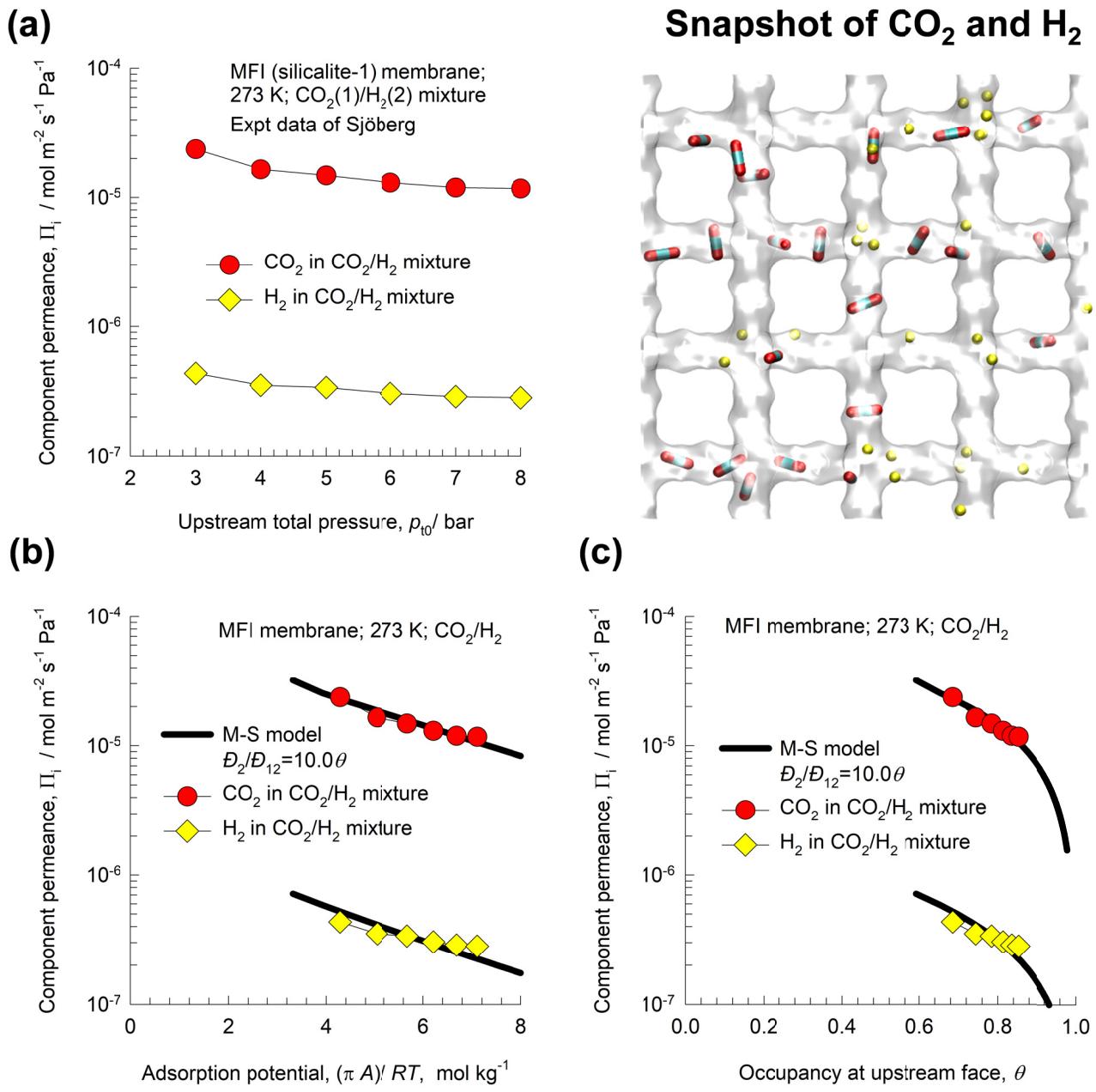

Figure S31. Experimental data of Sjöberg et al.[46] on component permeances for 50/50 CO_2/H_2 binary mixture permeation across MFI membrane at 273 K. The data are plotted as function of (a) upstream partial pressures, p_{i0}, (b) adsorption potential $\pi A/RT$ and (c) occupancy θ at the upstream face of the membrane. The continuous solid lines are the M-S model calculations.

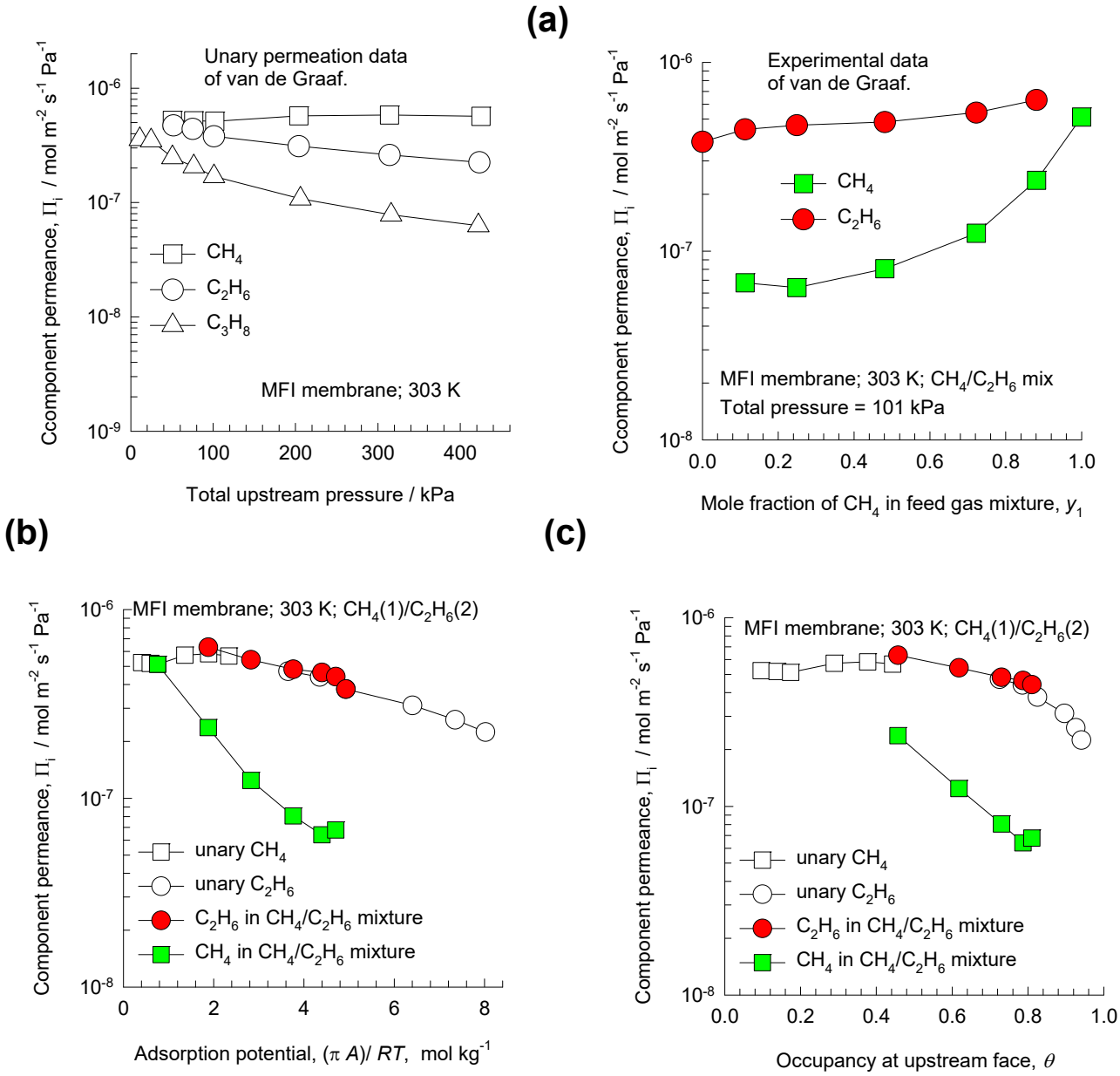

Figure S32. Experimental data of van de Graaf et al.[47] on component permeances for CH_4/C_2H_6 binary mixture permeation across MFI membrane at 303 K, and 101 kPa. The data are plotted as function of (a) upstream feed compositions and (b) adsorption potential $\pi A/RT$ and (c) occupancy θ at the upstream face of the membrane.

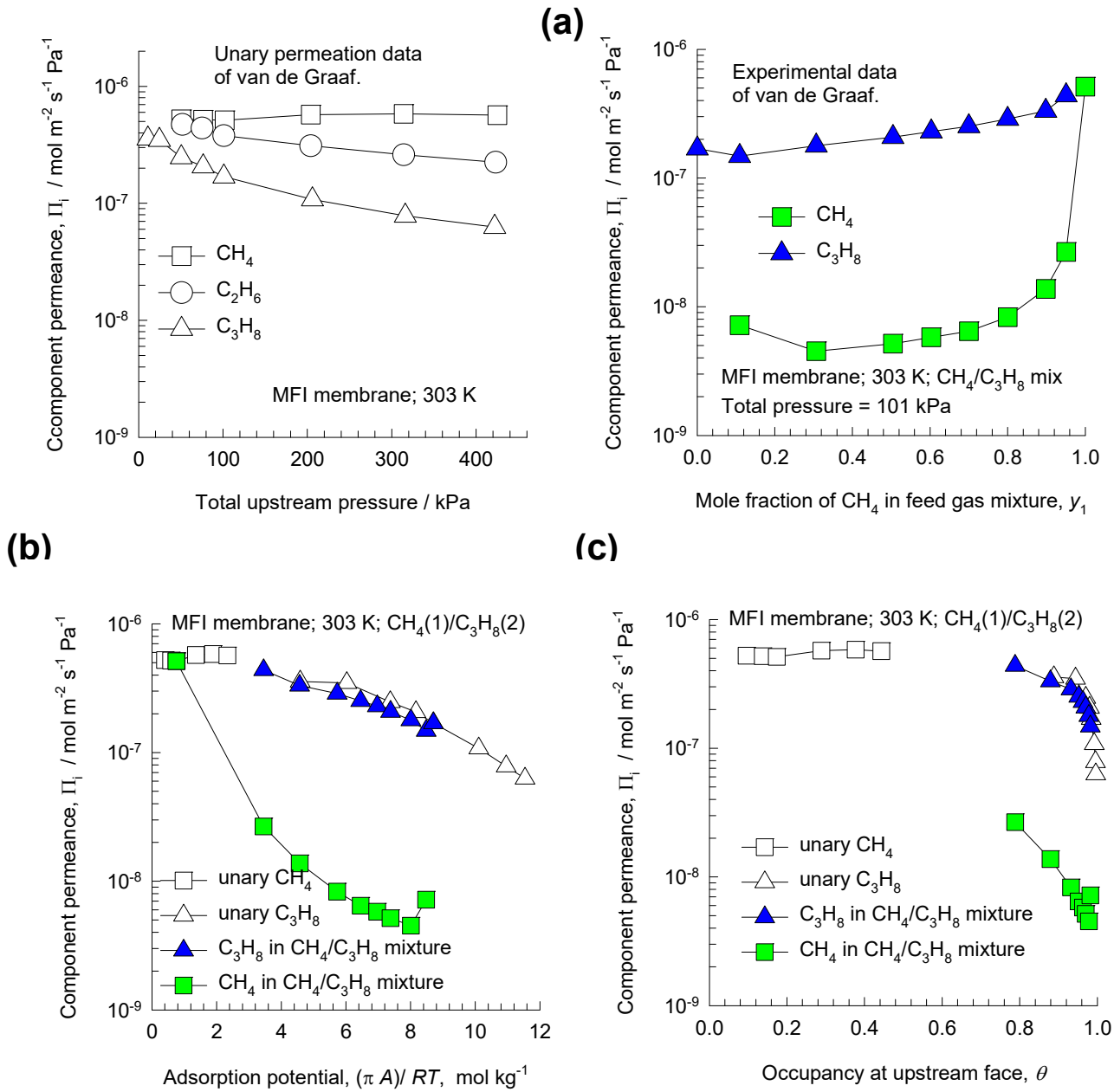

Figure S33. Experimental data of van de Graaf et al.[47] on component permeances for CH_4/C_3H_8 binary mixture permeation across MFI membrane at 303 K, and 101 kPa. The data are plotted as function of (a) upstream feed compositions and (b) adsorption potential $\pi A/RT$ and (c) occupancy θ at the upstream face of the membrane.

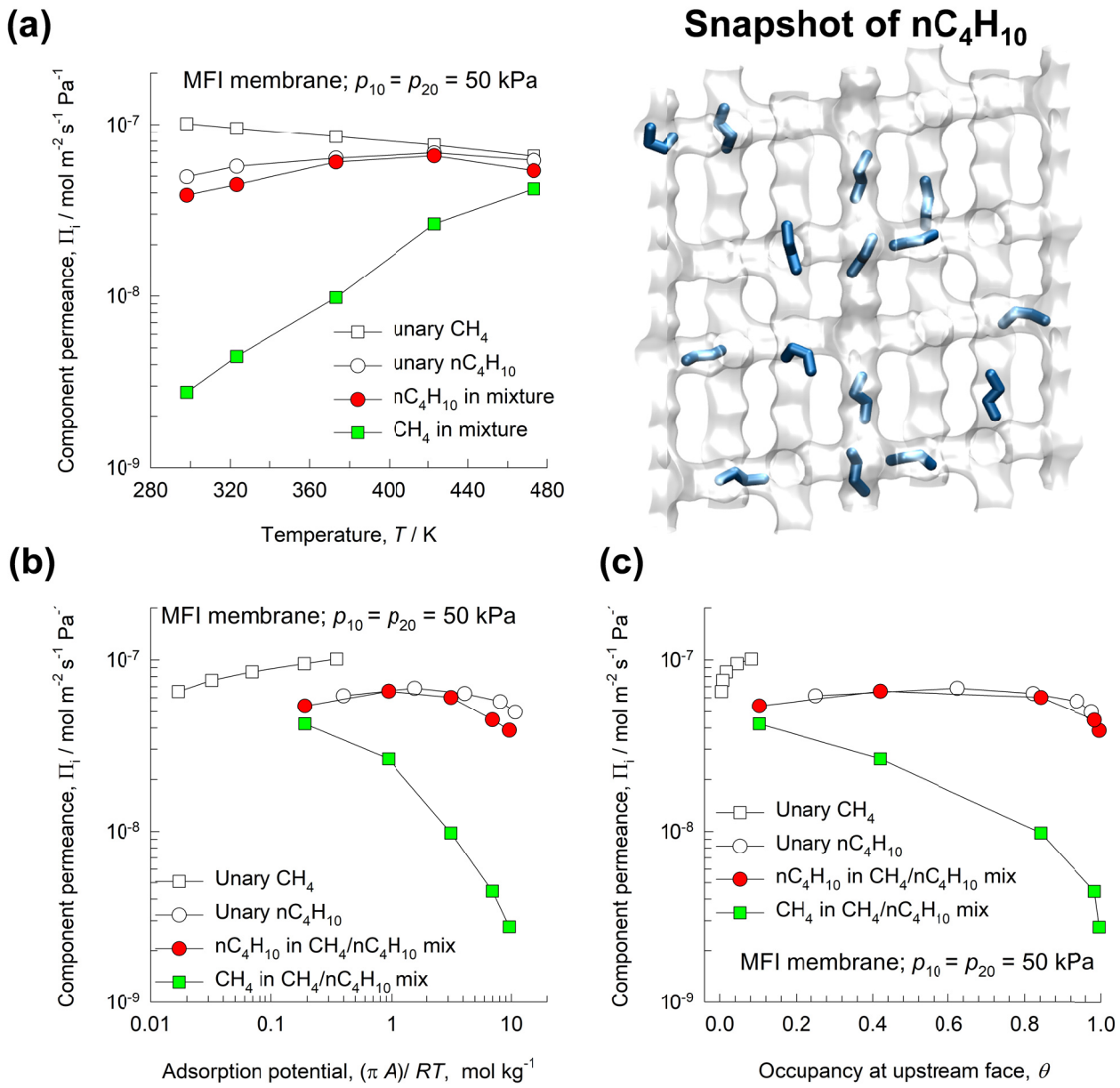

Figure S34. Experimental data of Vroon et al.[48] for unary and 50/50 CH_4/n-C_4H_{10} component permeances across MFI membrane at 100 kPa, and various temperatures. The data are plotted as function of (a) temperature and (b) adsorption potential $\pi A/RT$ and (c) occupancy θ at the upstream face of the membrane.

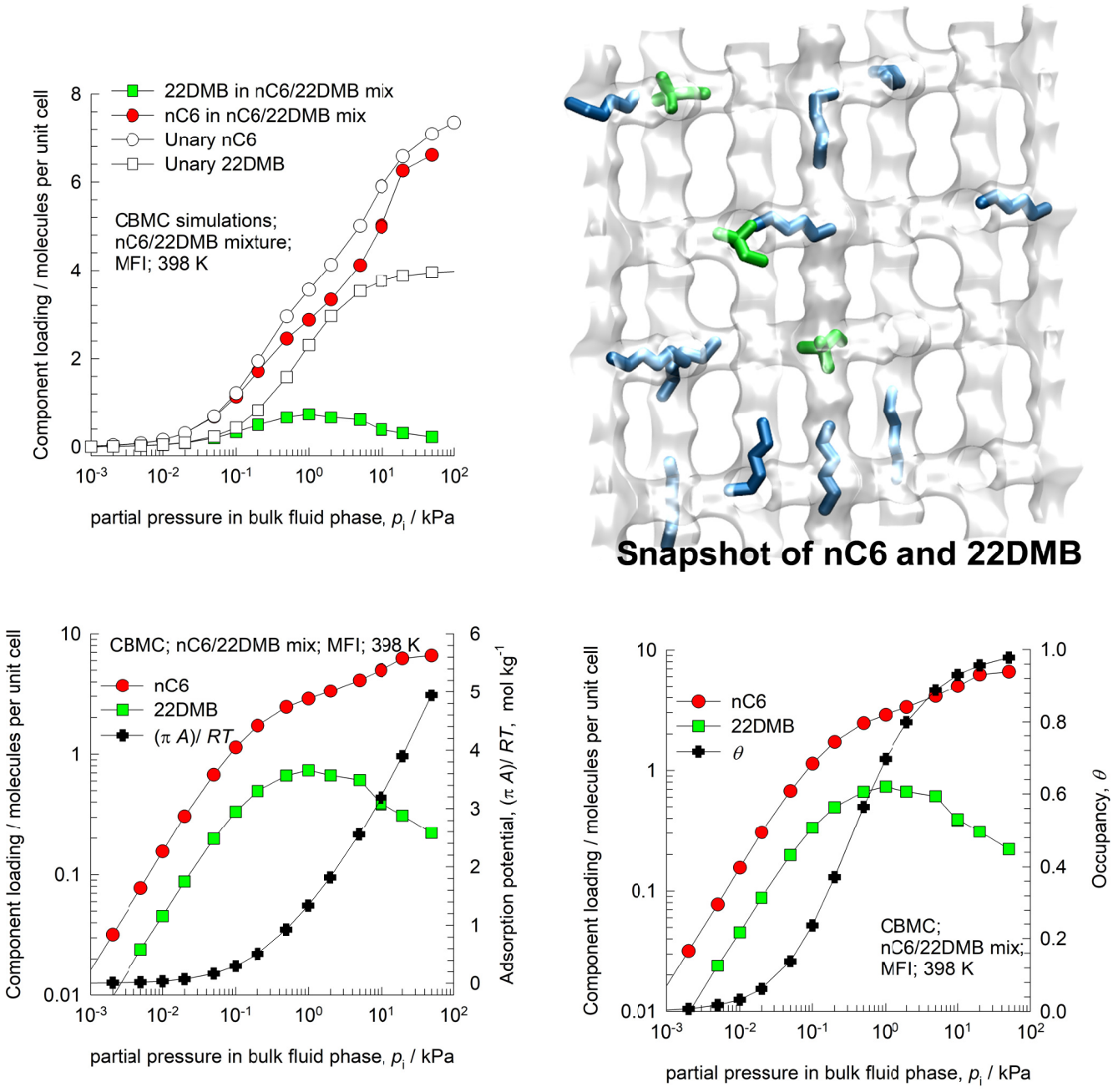

Figure S35. Configurational-Bias Monte Carlo (CBMC) simulations of unary and 50/50 nC6/22DMB mixture adsorption in MFI at 398 K. The data are plotted as function of upstream partial pressures, p_{i0}.

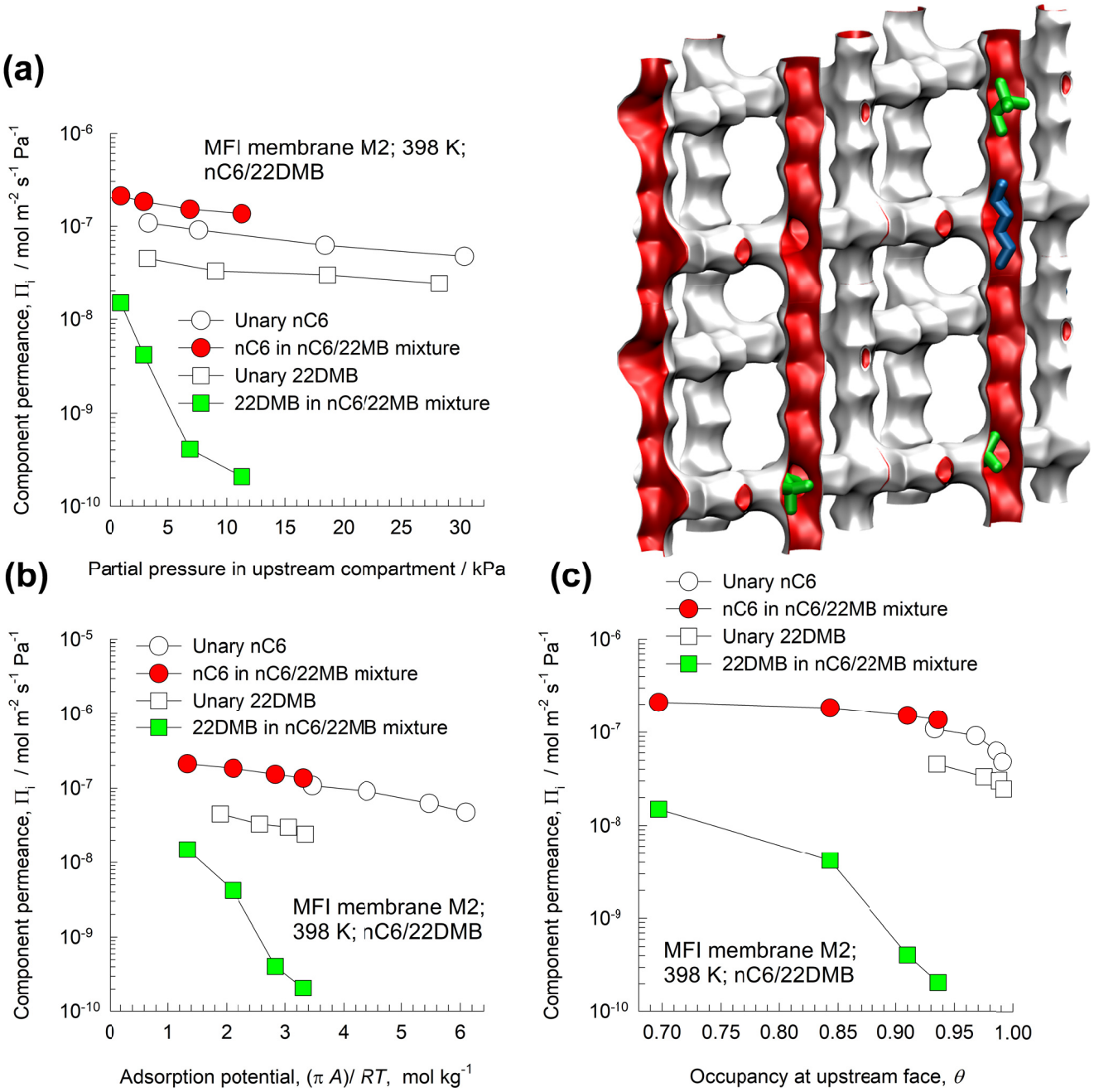

Figure S36. Experimental data Gump et al.[49] for unary and 50/50 nC6/22DMB mixture permeances across MFI membrane M2 at 398 K. The data are plotted as function of (a) upstream partial pressures, p_{i0} and(b) adsorption potential $\pi A/RT$ and (c) occupancy θ at the upstream face of the membrane.

9 Nomenclature

Latin alphabet

A	surface area per kg of framework, $m^2\ kg^{-1}$
b_A	dual-Langmuir-Freundlich constant for species *i* at adsorption site A, $Pa^{-\nu_A}$
b_B	dual-Langmuir-Freundlich constant for species *i* at adsorption site B, $Pa^{-\nu_B}$
$[B]$	Maxwell-Stefan matrix, $m^{-2}\ s$
$Đ_i$	Maxwell-Stefan diffusivity for molecule-wall interaction, $m^2\ s^{-1}$
$Đ_i(0)$	M-S diffusivity at zero-loading, $m^2\ s^{-1}$
$Đ_{ij}$	M-S exchange coefficient, $m^2\ s^{-1}$
$Đ_{12}$	M-S exchange coefficient for binary mixture, $m^2\ s^{-1}$
f_i	partial fugacity of species *i*, Pa
f_t	total fugacity of bulk fluid mixture, Pa
n	number of species in the mixture, dimensionless
N_i	molar flux of species *i* with respect to framework, $mol\ m^{-2}\ s^{-1}$
p_i	partial pressure of species *i* in mixture, Pa
p_t	total system pressure, Pa
P_i^0	sorption pressure, Pa
q_i	component molar loading of species *i*, $mol\ kg^{-1}$
$q_{i,sat}$	molar loading of species *i* at saturation, $mol\ kg^{-1}$
q_t	total molar loading in mixture, $mol\ kg^{-1}$
R	gas constant, 8.314 $J\ mol^{-1}\ K^{-1}$
T	absolute temperature, K

Nomenclature

w	energy of interaction, J mol^{-1}
x_i	mole fraction of species *i* in adsorbed phase, dimensionless
z	distance coordinate, m

Greek alphabet

β	parameter defined in equation (S43), and (S44), dimensionless
Γ_{ij}	thermodynamic factors, dimensionless
$[\Gamma]$	matrix of thermodynamic factors, dimensionless
δ_{ij}	Kronecker delta, dimensionless
ε	fractional pore volume of particle, dimensionless
ζ	coordination number defined in equation **Error! Reference source not found.**, dimensionless
λ	jump distance in lattice model, m
$[\Lambda]$	matrix of Maxwell-Stefan diffusivities, m^2 s^{-1}
μ_i	molar chemical potential of component *i*, J mol^{-1}
π	spreading pressure, N m^{-1}
Π_i	permeance of species *i* for zeolite membrane, mol m^{-2} s^{-1} Pa^{-1}
Θ_i	loading of species *i*, molecules per unit cell
$\Theta_{i,sat}$	saturation loading of species *i*, molecules per unit cell
Θ_t	total mixture loading, molecules per unit cage, or per unit cell
ν	jump frequency, s^{-1}
ν	exponent in dual-Langmuir-Freundlich isotherm, dimensionless
ϕ	parameter defined in equation (S43), and (S44), dimensionless
ρ	framework density, kg m^{-3}

Nomenclature

Subscripts

1	referring to component 1
2	referring to component 2
i	referring to component *i*
t	referring to total mixture
sat	referring to saturation conditions

10 References

(1) Myers, A. L.; Prausnitz, J. M. Thermodynamics of Mixed Gas Adsorption. *A.I.Ch.E.J.* **1965**, *11*, 121-130.

(2) Ruthven, D. M. *Principles of Adsorption and Adsorption Processes*. John Wiley: New York, 1984.

(3) Siperstein, F. R.; Myers, A. L. Mixed-Gas Adsorption. *A.I.Ch.E.J.* **2001**, *47*, 1141-1159.

(4) PTC MathCad 15.0. http://www.ptc.com/, PTC Corporate Headquarters, Needham, 3 November 2015.

(5) Krishna, R. Occupancy Dependency of Maxwell−Stefan Diffusivities in Ordered Crystalline Microporous Materials. *ACS Omega* **2018**, *3*, 15743-15753. https://doi.org/10.1021/acsomega.8b02465.

(6) Skoulidas, A. I.; Sholl, D. S.; Krishna, R. Correlation effects in diffusion of CH_4/CF_4 mixtures in MFI zeolite. A study linking MD simulations with the Maxwell-Stefan formulation. *Langmuir* **2003**, *19*, 7977-7988.

(7) Chempath, S.; Krishna, R.; Snurr, R. Q. Nonequilibrium MD simulations of difusion of binary mixtures containing short n-alkanes in faujasite. *J. Phys. Chem. B* **2004**, *108*, 13481-13491.

(8) Krishna, R. Describing the Diffusion of Guest Molecules inside Porous Structures. *J. Phys. Chem. C* **2009**, *113*, 19756-19781.

(9) Krishna, R. Diffusion in Porous Crystalline Materials. *Chem. Soc. Rev.* **2012**, *41*, 3099-3118.

(10) Krishna, R.; van Baten, J. M. Onsager coefficients for binary mixture diffusion in nanopores. *Chem. Eng. Sci.* **2008**, *63*, 3120-3140.

(11) Hansen, N.; Keil, F. J. Multiscale modeling of reaction and diffusion in zeolites: from the molecular level to the reactor. *Soft Mater.* **2012**, *10*, 179-201.

(12) Krishna, R.; van Baten, J. M. An Investigation of the Characteristics of Maxwell-Stefan Diffusivities of Binary Mixtures in Silica Nanopores. *Chem. Eng. Sci.* **2009**, *64*, 870-882.

(13) Krishna, R.; van Baten, J. M. Unified Maxwell-Stefan Description of Binary Mixture Diffusion in Micro- and Meso- Porous Materials. *Chem. Eng. Sci.* **2009**, *64*, 3159-3178.

(14) Krishna, R.; van Baten, J. M. Investigating the Influence of Diffusional Coupling on Mixture Permeation across Porous Membranes *J. Membr. Sci.* **2013**, *430*, 113-128.

(15) Krishna, R.; Baur, R. Modelling Issues in Zeolite Based Separation Processes. *Sep. Purif. Technol.* **2003**, *33*, 213-254.

(16) Krishna, R.; van Baten, J. M. Diffusion of alkane mixtures in zeolites. Validating the Maxwell-Stefan formulation using MD simulations. *J. Phys. Chem. B* **2005**, *109*, 6386-6396.

(17) Krishna, R.; van Baten, J. M. Influence of segregated adsorption on mixture diffusion in DDR zeolite. *Chem. Phys. Lett.* **2007**, *446*, 344-349.

(18) Krishna, R.; van Baten, J. M. Insights into diffusion of gases in zeolites gained from molecular dynamics simulations. *Microporous Mesoporous Mater.* **2008**, *109*, 91-108.

(19) Krishna, R.; van Baten, J. M. Segregation effects in adsorption of CO_2 containing mixtures and their consequences for separation selectivities in cage-type zeolites. *Sep. Purif. Technol.* **2008**, *61*, 414-423.

(20) Krishna, R.; van Baten, J. M. Describing Mixture Diffusion in Microporous Materials under Conditions of Pore Saturation. *J. Phys. Chem. C* **2010**, *114*, 11557-11563.

References

(21) Krishna, R.; van Baten, J. M. A molecular dynamics investigation of the diffusion characteristics of cavity-type zeolites with 8-ring windows. *Microporous Mesoporous Mater.* **2011**, *137*, 83-91.

(22) Krishna, R.; van Baten, J. M. Maxwell-Stefan modeling of slowing-down effects in mixed gas permeation across porous membranes. *J. Membr. Sci.* **2011**, *383*, 289-300.

(23) Krishna, R. The Maxwell-Stefan Description of Mixture Permeation across Nanoporous Graphene Membranes. *Chem. Eng. Res. Des.* **2018**, *133*, 316-325. https://doi.org/10.1016/j.cherd.2018.03.033.

(24) Reed, D. A.; Ehrlich, G. Surface diffusion, atomic jump rates and thermodynamics. *Surf. Sci.* **1981**, *102*, 588-609.

(25) Krishna, R.; Paschek, D.; Baur, R. Modelling the occupancy dependence of diffusivities in zeolites. *Microporous Mesoporous Mater.* **2004**, *76*, 233-246.

(26) Krishna, R.; van Baten, J. M. A molecular dynamics investigation of a variety of influences of temperature on diffusion in zeolites. *Microporous Mesoporous Mater.* **2009**, *125*, 126-134.

(27) Olson, D. H.; Camblor, M. A.; Vallaescusa, L. A.; Kuehl, G. H. Light hydrocarbon sorption properties of pure silica Si-CHA and ITQ-3 and high silica ZSM-58. *Microporous Mesoporous Mater.* **2004**, *67*, 27-33.

(28) Hedin, N.; DeMartin, G. J.; Roth, W. J.; Strohmaier, K. G.; Reyes, S. C. PFG NMR self-diffusion of small hydrocarbons in high silica DDR, CHA and LTA structures. *Microporous Mesoporous Mater.* **2008**, *109*, 327-334.

(29) Ruthven, D. M.; Reyes, S. C. Adsorptive separation of light olefins from paraffins. *Microporous Mesoporous Mater.* **2007**, *104*, 59-66.

(30) Khalighi, M.; Chen, Y. F.; Farooq, S.; Karimi, I. A.; Jiang, J. W. Propylene/Propane Separation Using SiCHA. *Ind. Eng. Chem. Res.* **2013**, *52*, 3877-3892.

(31) Li, S.; Falconer, J. L.; Noble, R. D.; Krishna, R. Interpreting unary, binary and ternary mixture permeation across a SAPO-34 membrane with loading-dependent Maxwell-Stefan diffusivities. *J. Phys. Chem. C* **2007**, *111*, 5075-5082.

(32) Li, S.; Falconer, J. L.; Noble, R. D.; Krishna, R. Modeling permeation of CO_2/CH_4, CO_2/N_2, and N_2/CH_4 mixtures across SAPO-34 membrane with the Maxwell-Stefan equations. *Ind. Eng. Chem. Res.* **2007**, *46*, 3904-3911.

(33) Krishna, R.; Li, S.; van Baten, J. M.; Falconer, J. L.; Noble, R. D. Investigation of slowing-down and speeding-up effects in binary mixture permeation across SAPO-34 and MFI membranes. *Sep. Purif. Technol.* **2008**, *60*, 230-236.

(34) Himeno, S.; Takenaka, M.; Shimura, S. Light gas adsorption of all-silica DDR- and MFI-type zeolite: computational and experimental investigation. *Molecular Simulation* **2008**, *34*, 1329-1336.

(35) Himeno, S.; Tomita, T.; Suzuki, K.; Nakayama, K.; Yoshida, S. Synthesis and Permeation Properties of a DDR-type zeolite membrane for Separation of CO_2/CH_4 Gaseous Mixtures. *Ind. Eng. Chem. Res.* **2007**, *46*, 6989-6997.

(36) Himeno, S.; Tomita, T.; Suzuki, K.; Yoshida, S. Characterization and selectivity for methane and carbon dioxide adsorption on the all-silica DD3R zeolite. *Microporous Mesoporous Mater.* **2007**, *98*, 62-69.

(37) van den Bergh, J.; Zhu, W.; Groen, J. C.; Kapteijn, F.; Moulijn, J. A.; Yajima, K.; Nakayama, K.; Tomita, T.; Yoshida, S. Natural Gas Purification with a DDR Zeolite Membrane; Permeation Modelling with Maxwell-Stefan Equations. *Stud. Surf. Sci. Catal.* **2007**, *170*, 1021-1027.

(38) van den Bergh, J.; Zhu, W.; Gascon, J.; Moulijn, J. A.; Kapteijn, F. Separation and Permeation Characteristics of a DD3R Zeolite Membrane. *J. Membr. Sci.* **2008**, *316*, 35-45.

(39) Krishna, R.; van Baten, J. M. Investigating the Relative Influences of Molecular Dimensions and Binding Energies on Diffusivities of Guest Species Inside Nanoporous Crystalline Materials *J. Phys. Chem. C* **2012**, *116*, 23556-23568.

References

(40) Li, K.; Olson, D. H.; Seidel, J.; Emge, T. J.; Gong, H.; Zeng, H.; Li, J. Zeolitic Imidazolate Frameworks for Kinetic Separation of Propane and Propene. *J. Am. Chem. Soc.* **2009**, *131*, 10368-10369.

(41) Bux, H.; Chmelik, C.; Krishna, R.; Caro, J. Ethene/Ethane Separation by the MOF Membrane ZIF-8: Molecular Correlation of Permeation, Adsorption, Diffusion. *J. Membr. Sci.* **2011**, *369*, 284-289.

(42) Liu, D.; Ma, X.; Xi, H.; Lin, Y. S. Gas transport properties and propylene/propane separation characteristics of ZIF-8 membranes. *J. Membr. Sci.* **2014**, *451*, 85-93.

(43) Krishna, R. Evaluation of Procedures for Estimation of the Isosteric Heat of Adsorption in Microporous Materials. *Chem. Eng. Sci.* **2015**, *123*, 191-196.

(44) Böhme, U.; Barth, B.; Paula, C.; Kuhnt, A.; Schwieger, W.; Mundstock, A.; Caro, J.; Hartmann, M. Ethene/Ethane and Propene/Propane Separation via the Olefin and Paraffin Selective Metal−Organic Framework Adsorbents CPO-27 and ZIF-8. *Langmuir* **2013**, *29*, 8592-8600.

(45) Sandström, L.; Sjöberg, E.; Hedlund, J. Very high flux MFI membrane for CO_2 separation. *J. Membr. Sci.* **2011**, *380*, 232-240.

(46) Sjöberg, E.; Barnes, S.; Korelskiy, D.; Hedlund, J. MFI membranes for separation of carbon dioxide from synthesis gas at high pressures. *J. Membr. Sci.* **2015**, *486*, 132-137.

(47) van de Graaf, J. M.; Kapteijn, F.; Moulijn, J. A. Modeling permeation of binary mixtures through zeolite membranes. *A.I.Ch.E.J.* **1999**, *45*, 497-511.

(48) Vroon, Z. A. E. P.; Keizer, K.; Gilde, M. J.; Verweij, H.; Burggraaf, A. J. Transport properties of alkanes through ceramic thin zeolife MFI membranes. *J. Membr. Sci.* **1996**, *113*, 293-300.

(49) Gump, C. J.; Noble, R. D.; Falconer, J. L. Separation of hexane isomers through nonzeolite pores in ZSM-5 zeolite membranes. *Ind. Eng. Chem. Res.* **1999**, *38*, 2775-2781.

(50) Golden, T. C.; Sircar, S. Gas Adsorption on Silicalite. *J. Colloid Interface Sci.* **1994**, *162*, 182-188.